University of Reading

School of Chemistry

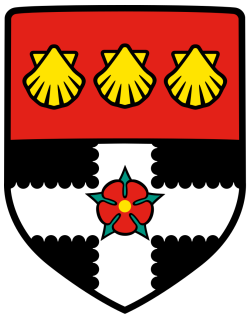

Studying the Surface Chemistry of Methane Oxidation Catalysts with Near-Ambient Pressure X-Ray Photoelectron Spectroscopy

A thesis submitted in partial fulfilment of the requirements for the degree of Doctor of Philosophy

Rachel Price

September 2016

Supervised by Professor Georg Held

Declaration

I confirm that this is my own work and the use of all material from other sources has been properly and fully acknowledged.

Signed

Rachel Price

Acknowledgements

I have been very fortunate to travel half way around the world with this project, and there are many people at home and at work to whom I owe a huge thank you, Danke, grazie, ευχαριστώ, khob khun ka and teşekkür ederim.

To the laboratory technicians Graham, Muhammed, Chris and George, for letting me borrow the odd piece of lab equipment and making demonstrating in the teaching labs an easy job for me.
To Catherine O'Hare and Judy Butler, for efficiently dealing with administrative tasks and being extremely helpful in answering any kind of enquiry.
To my PhD colleagues: Ed Nicklin, Silvia Baldanza and Jacopo Ardini who welcomed me into the group and were invaluable in their help with everything UHV and beamtime-related.
To Roger Bennett, for his help with problems in the lab and all the useful discussions on physical chemistry.
To many people at Johnson Matthey including, but not limited to, Peter Ash, Dave Thompsett, Richard Smith and Glenn Jones for having me at Johnson Matthey in the first place, Sonia Garcia for happily spending a lot of her time supervising me making catalysts, Agnes Raj for all the helpful meetings on methane oxidation and letting me come any time to use her SCAT rig, and the whole Microscopy team for fast-tracking my TEM data.
To Ethan Crumlin and all the staff at ALS 9.3.2 in Berkeley, for maintaining a brilliant beamline and helping me take data around the clock for this PhD project.
To Chanan Euaruksakul, for expertly doing the work of three people and for whom no task was too big or too small.
To Panos Tsaousis, for being my companion in the lab and introducing me to a catalogue of Eurovision hits.

To Tuğçe Eralp-Erden, for taking me with her to Barcelona, always being welcoming and making me feel like part of the furniture at Johnson Matthey, in a good way.
To my supervisor, Georg Held, for his expert guidance throughout my PhD and for taking me to the best jazz bars in San Francisco.
To my friends in Reading, past and present, for providing welcome distractions outside of science.
To Louise, for joining me on my quest to find the best Cosmopolitan in Reading.
To my friends in Essex, for their many spontaneous trips to Reading over the last eight years, but to Adam in particular, who lives vicariously through me and who I know will cite my paper whenever he needs a reference for ambient pressure XPS or methane oxidation catalysis.
To Kieran, for being my best friend and always being there at the end of the day to laugh, relax, and enjoy life with.
To my family, for always pretending to be interested in my work and humouring me by promising to address me as "Dr" when I finish.
And finally, to my Mum, Dad and brother, for always being proud of me despite not pretending to be interested in my work, for calling me a "tax dodger", and for probably not making room for this on their bookshelf.

This project was jointly funded by the University of Reading and Johnson Matthey. I would also like to thank the Royal Society of Chemistry and COST Action CM0904 for supporting my trips to ALS, Berkeley.

Abstract

The surface chemistry and activity of a range of supported-palladium catalysts, known for their high activity in methane oxidation reactions, were studied using near-ambient pressure x-ray photoelectron spectroscopy (NAP-XPS) and in-situ mass spectrometry. Using NAP-XPS, the chemical state of the catalyst was monitored under 0.33 mbar of a methane and oxygen gas mixture and a temperature ramp up to 800 K. In-situ mass-spectrometry was able to quantify the partial pressures of reactants and products throughout the temperature ramp, and the chemical state of the catalyst as determined by NAP-XPS was correlated to product formation. As a result, the impact of Pd particle size and support material on catalytic behaviour was studied, in addition to finding the active state of the catalyst.

For supported-Pd catalysts on Al_2O_3, SiO_2 and SiO_2-Al_2O_3, NAP-XPS showed PdO to be the dominant oxidation state at 500 – 600 K. Despite a gas ratio of $[CH_4]$:$[O_2]$ = 2, the complete oxidation of methane is favoured at these temperatures where CO_2 and H_2O are produced. PdO, therefore, was found to be the active state for complete methane oxidation. As the O_2 depletes and the temperature increases to >650 K, PdO reduces to PdO_x, where $0 \leq x < 1$. The partial pressures of CO_2 and H_2O decrease and syngas formation (H_2 and CO), the product of partial methane oxidation, is dominant, suggesting reduced Pd is the active state for partial methane oxidation. From NAP-XPS, it is possible to identify this change in oxidation state from a shift in binding energy. The temperature at which the shift from high to low binding energy of the Pd 3d peaks occurs corresponds to the onset temperature of syngas, as determined by mass spectrometry. A particle size effect was observed for Pd/Al_2O_3 and Pd/SiO_2 catalysts with Pd particle size ranges of 4 – 10 nm and 2 – 6 nm respectively, whereby the onset temperature of syngas, and the temperature at which PdO reduced, decreased with increasing particle size. This effect suggests that a larger particle size is more active towards partial methane oxidation, due to a greater metal-support interaction, and hence decreased reducibility, of smaller sized particles. The reactivity of support materials increased in the order: $SiO_2 < SiO_2$-$Al_2O_3 < Al_2O_3$.

Contents

List of Abbreviations

Abbreviation	Meaning
ALS	Advanced Light Source
ICP-MS	inductively coupled plasma mass spectrometry
IMFP	inelastic mean free path
FT-IR	Fourier transform infrared
FWHM	full width of half maximum
NAP-XPS	near-ambient pressure x-ray photoelectron spectroscopy
NGV	natural gas vehicle
PGM	platinum group metals
POM	partial oxidation of methane
SCAT	synthetic catalyst activity test
SCLS	surface core level shift
SEM	scanning electron microscopy
SSE	secondary electron emission
syngas	synthesis gas, H_2 + CO
TEM	transmission electron microscopy
THF	tetrahydrofuran
TP-XPS	temperature-programmed x-ray photoelectron spectroscopy
UHV	ultra-high vacuum
WGS	water-gas shift reaction
XPS	x-ray photoelectron spectroscopy
XRD	x-ray diffraction

1 Introduction

1.1 Catalysis

A catalyst is a non-participating component of a reaction with the purpose of providing an alternative reaction pathway to overcome an activation energy barrier. Catalysis, from the Ancient Greek $\kappa\alpha\tau\alpha\lambda\upsilon\sigma\iota\varsigma$ meaning "dissolution", is a kinetic process where chemical bonds are broken and formed between two or more reactant molecules on the surface of a catalyst. The catalyst enables an exothermic spontaneous reaction of two reactants with an activation energy significantly lower than for an uncatalysed reaction. After the product molecule desorbs, the catalyst is left chemically unchanged and able to repeat the process [1].

Figure 1.1 shows the energy levels of different points in a bimolecular reaction, with and without a heterogeneous catalyst. In the absence of a catalyst, the reaction relies on collisions between molecules A and B, which is a random process with an activation energy usually much higher than the thermal energy of the molecules [2].

The addition of a catalyst creates an alternative reaction pathway with several elementary steps. The first step involves the adsorption of the reactants onto the surface of the catalyst. In the second step, the reactants A and B react with each other to form a product, which desorbs from the catalyst surface in the third step. Although the change in Gibbs free energy from the first step to the final step (ΔG) is always the same, regardless of the presence or absence of a catalyst, the indi-

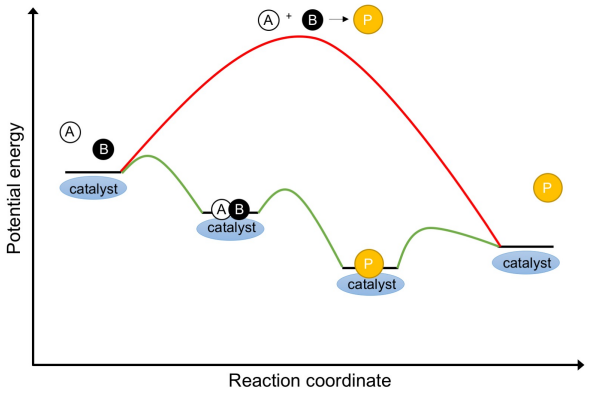

Figure 1.1: Energy diagram of a gas-phase bimolecular reaction with and without a solid catalyst.

vidual steps in the catalysed reaction require much less energy than that of the uncatalysed reaction. Therefore, the catalysed reaction is more kinetically favourable and will exhibit a much higher overall rate of reaction.

Heterogeneous catalysis is when the reactants are in a different phase to the catalyst, i.e. a gas phase reaction with a solid catalyst. This is more favourable over homogeneous catalysis, where the reactants and catalyst are in the same phase, due to much easier separation of the catalyst after the reaction. In addition, the active phase in many catalysts is an expensive metal, so it is economically desirable to reuse the same catalyst for many different reactions [3]. With a solid catalyst, the catalytic reaction occurs at the surface of the catalyst, where gas or liquid phase molecules adsorb, react and desorb. When designing a catalyst therefore, it is important to achieve maximum dispersion of the active phase on the surface to obtain maximum catalytic activity. The rate of adsorption depends on the reactant pressure or concentration, where a higher pressure or concentration increases the likelihood of molecules hitting the catalyst surface and absorbing. The Langmuir adsorption isotherm in Equation 1.1 defines the amount of gas adsorbed onto a surface as a function of pressure, assuming the system is at equilibrium where the rates of adsorption and desorption are equal:

$$\theta = \frac{bp}{1 + bp} \tag{1.1}$$

where θ is the fraction of the surface covered with adsorbate, p is the pressure of the gas and b is the adsorption coefficient. The Langmuir adsorption isotherm also assumes that each active site can only hold one molecule and the heat of adsorption is independent of the number of active sites [4]. The rate of reaction depends on the reaction mechanism, and is discussed in Section 1.1.1.

Heterogeneous catalysis is used in many industrial processes because of the ability to lower reaction temperatures and pressures, which all help to save costs. The human population relies on the conversion of feedstocks into fuels and the subsequent protection from the harmful by-products resulting from fuel processing. For example, car exhaust emissions are controlled with Pd, Pt and Rh catalysts which oxidise pollutant NO_x gases in a catalytic converter [5]. Heterogeneous catalysts are used in many other processes that are used daily in human life, including ammonia synthesis for fertilisers with a solid Fe catalyst [6], formaldehyde synthesis from a Ag catalyst which is turned into resins for furniture, and

ethylene oxide synthesis with a supported Ag catalyst for use in washing powders [7].

1.1.1 Mechanisms in Heterogeneous Catalysis

Bimolecular catalytic reactions can occur via different possible mechanisms. The type of mechanism the reaction follows depends on the type of reaction or the catalyst surface. Figure 1.2 depicts schematic diagrams of two different bimolecular mechanisms.

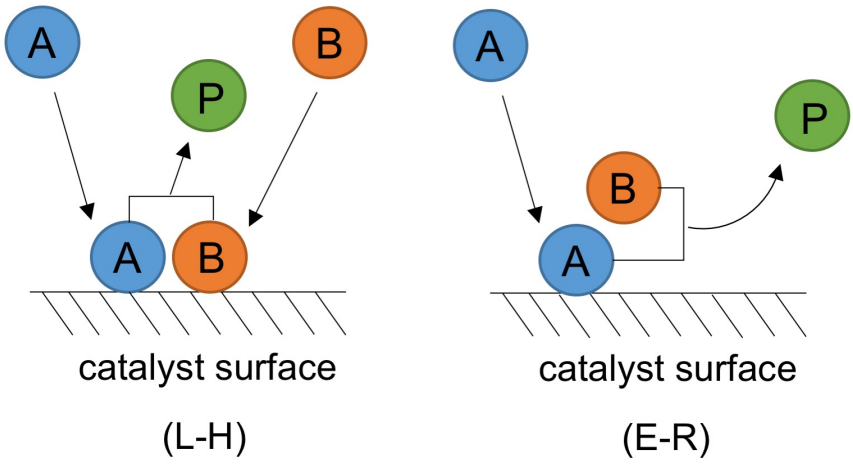

Figure 1.2: Schematic diagrams of the Langmuir-Hinshelwood (L-H) and Eley-Rideal (E-R) mechanisms [8]

The first mechanism is the Langmuir-Hinshelwood (L-H) mechanism, in which two reactant molecules adsorb onto neighbouring sites on the surface of the catalyst, react on the surface to form a product that subsequently desorbs into the gas or liquid phase. In this instance, it is assumed that both reactant molecules competitively adsorb on the same active sites, and so the rate-determining step is the formation of the product on the catalyst surface. The catalytic oxidation of CO on Pt, Rh and Ir surfaces is thought to occur via a Langmuir-Hinshelwood mechanism [9–11]:

$$\mathrm{CO} + * \longrightarrow \mathrm{CO}*$$

$$\mathrm{O_2} + 2* \longrightarrow 2\,\mathrm{O}*$$

$$\mathrm{O}* + \mathrm{CO}* \longrightarrow \mathrm{CO_{2(g)}}$$

where * denotes an active site on the surface of the catalyst. The rate of reaction in the Langmuir-Hinshelwood mechanism is simply based on the amount of adsorbed species A and B:

$$\mathrm{Rate}_{L-H} = k\theta_A\theta_B \tag{1.2}$$

where k is the rate constant and θ_A and θ_B are the respective amounts of reactants A and B adsorbed onto the surface of the catalyst. Substituting in the Langmuir adsorption isotherm from Equation 1.1, the dependence on pressure of the Langmuir-Hinshelwood mechanism can be expressed as:

$$\text{Rate}_{L-H} = k\frac{b_A p_A \cdot b_B p_B}{(1 + b_A p_A + b_B p_B)^2} \tag{1.3}$$

There are also cases whereby only one of the reactant molecules adsorbs to the catalyst surface and reacts with a second molecule that remains in the gas phase, known as the Eley-Rideal (E-R) mechanism, also shown in Figure 1.2 [8]. The rate-determining step is the collision between a surface adatom and a gas phase molecule [12], and relies on the surface of the catalyst being saturated with the adsorbate molecule in order to get the maximum reaction rate [13]. The rate equation for the Eley-Rideal mechanism is given in Equation 1.4:

$$\text{Rate}_{E-R} = k\theta_A p_B \tag{1.4}$$

where p_B is the pressure of reactant B. Substituting the Langmuir adsorption isotherm from Equation 1.1 the rate can be further expressed as:

$$\text{Rate}_{E-R} = k\frac{b_A p_A}{1 + b_A p_A} \cdot b_B p_B \tag{1.5}$$

A higher coverage of reactant A and a higher pressure of reactant B would increase the reaction rate. The rate of reaction also depends on the adsorption strength of reactant A, as a weak adsorption would make the reaction rate proportional to the pressures of both reactants A and B, whereas a strong adsorption of A would only render the reaction rate dependent on the pressure of reactant B. The Eley-Rideal mechanism is largely thought to occur in the recombination of hydrogen atoms on a graphite surface [14, 15] and the addition of hydrogen atoms to small hydrocarbons on a metal surface [16].

Many solid catalysts for heterogeneous reactions consist of an oxide support material or a metal oxide surface, and the Mars-van Krevelen mechanism uses oxygen from the catalyst itself to oxidise the reactant molecule. As shown in Figure 1.3, the reactant molecule A adsorbs onto a surface oxygen atom

from the catalyst material and desorbs to form an oxidation product, P. The surface oxygen vacancy is then filled by oxygen from the gas phase, or from the catalyst bulk material [17].

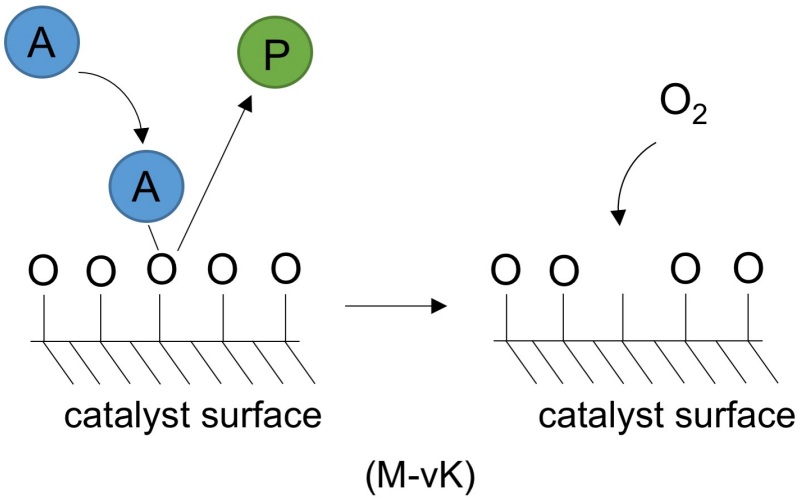

Figure 1.3: Schematic diagram of the Mars-van Krevelen mechanism [13].

The rate of reaction in the Mars-van Krevelen mechanism is dependent on reactant A forming a chemical bond to the surface (θ_A) and the pressure of reactant B which reacts with the chemically bonded reactant A, resulting in a rate equation mathematically the same as for the Eley-Rideal mechanism [18]:

$$\text{Rate}_{MvK} = k\theta_A p_{O_2} \tag{1.6}$$

Many oxidation reactions are proposed to proceed via the Mars-van Krevelen reaction, including the photocatalytic oxidation of cyclohexane with a TiO_2 catalyst [19] and the oxidation of methanol to formaldehyde with MoO_2 and MoO_3 catalysts [20]. In addition, it has also been reported that the oxidation of methane proceeds via a Mars-van Krevelen mechanism, whereby the rate-determining step is the activation of a C-H bond on a oxygen atom on the surface of a noble metal catalyst [21–23]. Fujimoto et al. report that the CH_4 molecule adsorbs onto an unsaturated Pd atom on a PdO surface and uses the surface oxygen from a neighbouring PdO to form a Pd-OH moiety [24].

1.2 PGM Catalysts

Platinum group metals (PGMs) is the collective name for the six d-block elements Ru, Rh, Pd, Os, Ir and Pt. Platinum was first discovered in the 16th century in Columbia, and first named "platina del Pinto" ("little silver of the River Pinto") after its shiny, silvery appearance. Palladium, rhodium, osmium and iridium were discovered three hundred years later, with palladium being named after Pallas, a recently discovered asteroid, rhodium after the rose colour of its salts (from the Greek *rhodes* meaning "rose"), iridium after its multicoloured salts ("iridescent" or "rainbow" from the Greek *iris*) and osmium from the Greek *osme* meaning "smell", due to the characteristic odour of its tetroxide. Ruthenium was the last PGM to be discovered, named after the Latin word for Russia (*Ruthenia*), where it was discovered by K. K. Klaus in 1844 [25,26].

The PGMs are precious, expensive metals that have similar chemical properties, as shown in Figure 1.4. Pt and Pd are relatively soft, have high resistance to oxidation and temperature and widespread use in catalysis. Rh and Ir are of a similar hardness and Rh also exhibits excellent catalytic activity. Ru and Os are brittle and have poor resistance to oxidation, but are often used in combination with other PGMs to form effective catalysts [27].

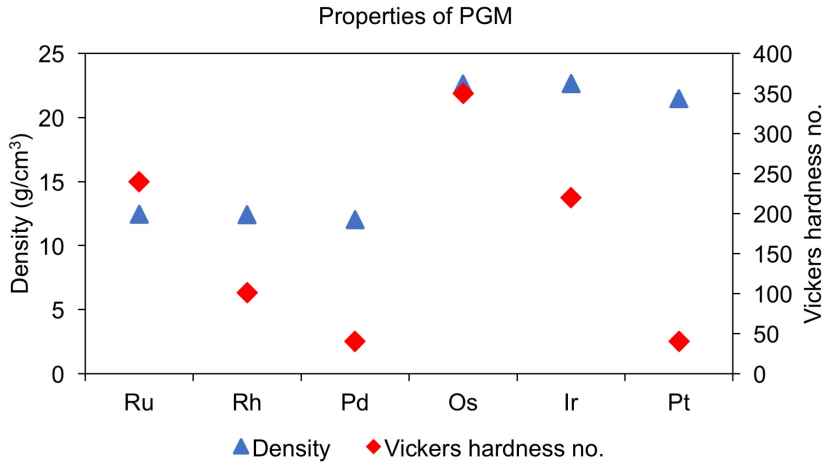

Figure 1.4: The density (g/cm^3) and hardness of the PGMs in order of atomic number [27].

As well as use in automotive catalysts, the PGMs are used for jewellery due to their anti-corrosion properties, and in many industrial uses including the dental industry, electrical components and phar-

maceuticals. As a result of their high demand, 450 tonnes of PGM were extracted in 2009 with a value of $15 billion [28].

1.2.1 Complete Oxidation of Methane

The complete oxidation of methane, or complete combustion of methane, is the conversion of methane under an excess of oxygen to CO_2 and H_2O:

$$\mathrm{CH_4 + 2\,O_2 \longrightarrow CO_2 + 2\,H_2O} \tag{1.7}$$

Complete methane oxidation to CO_2 and H_2O occurs naturally via a multistep reaction at high temperatures, or by flame combustion at 2000 K, producing more heat per mass than any other hydrocarbon (55.7 kJ/g) and a total energy of 50.1 MJ/kg [29,30]. In addition to producing only one molecule of CO_2 per molecule of CH_4, methane is inexpensive and highly abundant; natural gas reserves are thought to last for another 537 years with 204.7×10^{12} m^3 naturally available [31]. For all the aforementioned reasons, natural gas is considered to be an effective source of fuel for engines replacing traditional gasoline and diesel fuels, although a large amount of methane remains unburned and pollutes the atmosphere [32]. The challenge, therefore, is to develop a catalyst to catalytically convert all methane into its component products to reduce CH_4 emissions from exhaust gas. It is well established that palladium-based catalysts are the most active towards methane oxidation. The facile reducibility of Pd makes it a better catalyst than other noble metals for methane combustion [21]. However, under a high excess of oxygen, or lean burn, NO_x gases are also produced and so the addition of platinum to the catalyst is often used for a lean burn engine to reduce NO_x to NH_4 [33]. Catalytic methane combustion enables lower temperature conversion of methane, reaching 50% conversion at 700 – 800 K, by overcoming the high dissociation energy of the C-H bond (439.3 kJ mol^{-1}) [34]. To gain maximum dispersion and surface area, the Pd is usually in the form of small particles ($<$ 20 nm) and supported on a metal oxide support material, usually Al_2O_3 [35–37], SiO_2 [37,38] or ZrO_2 [24,39,40]. There is an ongoing debate about whether the active phase of the metal is PdO, metallic Pd, or a mixture of both [41], or if the redox process itself is in fact driving the reaction [42]. The biggest problem for catalyst poisoning in the complete oxidation of methane is water formation, as not only atmospheric water vapour but water produced in the oxidation both deactivate Pd sites. The formation of hydroxyl, carbonates and formates, by as little as 5% water in the system, significantly poisons the catalyst by blocking active sites. Although

reversible when water is removed from the feed under experimental conditions, it is impractical in engines to have to do so [33]. There are many studies into the mechanism of water inhibition on different methane oxidation catalysts [38, 43–46] and if this is understood, significant improvements could be made to circumvent this issue.

1.2.2 Partial Oxidation of Methane to Syngas

Under an oxygen deficit, methane can be partially oxidised to CO and H_2, a mixture otherwise known as "synthesis gas" or syngas:

$$\mathrm{CH_4} + \frac{1}{2}\,\mathrm{O_2} \longrightarrow \mathrm{CO} + 2\,\mathrm{H_2} \tag{1.8}$$

Partial methane oxidation to syngas is an effective way to produce hydrogen for use in fuel cells, and syngas for methanol synthesis. A liquid at room temperature, methanol is more easily stored and transported for use as biofuel than methane and its synthesis occurs at relatively low temperatures (473 – 573 K) over a Cu/ZnO based catalyst [47]. Historically, syngas has been produced in large quantities by steam reforming and a Ni catalyst, where methane and steam react together at temperatures in excess of 1000 K to produce hydrogen and carbon dioxide [48]. Due to the high, expensive operating temperatures of steam reforming, the catalytic partial oxidation of methane has become a favourable route to producing syngas [49]. In addition to methanol, syngas is useful for the formation of longer chain liquid hydrocarbons, such as kerosine and gasoline, via the Fischer-Tropsch process [50, 51]. Partial oxidation (ΔH = -35.5 kJ mol^{-1}) is competing against more exothermic oxidation reactions producing water and various ratios of CO, CO_2 and H_2 (ΔH = -519.2 – -802.5 kJ mol^{-1}) that, to a certain extent, can be controlled by pressure, temperature and gas composition to shift equilibria [52, 53], but the main challenge with catalytic partial oxidation of methane is designing a catalyst with optimum selectivity to syngas in a 2:1 ratio of H_2 to CO. There has been intense research into Ni catalysts for partial oxidation of methane due to high performance and low cost, although loss of activity and deactivation has been shown to occur due to carbon deposition and sintering at high temperatures [34, 53–55]. Platinum group metals have also been shown to exhibit good activity and selectivity towards syngas formation under partial oxidation conditions, with good thermal stability against sintering. Li et al. reported both good catalytic performance and high thermal stability with a Pd/SiO_2 catalyst [56], and a study by Wang and Ruckenstein showed supported-Rh catalysts to exhibit excellent activity and selectivity towards syngas formation [57]. In this project, the partial oxidation of methane with Pd catalysts is explored by monitoring the surface chemical composition and activity of each catalyst in-situ.

1.3 Particle Size Effects in Catalysis

There are many debates currently regarding whether catalytic reactions with supported-metal catalysts are structure sensitive or not. Structure sensitivity arises from the changes in metal particle size, that in turn vary the number of steps, terraces and active sites available for catalysis and hence affect the rate of reaction. This is not always the case and depends on the reaction [58]. Catalytic reactions can be structure sensitive in two ways: firstly an increased particle size up to 20 nm can increase the turnover frequency, such as in the CO hydrogenation reaction with a Ru/Al_2O_3 catalyst; and secondly increasing particle size up to 20 nm can decrease the turnover frequency as in ethane hydrogenolysis on Pt/SiO_2. A structure insensitive reaction would show no increase or decrease in turnover frequency with changes in particle size, such as in the Pt/SiO_2 catalysed benzene hydrogenation reaction [59–61].

In methane oxidation, the dissociation of the C-H bond is thought to occur faster on bridge and kink sites, where a large proportion of the metal atoms are coordinatively unsaturated [62]. This would agree with the concept that the reaction is structure sensitive and turnover rates would favour smaller particles, although all three outcomes have been observed experimentally. Wei and Iglesia report that with decreasing cluster size of Rh nanoparticles supported on Al_2O_3 or ZrO_2, the rate of activation of the C-H bond in methane increased, also suggesting that smaller clusters have more unsaturated Rh atoms, which are more effective at breaking the C-H bond [63]. Conversely, the conversion rate of methane has also been shown to increase with increasing particle size of Pd nanoparticles up to 20 nm, supported on Al_2O_3 [64]. The trend here is explained by methane oxidation on a Pd/Al_2O_3 catalyst proceeding via a Mars-van Krevelen mechanism. The reactivity is therefore dependent on the Pd-O bond strength. The Pd-O bond is stronger with smaller particles, which stabilises them against redox transformations and so negatively affecting the rate of reaction. The low reducibility of smaller particles leaves fewer vacancies, which is detrimental to the reaction rate of any reaction that proceeds by the Mars-van Krevelen mechanism [21]. It is unlikely the reaction rate would continue to increase with increasing particle size as the conversion of methane is significantly lower on polycrystalline Pd foil [65]. Therefore, in the cases where larger particles are more reactive, there is likely to be an optimum size. A particle size effect on catalytic activity is not always observed, however. Particle size effects are not observed with a Pt/Al_2O_3 catalyst, which performs identically and independently of particle size in the range of 4 – 17 nm [64]. Ribeiro et al. observed only a small change in methane conversion with a Pd/ZrO_2 catalyst, and reported supported

Pd catalysts to be structure insensitive towards the complete oxidation of methane [66].

1.4 An Introduction to NAP-XPS and its Applications

In the last few decades, there has been great focus on developing in-situ characterisation techniques for heterogeneous catalysis. An understanding of the fundamental chemical transformations of a catalyst's surface is key to the development of new, more efficient catalysts. Traditional surface science characterisation techniques, such as x-ray photoelectron spectroscopy (XPS), are carried out under ultra-high vacuum (UHV) conditions, whereby the base pressure of the reaction vessel is $< 10^{-9}$ mbar. Although useful for characterisation of atomically clean and well-defined surfaces, UHV is not a representative condition for catalysis. It has therefore been desirable for a number of years to bridge the so-called "pressure gap" between UHV characterisation methods and industrial batch testing, in order to study the fundamental concepts of catalysis in-situ [67]. The original concept of near-ambient pressure XPS (NAP-XPS) was developed by Hans and Kai Siegbahn, who designed a differentially pumped analyser to keep high pressures contained to the reaction vessel and pumped out of the system before reaching the analyser [68–70]. Siegbahn and Siegbahn's experiments were predominately on liquid samples and organic solvents, and the technique was further developed by Joyner, Roberts and Yates to incorporate solid samples by the inclusion of a sample cell in which the gases were leaked into [71]. Both methods enabled experimental pressures of up to 1 mbar and are still being used today, although pressures up to 25 mbar are now possible due to multiple stages of differential pumping between the reaction chamber and the analyser. Despite being a significant pressure increase on UHV, the workable pressures are limited in this technique due to the attenuation of photoelectrons. The intensity of the spectrum follows a Beer-Lambert law, where I is dependent on the path length the electrons have to travel to get to the analyser and the pressure of the system. The greater number of gas phase molecules the photoelectron has to travel through, the weaker the signal intensity. This is overcome slightly by decreasing the path length, by moving the sample as close to the analyser as possible, but in modern times the use of intense synchrotron radiation as the x-ray source provides a high flux, more focussed spot on the sample to produce more photoelectrons. Thus, the combination of multiple differential pumping stages, small distances between the sample and analyser cone of a small aperture and a high brilliance light source has enabled the collection of high intensity data under pressures up to several mbar [72–75].

Near-ambient pressure XPS (NAP-XPS) is becoming an increasingly popular technique to study catalysts in-situ because of the surface sensitivity of XPS and the ability to mimic catalytic pressures and temperatures. In particular, nano-catalysts are of interest due to their high surface area to volume ratio, resulting in low cost, high performance catalysts. There are many effects to consider in studying nano-catalysts at the fundamental level, such as their redox properties [76], the surface structural modifications during and post-reaction [77] and the surface versus bulk compositions in core-shell nanoparticles [78] under a variety of conditions; all of which contribute to the overall catalytic performance. Jürgensen et al. studied PdO/TiO_2 nanoparticles under ambient pressures of 2-propanol and oxygen to identify the redox behaviour of PdO during the catalytic partial oxidation of 2-propanol to its corresponding carboxylates. Using NAP-XPS, they found that the Pd was predominately in its oxide form (PdO) at 30°C under UHV, but with the addition of 2-propanol and oxygen and heating to 120°C, the PdO reduces to Pd. In the absence of O_2, the PdO starts reducing at lower temperatures, as noted by a shift from high to low binding energy in the Pd 3d region. C 1s spectra revealed the production of carboxylate species from the decomposition of 2-propanol, which occurred only at temperatures after the PdO had been reduced (T >90°C). From this information, the active species of the Pd can be determined, and in this case it appears that metallic Pd is the active species for the partial oxidation of alcohols [76]. NAP-XPS has also been used to study the extent of surface modification and restructuring of surfaces exposed to ambient pressures of gases. A study by Klyushin et al. used NAP-XPS to show how the surface of Au changed in-situ under ozone oxidation [77]. NAP-XPS identified an oxide phase covered the surface of the Au during exposure to O_3, which is thought to mobilise Au atoms and lead to a restructuring of the Au surface. The oxide layer is seen to desorb after O_3 is removed from the system, but the Au 4f spectra show the Au surface to be permanently modified due to low-coordinated Au atoms after O_3 treatment. Core-shell nanoparticles are bimetallic nanoparticles with a core consisting of one metal and a shell consisting of the other. Many industrial processes rely on bimetallic catalysts including catalytic reforming and electrocatalysis in fuel cells, but structural surface changes on the nanometer scale are not fully explained. Tao et al. demonstrate with NAP-XPS how ambient pressures of NO, O_2, CO and H_2 can change the composition and distribution of PtPd and RhPd bimetallic core-shell nanoparticles. Under pressures of up to 200 mTorr, they use different incident photon energies to probe different depths of the surface of the catalyst to give the elemental composition of the core and the shell. The distribution of each metal differs under different gas combinations, determined by quantitative analysis of NAP-XP spectra. They report that, for a RhPd nanoparticle, under oxidising conditions Rh atoms seg-

regate to the shell region, whilst under reducing conditions Pd atoms migrate to the shell region, due to the differing surface energies of each metal oxide under different conditions. RhO_x is more stable than PdO, and so under oxidising conditions it is more favourable for Rh to be at the surface. No distribution changes occur in the PtPd nanoparticles, suggesting that the addition of another metal can affect surface changes, which may in turn affect selectivity and reactivity of a bimetallic catalyst under different conditions [78, 79].

In addition, NAP-XPS has been used to identify how metals behave at the solid/liquid interface under different aqueous environments in order to mimic biological processes and how organic molecules co-adsorb onto surfaces at the equilibrium vapour pressure [80, 81]. It is also possible to study charge transfer in electrochemical cells and at the interfaces of electrocatalysts with NAP-XPS, for research into batteries and fuel cells technology [82, 83]. The kinetic energy of electrons from a negatively biased sample will be higher than those from a positively biased sample, so the kinetic energy shifts in NAP-XP spectra can give non-invasive information regarding local overpotentials across interfaces [67].

Specifically, methane oxidation and exhaust emissions control technologies are not yet well studied with regards to NAP-XPS. Zhu et al. report the surface chemistry changes of a Pd-doped ceria catalyst under 3 Torr of methane and oxygen (CH_4/O_2 = 2). Lab source NAP-XPS studies reveal that the PdO_x reduces to metallic Pd with increased temperature, suggesting that a dominance of metallic Pd is the active phase for partial methane oxidation [84], which is consistent with work on the partial oxidation of methane with Pd/Al_2O_3 catalysts [65]. On a $NiCo_2O_4$ catalyst, Tao and co-workers determine the mechanistic pathway of CH_4 oxidation with NAP-XPS paired with in-situ IR spectroscopy. They follow C 1s and O 1s NAP-XP spectra to identify that CH_4 dissociates to CH_3 on a Ni cation, which oxidises to form CH_3O and then CHO, eventually forming CO_2 and H_2O [85]. In this project, the surface chemistry and modifications of supported Pd catalysts under methane oxidation conditions will be studied using NAP-XPS. The redox properties of the metal and the support material will be determined at various points in the reaction in order to characterise the chemical composition of the catalyst at the formation of each oxidation product. The information gained in these experiments shall provide a more informed insight into how methane oxidation catalysts behave in-situ and help to tune catalysts in the future to positively exploit these characteristics.

2 Experimental Techniques

2.1 Catalyst Preparation Methods

The main objective in preparing an effective catalyst is for the material to have high activity, selectivity and stability. These objectives are usually met by ensuring the material contains a highly dispersed active species with a high surface area [86]. In modern catalysts, the active species is a metal or oxide and high dispersion is obtained by its deposition onto a porous support material with high thermal stability [87]. The support material is usually an inorganic oxide; Al_2O_3, SiO_2, TiO_2, CeO_2 and ZrO_2 are all common catalytic support materials, although activated carbon is also a popular choice of support due to its chemical inertness, high surface area and low costs [88]. Transition metals exhibit excellent catalytic activity due to their ability to change between oxidation states, and in particular the platinum group metals (PGMs), which include Pd, Pt, Rh and Ru, are used as the active metal species for methane oxidation reactions [32, 35, 89, 90]. The preparation of a catalyst first involves the formation of the primary solid, or the supported-metal particles, followed by drying to remove aqueous material after precipitation, and lastly thermal treatment to remove unreacted precursors and to control particle size of the metallic nanoparticles. This section aims to highlight and discuss the different techniques used to prepare supported PGM catalysts.

2.1.1 Co-Precipitation

The technique used to prepare most of the catalysts studied in this work was the co-precipitation method, whereby the active phase of the catalyst (metallic nanoparticles) and the support material are precipitated out together from a homogeneous liquid medium. The formation of nanoparticles occurs by nucleation, in which the system is far from equilibrium causing the formation of elementary particles, followed by growth, where the particles can agglomerate to approach equilibrium. The particles are then filtered from the mother liquor to yield the final solid [86, 91, 92].

To synthesise the supported-metal catalysts, a molar excess of $Pd(NO_3)_2$ was added to a colloidal suspension of dodecenyl succinic anhydride in tetrahydrofuran (THF) and a base solution of aqueous Na_2CO_3. The colloidal suspension helps to control particle size and prevent too much agglomeration, in a similar way colloids aid growth in the sol-gel preparation method [93], and the addition of the base neutralises the palladium salt to encourage nucleation. The support material is added, stirred for 24 hr to bind with the Pd nanoparticles, and the catalytic solid is washed, filtered and dried.

The particle size of the metal nanoparticles is controlled by a thermal treatment called calcination. Calcination temperatures are usually between 300 – 1000 °C and aim to decompose and remove any impurities in the catalyst leftover from the synthesis. The high temperatures will also cause further agglomeration of nanoparticles, and the higher the temperature the greater the rate of agglomeration. Therefore, higher calcination temperatures will yield larger nanoparticle sizes. The catalysts are aged for 2 – 4 hours, which gives enough time to control the particle size uniformly throughout the catalyst.

2.1.2 Incipient Wetness Impregnation

An alternative synthesis method for supported-metal catalysts is to impregnate the support directly with a metal precursor salt. The incipient wetness impregnation, or dry impregnation, method uses the same volume of metal precursor solution as the pore volume of the support material [92,94,95]. $Pd(NO_3)_2$ was used again in this case as the precursor for supported-Pd catalysts, and a concentrated aqueous solution was added and mixed to the support material (either Al_2O_3 or SiO_2) until the pore volume was filled. The catalysts are calcined to 600 °C to remove the nitrate precursor.

The weight percent metal loading can be calculated prior to synthesis to ensure the correct amount of precursor is used. For example, to make 20 g of a 5 wt% Pd catalyst from a 15.11% assay of $Pd(NO_3)_2$, the following calculation is used:

5% of 20 g = 1 g of Pd and 19 g support material (e.g. Al_2O_3)

$\frac{1 \times 100}{15.11}$ = 6.62 g of $Pd(NO_3)_2$

In this case, to achieve a 5 wt% Pd loading, 6.62 g of $Pd(NO_3)_2$ precursor should be used.

2.2 X-Ray Photoelectron Spectroscopy

X-ray photoelectron spectroscopy (XPS) is a surface sensitive characterisation technique that can detect all elements except H and He, the state of chemical bonding, and provide information up to a depth of 10 nm [96,97]. The fundamental principles of XPS are based on the "Photoelectric Effect", first discovered in 1888 by Wilhelm Hallwachs [98] and later clarified by Albert Einstein in 1905 who described how high frequency radiation can eject electrons from a material. The kinetic energy of these electrons is related to the frequency of the incoming radiation (photons), the work function of the emitting material, and the binding energy of a hole state to form the relationship:

$$h\nu = E_{kin} + E_b + \phi \tag{2.1}$$

where h is Planck's constant and ν is the frequency of the incoming x-ray (photon energy), E_{kin} is the kinetic energy of the emitted electron, E_b is the binding energy and ϕ is the work function [99]. A schematic diagram of the XPS process is shown in Figure 2.1, whereby an electron from a core energy level (E_1) is ejected into the vacuum. The binding energy (E_b) is an intrinsic property of each element, thus making XPS a suitable technique for elemental analysis [100].

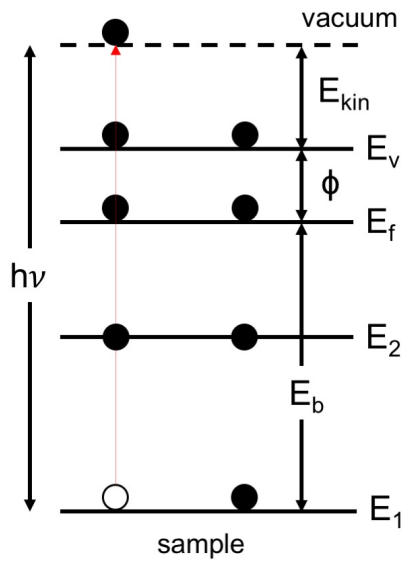

Figure 2.1: Schematic diagram of the XPS process showing a core electron from the sample ejected into the vacuum. E_f and E_v denote the Fermi level and the vacuum level respectively.

Photoelectrons emitted from the sample and into the vacuum have an inelastic mean free path (IMFP) of 10 – 100 Å in solid matter, depending on their kinetic energy, which is defined as the distance an electron can travel before the intensity of the electrons, which have not undergone energy loss, decays to $1/e$ of its initial value [101]. After the photoelectrons pass through the aperture to the analyser, they are focussed into an electron beam by a series of lenses. The analyser itself is hemispherical in shape, with a negative voltage on the outer hemisphere and a positive (or less negative) voltage on the inner hemisphere. Electrons will only reach the detector on the other side of the hemisphere if their kinetic energies (E_{kin}) are:

$$E_{kin} = e\Delta V(\frac{R_1 R_2}{R_2^2 - R_1^2}) \tag{2.2}$$

where e is the charge on the electron, ΔV is the potential difference between the hemispheres and R_1 and R_2 are the radii of the inner and outer hemispheres respectively [102], although this is only true for electrons that enter the hemisphere on and tangential to the axis. To account for varying electron trajectories, the electrons are subjected to a retarding voltage as they enter the analyser, bringing them to the same focal point at the entrance slit. A schematic diagram of a hemispherical analyser is shown in Figure 2.2.

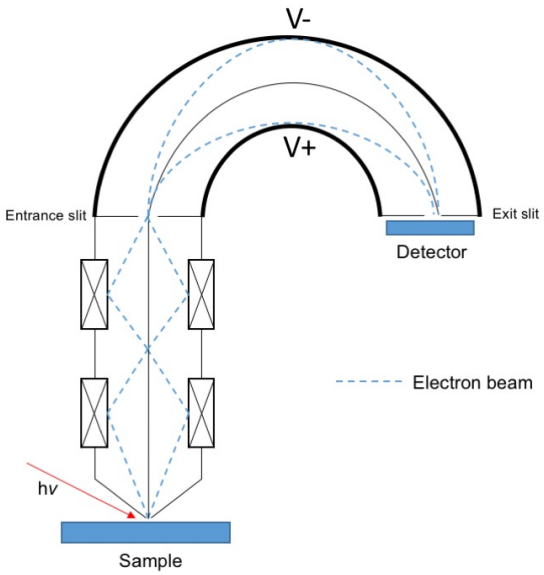

Figure 2.2: Schematic diagram of the inside of a hemispherical XPS analyser. Two different angular trajectories that both arrive at the same focus and energy in the analyser are shown.

2.2.1 Ultra-High Vacuum

Surface science studies, including XPS and electron microscopy, require operation under base pressures of $< 10^{-8}$ mbar, otherwise known as ultra-high vacuum (UHV). In particular, UHV is desired for electron spectroscopy for the following reasons [96]:

1. To reduce inelastic scattering of photoelectrons by gas molecules in between the sample and the analyser
2. To keep the sample clean and free of contaminants from the gas phase that could distort or attenuate the spectra
3. To protect instrumentation inside the spectrometer

The XPS signal intensity, I, is proportional to $e^{-(\sigma dp)}$, where d is the distance the electrons travel through at pressure p and σ is the cross-section of the scattering [103]:

$$I \sim e^{-(\sigma dp)} \tag{2.3}$$

It is for this reason that p should be minimised in order to increase signal intensity and decrease inelastic electron scattering. Although not too important for supported-nanoparticle catalysts, as such samples do not require sample cleaning, UHV helps to keep samples clean from contaminants in the gas phase because the sticking probability of a gas molecule to the surface of a sample is related to the surface coverage [104]. Langmuir's adsorption isotherm says simply that increased pressure will give increased surface coverage, because the pressure of the adsorbate is related to the volume of the adsorbate adsorbed onto a substrate, assuming the adsorbate behaves as an ideal gas and the substrate has enough vacant surface sites [105]. Thus, low pressures inside the spectrometer are essential to keep monolayers of unwanted gas molecules forming on the surface. UHV is achieved by high speed turbo molecular pumps assisted by ion and titanium sublimation pumps, which remove gas molecules from inside the chamber [102]. After opening the chamber to introduce a sample, a bake-out is performed, in which the spectrometer is coated in baking tapes or tents, and heated to ∼140 °C to remove water.

2.2.2 Spin-Orbit Splitting

A feature of orbitals with an angular momentum quantum number (l) > 0 is a splitting of the core-level peak [97], due to the coupling of the electron spins. The different binding energies of each spin-split is defined by the total angular momentum quantum number, J, and the peak areas of each spin-split are a fixed ratio dependent on the subshell (Table 2.1) [106].

Subshell	l	J	Peak area ratio
p	1	3/2, 1/2	2:1
d	2	5/2, 3/2	3:2
f	3	7/2, 5/2	4:3

Table 2.1: Angular momentum quantum numbers for the subshells p, d and f and their corresponding XPS peak area ratios.

In Figure 2.3, a Pd 3d XPS spectrum is shown to have two peaks, arising from the 5/2 and 3/2 spin-orbit coupling associated with the d subshell. The peak area ratio between the Pd $3d_{5/2}$ (low binding energy) peak and the Pd $3d_{3/2}$ (high binding energy) peak should be 1.5, in accordance with the ratios in Table 2.1.

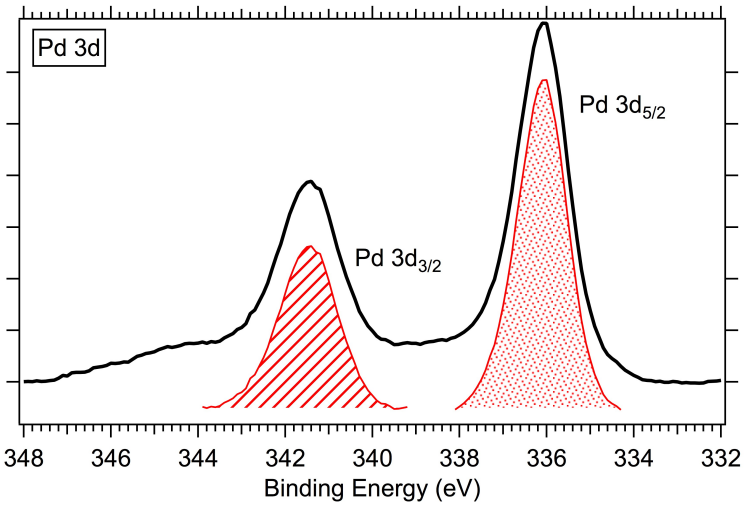

Figure 2.3: Pd 3d XPS spectrum showing both 5/2 (dotted peak) and 3/2 (striped peak) spin-splits. Area of Pd $3d_{3/2}$ = 52.1, area of Pd $3d_{5/2}$ = 90.9, area ratio = 1.7.

2.2.3 Chemical Shifts

The binding energy of a photoemitted electron (E_B) is defined as the difference in the energy of the initial state electron N wavefunction and the energy of the final state, or ionised, electron $N-1$ wavefunction [107]:

$$E_B = E^{N-1} - E^N \tag{2.4}$$

From Equation 2.4, it is apparent that both initial state energy and final state relaxation affect the binding energy of the resulting spectral line. The initial and final states are affected by the changes in the valence electronic structure of the atom, before and after the emission of a electron. Although the core electrons do not take an active part in bonding, they are strongly affected by the valence electron distribution and the local electronic environments [108], and binding energy shifts of up to several eV for the same element are often observed [98]. Therefore, XPS can be used to analyse the chemical composition of a surface in more detail than simply elemental composition.

The exact binding energy of an emitted electron depends on the core level it is ejected from, the oxidation state of the atom it is ejected from, and its chemical and physical surroundings. For atoms with more positive oxidation states, the emitted electron would experience greater attraction from the nucleus of the atom due to fewer valence electrons [100]. This initial state effect will result in a higher binding energy than for atoms of the same element with a lower oxidation state. To be able to distinguish between different oxidation states is key to identifying the nature of the chemical state of nanoparticles. For example, it is possible to determine whether a Pd nanoparticle is in an oxide state or a metallic state by the binding energy value. In the Pd $3d_{5/2}$ region, a metallic Pd (Pd^0) peak occurs at 335.0 – 336.0 eV and a PdO (Pd^{2+}) peak occurs at 336.0 – 337.0 eV. Higher oxidation states of Pd, such as Pd^{4+} in PdO_2, have a $E_B >$ 337.0 eV [109]. High resolution XPS is often needed to resolve different oxidation states and this is achievable with synchrotron x-ray sources (see Section 2.3.2). Smaller binding energy shifts are also observed between bulk atoms and surface atoms, known as surface core level shifts (SCLS). Atoms at the surface of a crystal or nanoparticle are less coordinated than those in the bulk and as a result, the valence bandwidth is narrowed leaving a redistribution of charge on the surface. This change in potential is responsible for the shift in binding energy for surface atoms, compared to bulk atoms, which is typically less than 1 eV [110]. This effect is observed by Baetzold et al. for different crystallographic orientations

and reconstructions of Pt single crystal surfaces. They report a 0.4 eV SCLS to lower binding energy for a Pt{111} surface, and two SCLS shifts for a Pt{110}-(1x2) reconstructed surface (0.55 eV and 0.21 eV), which correspond to the two different types of co-ordination site on the reconstructed surface [111].

The molecular bonding also affects the binding energy, and in some cases the nature of the molecular environment can shift the binding energy of the same element by up to 10 eV [98]. This is particularly seen in C 1s spectra when different carbon species are present. Figure 2.4 shows a NAP-XPS spectrum in the C 1s region taken in the gas phase of 0.22 mbar CH_4 and 0.11 mbar O_2. In this case, a Pd/SiO_2 sample was used as the catalyst and the reaction products, CO and CO_2, can clearly be seen at two different positions on the binding energy scale. Unreacted CH_4 appears as a peak at 284.5 eV, whilst oxidised carbon appears at higher binding energies with CO at 289 eV and CO_2 at 291 eV.

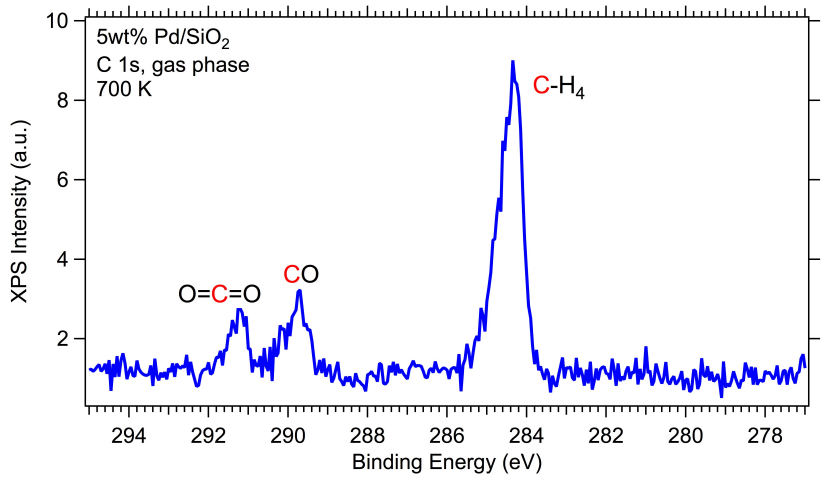

Figure 2.4: NAP-XPS C 1s spectrum taken in the gas phase under 0.22 mbar CH_4 and 0.11 mbar O_2 at 700 K showing the binding energy shifts of different carbon-containing molecules. $h\nu$ = 400 eV.

The high electronegativity of the C≡O bond, compared with the non-polar C-H bond, causes a shift towards higher binding energy. Highly electronegative molecules, such as CF_3, appear at higher binding energies than non-electronegative molecules of the same element (i.e. CH_4). In the cases of different molecular bonding, final state effects are dominant. The equivalent core approximation describes these effects as the ionised atom as a result of photoemission replaced by a neutral, unionised atom of the element with Z+1. The addition of one electron from the neutral atom creates a strain on the molecule and thus increases its overall energy. The differences in the strain energies due to different molecular configurations are the cause of the differences in binding energies for the same element [98].

2.2.4 Other Final-State Effects

A typical XPS spectrum will exhibit sharp core level peaks representative of the elements in the irradiated sample over a background of inelastically scattered electrons in the order of 10^3 counts per second, depending on the x-ray source . The binding energy is the difference between the initial and final state of the core electron, and so final state effects such as shake-up satellites, multiplet splitting and plasmon excitations are also possible features of photoelectron spectra. Shake-up satellites occur when the ejected core electron couples with a valence electron, which promotes the core electron to a higher energy level (Figure 2.5). This leads to an overall kinetic energy loss and therefore weak spectral intensity is seen at a higher binding energy than the unaffected core level electrons, which may give rise to an asymmetric line shape (Figure 2.6) [112].

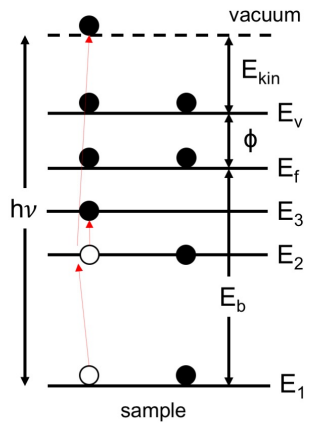

Figure 2.5: Schematic diagram of the "shake-up" process.

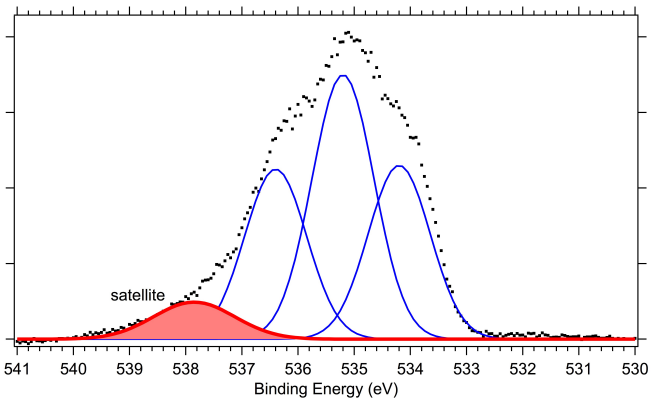

Figure 2.6: X-ray photoelectron spectrum in O 1s region showing satellite peak (filled red) resulting from the "shake-up" process. Raw data shown as black dotted line, fitted peaks at blue solid lines. $h\nu$ = 650 eV.

Plasmon excitations are energy losses resulting from oscillations in the conduction band induced by the ionised core electron, however these are only generally a feature of clean metal surfaces [113]. After electron excitation, the atom is unstable as a result and looks to return to a more stable state. Known as relaxation, the electron density rearranges and redistributes by the transfer of an electron from a high energy state to a lower energy state. Consequently, the positive charge left behind from the emitted electron is screened and so the binding energy is decreased. Screening, or shielding, from positive charge resulting from electron loss can affect the core-level shift and the overall binding energy of the peak depending on the extent to which the photoelectron is screened. This can be particularly apparent in samples containing small nanoparticles (< 2 nm) that are typical of catalyst samples. Small nanoparticles tend to have a reduced ability to screen the aforementioned positive charge, resulting in greater attraction between the photoelectron and the parent atom. This would in turn result in the peak in the photoelectron spectrum shifting towards a higher binding energy, as compared with a nanoparticle of a greater diameter, for example [114]. Other final-state effects such as peak broadening may also be observed either due to vibrational excitations as a result of photoionisation or from sample charging [98, 104, 115].

2.2.5 Background Subtraction

The final-state effects discussed in Section 2.2.3 can be useful in analysing particular chemical environments of elemental species, but often simply contribute to the background noise resulting in a higher background at higher binding energies (low kinetic energies). The background intensity should be subtracted in order to show the XPS features in detail. Background subtraction can either be linear (Figure 2.7a), in which a straight line is drawn between two user-defined points a few eV either side of the peak, or step-like, whereby a Shirley background is employed (Figure 2.7b) and information about the spectrum is used to define the line of the background [116]. After background subtraction, the peaks are fitted using a custom fit function that is discussed in detail, including examples, in Chapter 3.

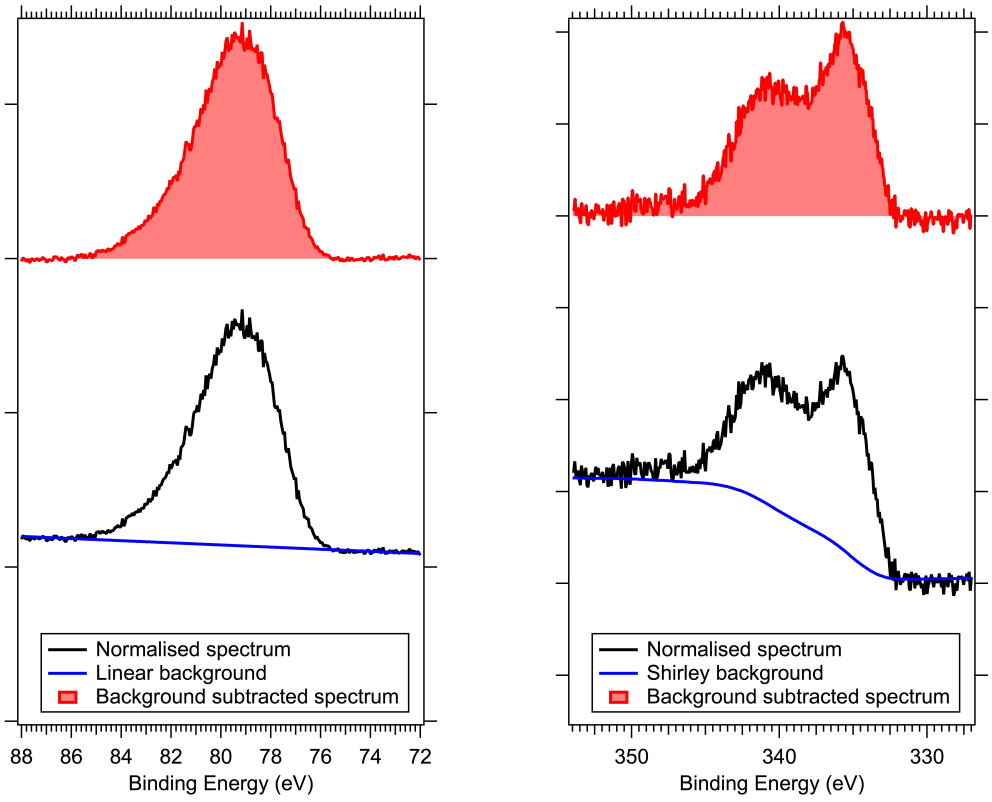

Figure 2.7: (a) XPS spectrum corrected with a linear background subtraction and (b) XPS spectrum corrected with a Shirley background subtraction. $h\nu$ = 450 eV.

2.3 X-Ray Sources

2.3.1 Laboratory Sources

Soft x-rays are used in photoelectron spectroscopy because they have energies in the range 100 – 2000 eV, the minimum energy needed to excite core electrons. X-rays used in XPS are either laboratory sources or synchrotron light sources. X-rays from a lab source are generated by bombarding a metallic anode with high energy electrons. The most common anodes used are Al or Mg that give x-rays with photon energies of 1486 eV and 1254 eV respectively, each producing Kα radiation [117]. Both Al Kα and Mg Kα x-rays have naturally narrow line widths (0.6 – 0.8 eV), although with the introduction of a monochromator the line widths can be reduced to 0.2 – 0.3 eV [98]. The disadvantage of lab source x-rays is the fixed photon energy $>$1000 eV. Referring back to Equation 2.1, high photon energies will give high kinetic energies, and lower cross-sections at low binding energies. As a result, the surface sensitivity of the method and the overall resolution of the spectrum are also reduced [118].

2.3.2 Synchrotron Radiation

An alternative way to produce x-rays is with synchrotron radiation, which is based on the principle that when electrons are accelerated and forced into a curved trajectory they emit radiation [119]. In modern day synchrotrons, electrons are injected into a vacuum ring from an electron gun and accelerated via a series of particle accelerators. Once they are travelling at almost the speed of light, the electrons are released into the main storage ring where they reach energies up to 3 GeV. The electron beam is forced around the ring by magnets, and at each magnet the resulting radiation is tunnelled through a beamline, eventually ending up in an experimental chamber. To date, there are four generations of synchrotron light sources [120]. First generation synchrotrons were primarily used for elementary particle physics and the synchrotron radiation itself was used parasitically as beams for low energy physics experiments. The second generation of synchrotrons were storage rings fully dedicated to the use of synchrotron radiation [121]. In the 1990s, the operation of third generation synchrotrons began, which introduced insertion devices into the storage ring. Insertion devices, otherwise known as wigglers or undulators, consist of a series of dipole magnets of opposite poles that oscillate the electrons as they pass through. The resulting x-ray beam is narrower and more intense, owing to the increased brilliance of the x-ray beam [122, 123]. Brilliance is a measure of the spectral brightness or beam intensity and the

brilliance of a beam produced by a typical undulator is 10^{18} – 10^{19} photons/(s·mm^2·mrad·0.1% bandwidth); 8 to 10 orders of magnitude higher than a laboratory source [98]. The brightness and coherence of the beam is set to improve in fourth generation light sources, in which the photons are concentrated into tighter bunches and pulsed in the sub-picosecond range. This leads to a brilliance in the 10^{23} photon range and considerably faster data acquisition [124, 125].

Synchrotron radiation has many advantages over laboratory x-ray sources including high brilliance, high photon flux and fast data acquisition, but another is the ability to tune the photon energy. In order to maximise the photoionisation cross-section, or the probability of electron emission, the photon energy may need to be tuned to give the required kinetic energy. The photon energy range is dependent on the gap between magnets of an undulator, which can be reduced or increased in order to find the desired photon energy range. A monochromator grating within the beamline further tunes the photon energy to a more specific value with up to 0.1 eV resolution [126].

2.4 NAP-XPS

The reasons for using UHV-XPS as discussed in Section 2.2.1 are applicable for surface science experiments that require a clean surface, such as for the characterisation of molecules on single crystal substrates or model catalysts [127–130]. For well characterised "real" catalysts, such as supported-nanoparticles, there is no benefit in UHV. By nature, catalysts are involved in reactions and so the question to answer is how the surface chemistry of the catalyst is affected by the progressing reaction. Near-ambient pressure x-ray photoelectron spectroscopy (NAP-XPS) is an emerging tool for probing the surface of samples with x-rays whilst under pressures of small molecules up to 10 mbar [131], making it an excellent method for studying catalysts under near-reaction conditions.

NAP-XPS spectrometers differ from those used for conventional UHV-XPS by the insertion of a differential pumping system between the hemispherical analyser as depicted in Figure 2.2, and the reaction chamber. A differential pumping system is a series of apertures and pumps that, as the reaction gases pass through, gradually decreases the pressure from the mbar range to an analyser-safe 10^{-8} mbar (Figure 2.8).

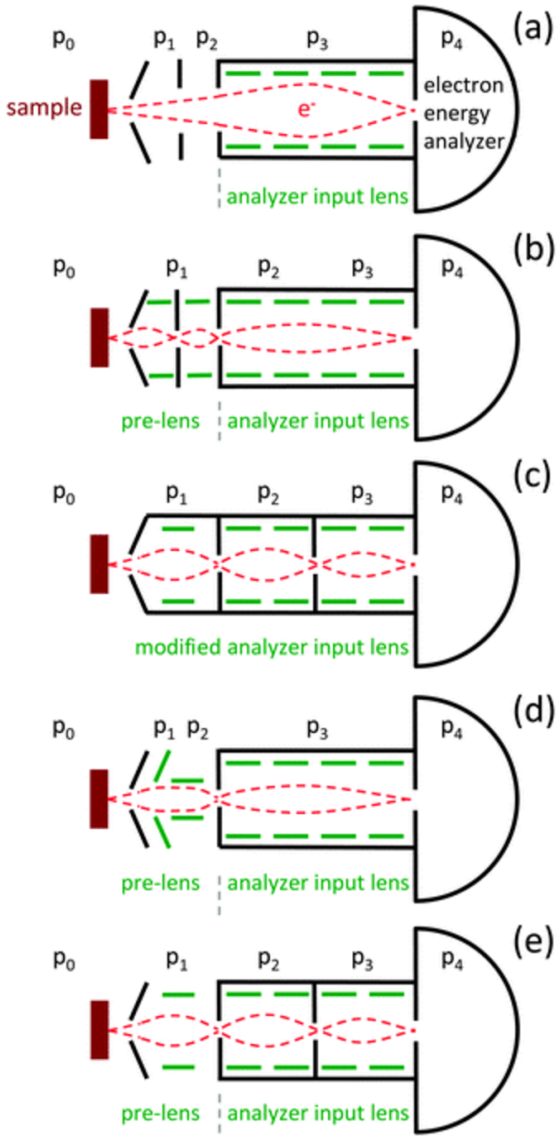

Figure 2.8: Various differential pumping set-ups used in NAP-XPS analyser systems. The most basic system in (a) shows two differential pumping stages between the sample and the first aperture to the analyser lens. Figures (b) to (e) show more sophisticated systems with smaller apertures that reduce pressure differentials and focus electrons in smaller angles. Image taken with permission from [103] - published by the Royal Society of Chemistry.

Gases are introduced via leak valves, gauged either manually or electronically by mass flow controllers. The gases can either leak directly into the analysis chamber after shutting off all pumps, as at beamline 9.3.2 at ALS (Figure 2.9a) [132] and the CIRCE beamline at ALBA [133], or into a small sealed reaction cell containing the sample inside the analysis chamber as at the SPECIES beamline at MAX IV (Figure 2.9b) [134].

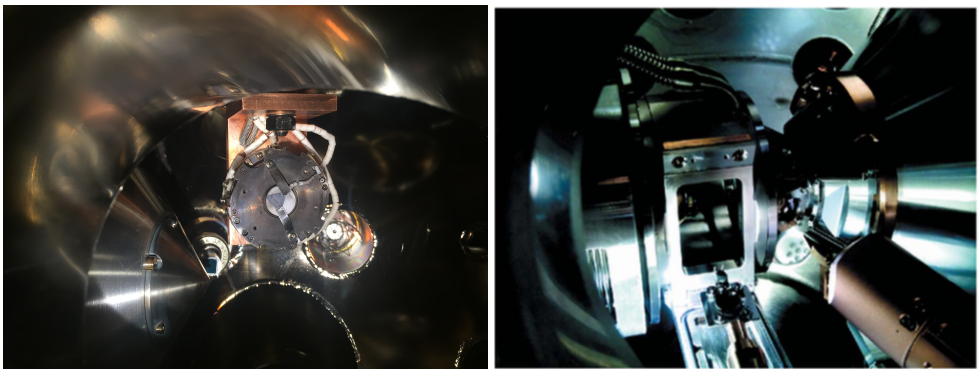

(a) **(b)**

Figure 2.9: Photographs of different NAP-XPS sample holders. (a) Inside the NAP-XPS chamber at ALS 9.3.2. (b) The NAP reaction cell at SPECIES MAX IV, taken with open-access from [134].

Equation 2.3 refers to the relationship between pressure and signal intensity, as inelastic scattering is increased with increased pressures. This effect is minimised under UHV conditions, but in NAP-XPS experiments the pressure is orders of magnitude higher and inelastic scattering becomes an issue. The signal intensity is also dependent on the distance between the sample and the analyser, because an increased distance for electrons to travel would decrease the probability of an electron reaching the aperture. Thus, for ambient-pressures, d, the distance between the sample and the analyser aperture, should be minimised (typically 1 mm) and for higher values of p, I will be lower and therefore yield a weaker signal [103]. In the case of the reaction cell set-up, the cell is pushed directly up to the analyser nozzle and sealed, which can be seen in Figure 2.9b.

2.5 Temperature Programmed XPS

In both UHV and NAP-XPS experiments, temperature programmed XPS (TP-XPS) is a useful tool to identify at what temperatures certain surface composition changes occur such as an change in oxidation state or desorption of molecules [101, 135]. TP-XPS experiments involve the collection of fast spectra during a linear temperature ramp, either heating or cooling. The result is a two-dimensional image of binding energy (x-axis) versus temperature (or time) (y-axis) versus XPS intensity (z-axis), where the intensity is represented by a colour scale. In this work, TP-XPS was used on both heating and cooling of the sample in UHV and ambient pressures in order to determine a relationship between temperature and sample conductivity. This is discussed in more detail in Chapter 3.

2.6 Mass Spectrometry

Based on the principle that the extent to which a molecular ion is deflected in an oscillating electrical field is dependent on its molecular mass [136], the abundance of different gases in a mixture can be detected by mass spectrometry. A quadrupole mass spectrometer starts by ionising the gas sample and accelerating the resulting positive ions to the same kinetic energy. Oscillating electric fields deflect the ions, depending on mass to charge (m/z) ratio. Ions with a greater m/z ratio will be deflected to a lesser extent than ions with a smaller m/z ratio, and the ions that reach the detector are counted, amplified and charted as intensity versus m/z [137]. This is a particularly useful tool for characterising the abundance of reactants and products present in a gas phase reaction, and hence determining the activity of a catalyst.

Catalytic activity data obtained by mass spectrometry can complement the information obtained by NAP-XPS regarding the surface chemistry of a catalyst under reaction conditions. Correlating the two sets of data firstly ensures the reaction is taking place, and also identifies which surface state is the most active or selective to different products. Many NAP-XPS set-ups include a mass spectrometer in the differential pumping stage that can detect gas molecules as they are pumped away from the analysis chamber. The values for partial pressures of different gases obtained from mass spectrometry can be used to quantify the amounts of reactants being used and products being formed. Chapters 4, 5 and 6 present mass spectrometry data that show the percentage conversion of reactant gas methane to its oxidation products. The integer masses of the reactant gases, CH_4 (16) and O_2 (32) are also monitored along with the integer masses of the possible oxidation products; CO_2 (44), H_2O (18), H_2 (2) and CO (28). The quantification of different oxidation products at different temperatures can be correlated to the NAP-XPS data, and the active state of the catalyst for different oxidation reactions is determined. Mass spectrometry data can also be used to distinguish the relative reactivities of different catalysts under the same conditions, by comparing the onset temperatures of each product. In addition, monitoring the partial pressures of each gas on cooling will identify whether the reaction is reversible or not, or if any hystereses are observed. Furthermore, taking the natural log of the partial pressure and plotting as a function of 1/T in an Arrhenius plot, the activation energy of each product formation in a first order reaction is given by the gradient of the straight line. Activation energies can give a more quantitative view on catalytic reactivity and insight into the reactions occurring at each temperature range.

3 Experimental Procedures

Abstract

Insulating materials have been a major problem for research into supported metal catalysts with x-ray photoelectron spectroscopy. Common catalyst supports are often insulators, including alumina and silica. At synchrotrons, in the absence of charge compensation methods, insulating materials will charge and hence disrupt the resulting spectra. It is for this reason that only model catalysts have been tested thus far with synchrotron XPS, with very few experiments in the literature discussing "real" catalysts in this way.

This chapter discusses how the high resistivity of insulators in Pd/Al_2O_3 and Pd/SiO_2 catalysts can be overcome by using doped substrates and increased temperatures (> 450 K) to activate ionic conduction. The activation energies of the movement of charge carriers for Pd/Al_2O_3 and Pd/SiO_2 catalysts under UHV and ambient pressures are calculated by observing the binding energy shift in a temperature-programmed XPS spectrum.

Despite an increase in conductivity of the support material at higher temperatures and a significant improvement in the spectra stability, there are still residual effects of charging in the Al 2p and Si 2p spectra. These effects, including peak broadening and splitting, should be taken into account when fitting the Pd 3d spectra. Therefore, a custom fitting procedure has been developed that takes into account these unusual features of the support material spectra, which is also explained in detail.

3.1 Conductivity of Insulating Supports

Sample charging is a common drawback in XPS measurements of non-conducting samples [104]. Sample charging is the result of a lack of surrounding electrons compensating for photoelectrons ejected from the sample and into the vacuum. In conductors, these emitted electrons are replaced by electrons from the conduction band. However, in insulating materials the band gaps are usually too large to facilitate movement of electrons from the valence band to the conduction band and so the emitted electrons are not replenished. This imbalance between ejected electrons and replacement electrons causes a build up of positive charge [138].

X-ray induced primary and secondary electron emission (SEE) is a process that occurs within a material as a result of x-ray ionisation and the photoelectric effect. SEE is often responsible for sample charging due to the positive charges resulting from the electron emission [139]. The photoelectric effect says that when a material is ionised by a light source, a photoelectron is emitted, followed by an Auger electron, into the vacuum [115]. Secondary electrons are produced as a result of inelastic interactions of the primary electrons and the subsequent electron holes they create and, due to the loss of negative charge in the sample with no neutralising charge, their emission is a major cause of charging in insulating samples [139–141]. This can affect the resulting spectra in ways that make for difficult analysis and so charge compensation methods are usually implemented during XPS experiments.

3.1.1 Charge Compensation Methods

Laboratory electron spectrometers are equipped with charge compensation methods in order to eliminate surface charging. A commonly used technique in laboratory x-ray sources is a low energy electron flood gun, which bombards the sample with electrons ($\sim$ 6 V) that replenish the negative charge lost by photoelectron and secondary electron emission [142, 143]. In a conducting sample, the kinetic energy of the photoelectron (E_k) is calculated by:

$$E_k = h\nu - E_B - \phi_s \tag{3.1}$$

where $h\nu$ is the incident photon energy, E_B is the binding energy and ϕ is the workfunction of the spectrometer. In an insulating sample, residual charge on the surface must be considered:

$$E_k = h\nu - E_B - \phi_s - \frac{\Delta E}{e} \tag{3.2}$$

where $\frac{\Delta E}{e}$ is the electrostatic potential created by sample charging [96, 144].

Figure 3.1 shows XPS spectra of the same Pd/Al_2O_3 sample with the flood gun turned both on and off in the Pd 3d region. The difference in energy (ΔE) between the spectrum taken with the flood gun off and the spectrum taken with the flood gun on is 9.9 eV. The spectrum taken with charge compensation methods in place should see no effect from charging. However, the spectrum taken without any contribution from the flood gun exhibits sample charging, evident by the positive shift in binding energy.

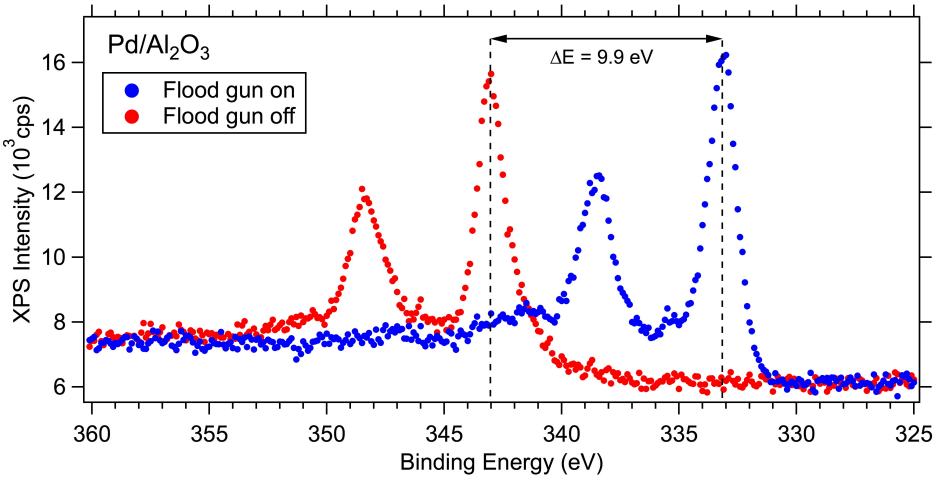

Figure 3.1: Raw ESCA spectra of Pd/Al_2O_3 catalyst in the Pd 3d region with the flood gun on (blue dots) and flood gun off (red dots). $h\nu$ = 1486 eV.

Despite the frequent use of flood guns with laboratory x-ray spectroscopy, XPS chambers at synchrotron facilities are not usually equipped with any charge compensation apparatus and it is for this reason that insulator-supported catalysts have barely been tested with synchrotron XPS. Considering that x-rays produced from synchrotron light have a photon flux orders of magnitude higher than x-rays from a laboratory source [145], the effect of sample charging is much greater. Provided the binding energy shift of the uncompensated spectrum is stable, the binding energy can be shifted back by the same value as that of the key element in the support (e.g. Al 2p in Al_2O_3 supported samples) or by adventitious carbon (C 1s) that is adsorbed onto the sample, but plays no role in the chemistry of the system [104]. However, the binding energy shift is not the only artefact of sample charging, and so it is beneficial to have

another charge compensating method in place to help minimise any peak broadening and splitting that may arise from sample charging.

To improve the conductivity of an insulating sample without a flood gun, other methods must be considered. A common way to improve conductivity is by doping the sample with atoms that create extra states within the band gap. Carbon is a common dopant used to improve the conductivity of insulators, however it is not known how the carbon may interact with the catalyst under reaction conditions. Another way to enhance sample conductivity is to modify how the sample is mounted. Supported catalysts are often in powder form, which can be adhered or pressed into a conducting substrate. Double-sided carbon tapes are often used to stick powdered samples onto, and as long as the layer of adhered catalyst is thinner than the penetration depth of the x-ray beam, the carbon from the tape will provide a conducting effect. Likewise, powders can be pressed into indium foil; a substrate with a low hardness and high conductivity [146]. However, the melting temperatures of both indium and the acrylic adhesive in carbon tapes are 157°C [147] and 60°C respectively. In the case of methane oxidation catalysts where the reaction temperature exceeds 300°C, these materials are not suitable. Therefore, for methane oxidation catalysts, it is necessary to choose a substrate with a high melting point, as well as high conductivity.

3.1.2 Sample Preparation for Synchrotron XPS

The supported Pd catalysts in this work were mounted for synchrotron XPS onto an n-type Si {111} wafer substrate [65]. A non-doped silicon wafer has a resistivity of 100 – 3000 Ωcm at room temperature, but the inclusion of a phosphorus dopant significantly decreases the resistivity to 10^{-3} – 40 Ωcm [148]. With a melting point of 1410°C, an n-type Si {111} wafer with phosphorus as dopant (Sigma-Aldrich) was selected.

A 1 × 1 cm piece of silicon wafer was taped onto a hot plate set to 100°C, as a 3:1 aqueous suspension of the catalyst in its powder form was prepared. The suspension was then poured into a spray gun, fitted to a compressed air outlet, and sprayed onto the silicon wafer for 10 s. The water immediately evaporated to leave a thin and reasonably homogeneous layer of nanoparticles on the surface of the silicon. Optical microscope (Figure 3.2a) and SEM (Figure 3.2b) images show the homogeneity of a spray coated Pd/Al_2O_3 layer on a silicon wafer.

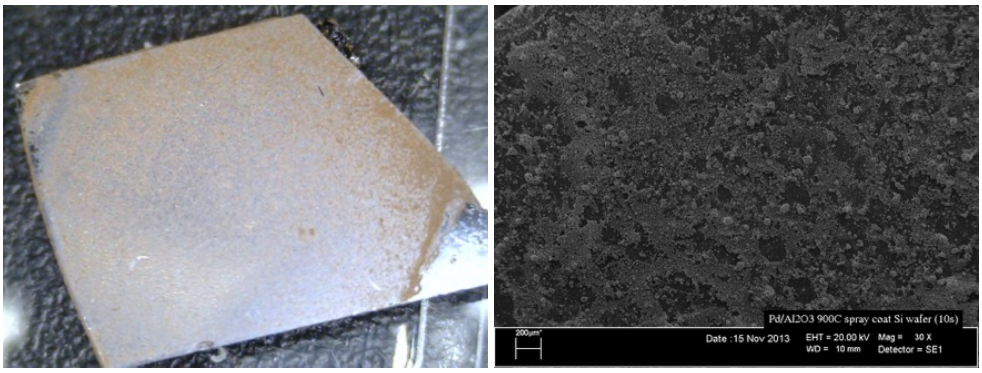

(a) Optical **(b)** SEM

Figure 3.2: Optical microscope image (a) and SEM image (b) of a silicon wafer spray coated with Pd/Al_2O_3 catalyst

The layer of catalyst was kept thin to not only ensure the conducting effect of the substrate, but also to provide a stronger contact between the catalyst and the wafer.

3.1.3 Activation Energies of Charge Carriers

Despite considerations into how the sample was mounted for synchrotron experiments, the catalyst samples still exhibited signs of charging under synchrotron light at room temperature. XPS spectra taken under UHV conditions at room temperature showed the binding energy of the Al 2p peak to have shifted by approximately 30 eV. Temperature-programmed XPS taken under UHV conditions show the temperature effect on sample charging and can be related to the band gap. In Figure 3.3, TP-XPS in the Al 2p region show how the binding energy of the peak shifts as a function of temperature. On heating (Figure 3.3c), the Al 2p peak shifts back by 20 eV from 350 – 450 K. After 450 K, the peak is stable, only shifting a few eV up to 800 K, and close to the literature value of 74.5 eV [149]. The effect is reversible on cooling: Figure 3.3a shows a stable Al 2p peak close to the expected binding energy value, but around 550 K the peak appears to broaden and shift.

The temperature dependence of sample charging and peak shifting would suggest there is an activated process, in which upon heating charge carriers become more mobile. For the case of ionic conductivity, a certain activation energy is needed for sufficient availability of ions, which is typically in the range of $<$1 eV. The valence band to conduction band transitions require 5.5 – 9.3 eV for SiO_2 [150, 151] and 8.7 eV for Al_2O_3 [152]. This activation energy (E_a) is determined by an Arrhenius equation:

$$N_c \sim e^{(-E_a/kT)} \sim \sigma \tag{3.3}$$

where N_c is the number of charge carriers, k is the Boltzmann constant in eV K^{-1} and σ is the conductivity of the sample. The binding energy shifts in XPS spectra caused by sample charging (ΔE_B) can be used to determine σ, due to the relationship:

$$\Delta E \sim R \cdot I \sim \frac{I}{\sigma} \tag{3.4}$$

where R is the resistance of the sample and I is the emission current. The Arrhenius plots in Figures 3.3b and 3.3d show $ln(\Delta E_B)$, where E_B is the binding energy shift from the uncharged peak, as a function of inverse temperature for sample cooling and heating respectively. Both plots can be fitted with a straight line, of which the gradient is E_a/k. The activation energy required to neutralise the sample (E_a) is calculated to be 0.3 eV under both sample heating (3.91% error) and cooling (2.48% error).

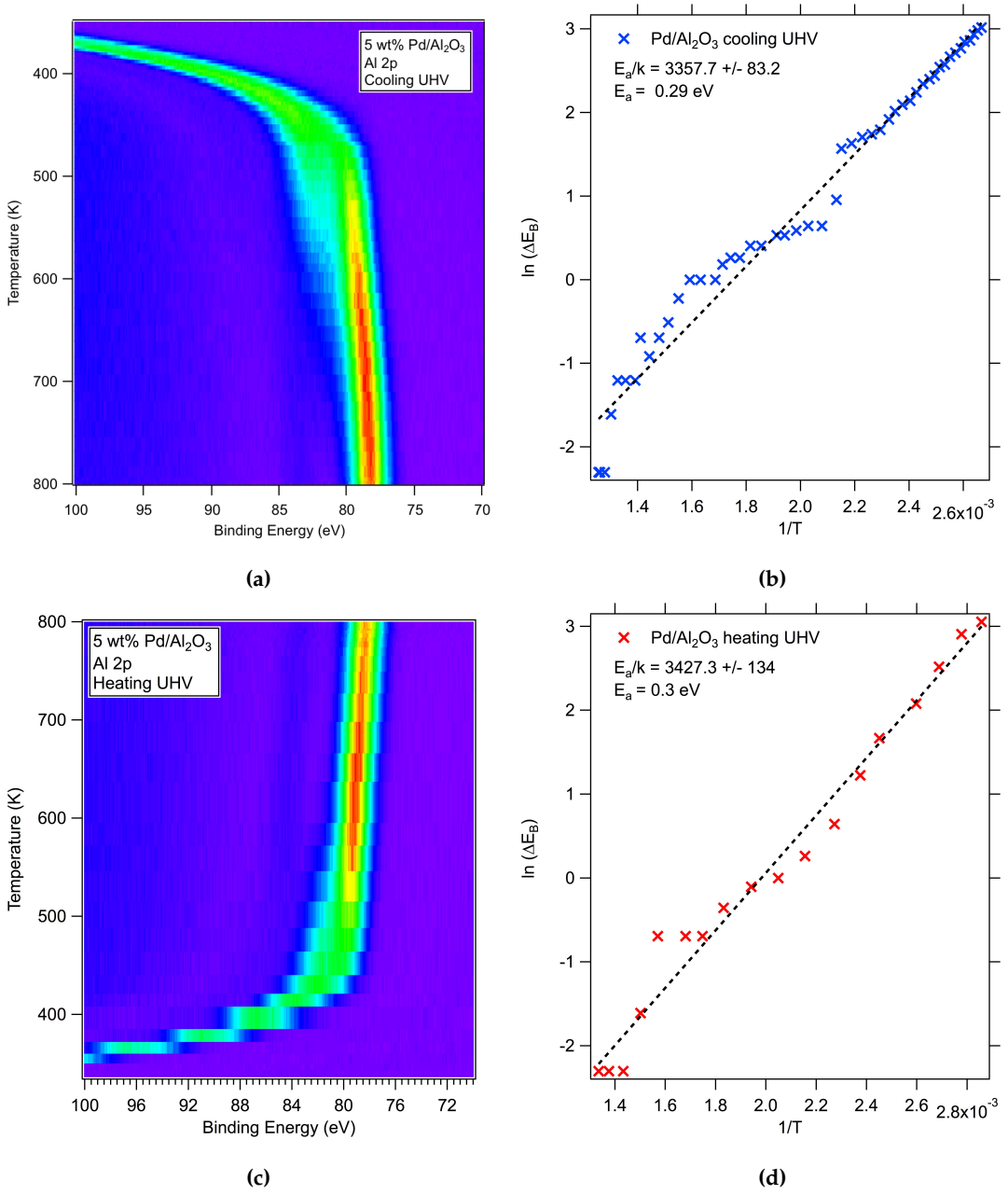

Figure 3.3: Temperature-programmed XPS spectra of a 5 wt% Pd/Al_2O_3 catalyst spray coated on a n-type P-doped Si wafer taken in the Al 2p region whilst heating from 300 K to 800 K (a) and cooling from 800 K to 300 K (c). Figures (b) and (d) show the determination of the activation energies using the binding energy shift at each point on the TP-XPS spectra. k (Boltzmann constant) = 8.62×10^{-5} eV K^{-1}

Under ambient pressures, a similar effect is observed. Figure 3.4 shows TP-XPS in the Al 2p region of a different Pd/Al_2O_3 catalyst cooled from 800 K in 0.33 mbar O_2 (Fig. 3.4a) and the derivation of the activation energy (Fig. 3.4b). As the activation energy is slightly lower at 0.25 eV (5.5% error), the presence of the gas appears to have a slight conducting effect over UHV. The gas phase molecules can also be irradiated by the photon beam, producing photoelectrons that can partially help to neutralise the surface, in a similar way to a flood gun. The effect of pressure on conductivity has been observed on a mica sample by Bluhm, whereby the binding energy in the Si 2p region is shifted 250 eV with an increase in water vapour pressure from 0.1 – 1.7 Torr [74]. Temperature, however, is still the main influence on conductivity of these samples, as the activation energy does not decrease significantly under ambient pressures. These activation energies are considerably lower than the band for for pure alumina, which is reported to be 8.0 – 8.7 eV [152, 153].

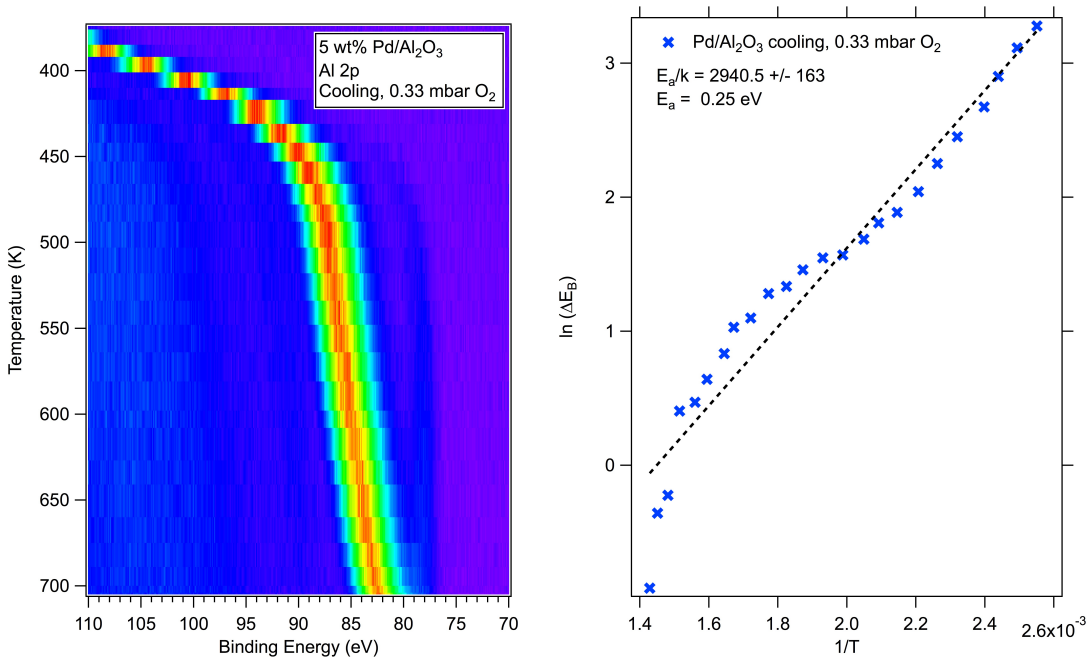

Figure 3.4: Temperature-programmed XPS spectra of a 5 wt% Pd/Al_2O_3 catalyst spray coated on a n-type P-doped Si wafer taken in the Al 2p region whilst cooling from 800 K to 400 K under 0.33 mbar O_2 pressure (a) and determination of the activation energy using the binding energy shift at each point on the TP-XPS spectra (b). k (Boltzmann constant) = 8.62×10^{-5} eV K^{-1}

The same temperature effect on conductivity is seen on silica-supported catalysts. Figure 3.5a shows temperature-programmed XPS spectra of a Pd/SiO_2 catalyst under UHV and a temperature ramp from 300 – 800 K. The stable peak at 99 eV is characteristic of elemental silicon, likely coming from the Si wafer substrate. The strong intensity suggests there will be a large conductivity contribution from the substrate and the effect is reflected in the activation energy (Figure 3.5b). E_a for this Pd/SiO_2 catalyst is 0.09 eV (2% error); 0.21 eV lower than that for Pd/Al_2O_3 under the same conditions. High temperature studies on Y_2O_3 have shown that at 650 – 900 K the conduction of oxygen ions has an activation energy of 0.85 eV, compared to a band gap of 5.5 eV [154, 155]. From the data presented here, it is not possible to tell if the increase in conductivity with temperature is caused by a dopant or by ion conductivity. However, similar effects and activation energies are seen with Y_2O_3 and assigned to ion conductivity. It is likely ion conductivity is the reason for the extra conductivity with increased temperatures, rather than an electronic effect.

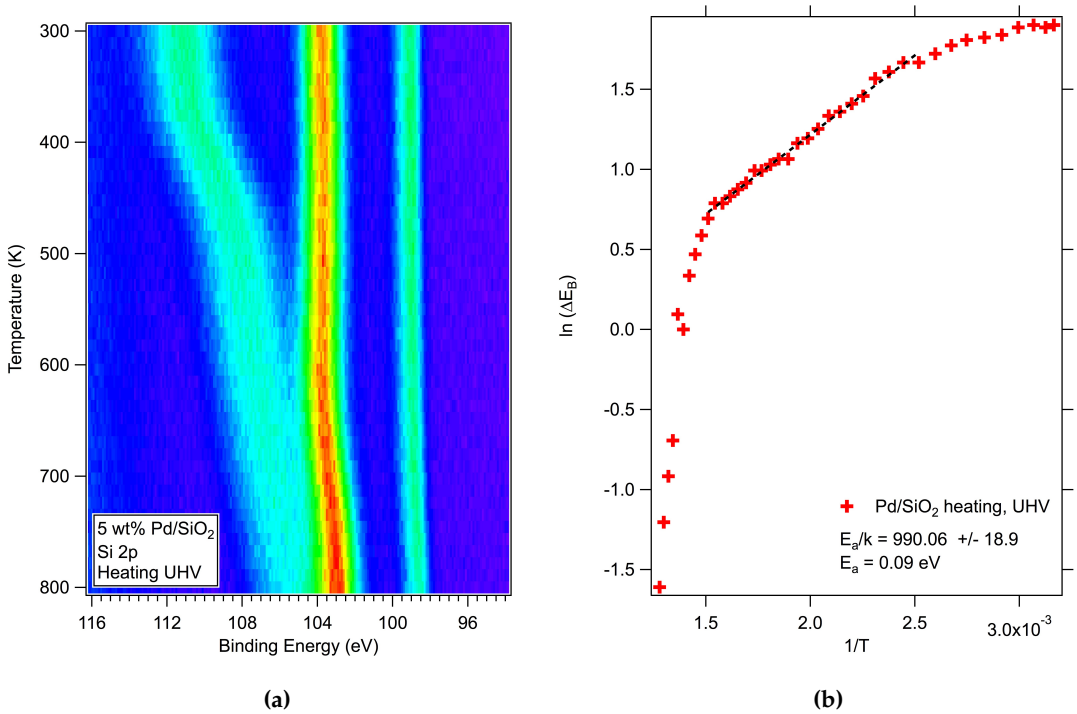

Figure 3.5: Temperature-programmed XPS spectra of a 5 wt% Pd/SiO_2 catalyst spray coated on a n-type P-doped Si wafer taken in the Si 2p region whilst heating from 300 K to 800 K in UHV (a) and determination of the activation energy using the binding energy shift at each point on the TP-XPS spectra (b). k (Boltzmann constant) = 8.62×10^{-5} eV K^{-1}

The data presented in this section show that different insulating supports under both ultra-high vacuum and ambient pressures behave similarly in terms of conductivity. At room temperature the spectra shift in binding energy due to charging of the surface, but this effect can easily be minimised by using a conducting substrate and increasing the temperature to $\sim$ 450 K. It is for this reason that the NAP-XPS experiments in Chapters 4, 5 and 6 begin at 500 K. This temperature is high enough for the binding energy shift to be stabilised, but not too high for the methane oxidation reaction to take place. Artefacts of sample charging are still seen however, and the spectra must be fitted accounting for these spectral distortions.

3.2 Peak Fitting

This section standardises a fitting procedure for supported metal catalysts of which the support is an insulating material, e.g. Al_2O_3 or SiO_2. The insulating properties of these supports can induce shifting, broadening [142] and splitting [156] of the XPS line shape due to charging caused by a positive charge build up on the surface. In metals or other conductors, the valence band and the conduction band overlap. Therefore, electrons are free to move easily between the valence and conduction bands. In this instance, the XPS should not be affected by charging and conventional XPS fitting procedures can be implemented. XPS peaks of conducting samples are fitted using the pseudo-Voigt function that takes into consideration both Lorentzian line shapes as a result of core hole life times, and Gaussian line shapes from instrumental effects [101]. The pseudo-Voigt function is shown below in Equation 3.5:

$$I(BE) = H\left\{m \cdot \frac{\tau^2}{2(BE-P)^2+\tau^2} + (1-m) \cdot \exp\left[-\left(\frac{BE-P}{0.601\,\tau}\right)^2\right]\right\} \tag{3.5}$$

where P = position of the peak (binding energy, eV), E = energy (independent variable, eV), m = Gaussian and Lorentzian mixing parameters, τ = the full width of half maximum (FWHM, eV) of the fitted peak and H = height of the peak (normalised y axis value, arbitrary units). In conducting samples, these parameters can be taken from the spectrum directly and may differ within the spectrum depending on the species. However, in insulating samples such as Pd/Al_2O_3 and Pd/SiO_2 catalysts, the FWHM (τ), mixing parameter (m) and x-axis energy shift (ΔE) values are obtained from fitting the peak of the insulating material (Al 2p in a Pd/Al_2O_3 catalyst), as the assumption is made that the main contribution to peak broadening is sample charging. The same τ, m and ΔE values from this spectrum are then used to fit the corresponding metal spectrum (Pd 3d in a Pd/Al_2O_3 catalyst) that has been taken under the same conditions and with the same photon energy. The τ and m parameters take into account any peak broadening or asymmetry caused by charging. ΔE, the difference between the binding energy values of the experimental peak and the literature peak, accounts for any peak shifting caused by charging. On some occasions the peak of the insulating material appears to be split into two, which is a consequence of differential charging on different areas of the sample surface [117, 157]. Despite not making chemical sense, the peak is fitted with two features, and any corresponding spectra must also be fitted with two features for every peak.

3.2.1 Peak Fitting Example: One Al 2p Peak

An example is shown using a Pd/Al_2O_3 catalyst, but the same approach can be applied to any supported-metal catalyst. After normalisation and background subtraction, the Al 2p peak can be fitted. Figure 3.6 shows a fitted Al 2p spectrum of a Pd/Al_2O_3 catalyst under partial methane oxidation conditions. The same parameters (τ = 2.9 and m = 0.1) were used to fit the Pd 3d spectrum that was taken at the same incident photon energy and under the same reaction conditions (Figure 3.7). The Pd 3d spectrum in is shifted along the x-axis by ΔE (–4.4 eV) in order to correct the binding energy. The energy separation and the intensity ratios between the spin-orbit components Pd $3d_{5/2}$ (low binding energy, 335 – 337 eV) and Pd $3d_{3/2}$ (high binding energy, 340 – 342 eV) are always kept fixed at 5 eV ($\pm$ 0.3 eV) and 1.5 ($\pm$ 0.2) respectively [158, 159] and are not dependent on the Al 2p spectrum. Due to the constraints of the parameters from the Al 2p spectrum and the spin-orbit coupling properties, the fit residuals for Pd 3d spectra are calculated to be typically 1 – 5% [160].

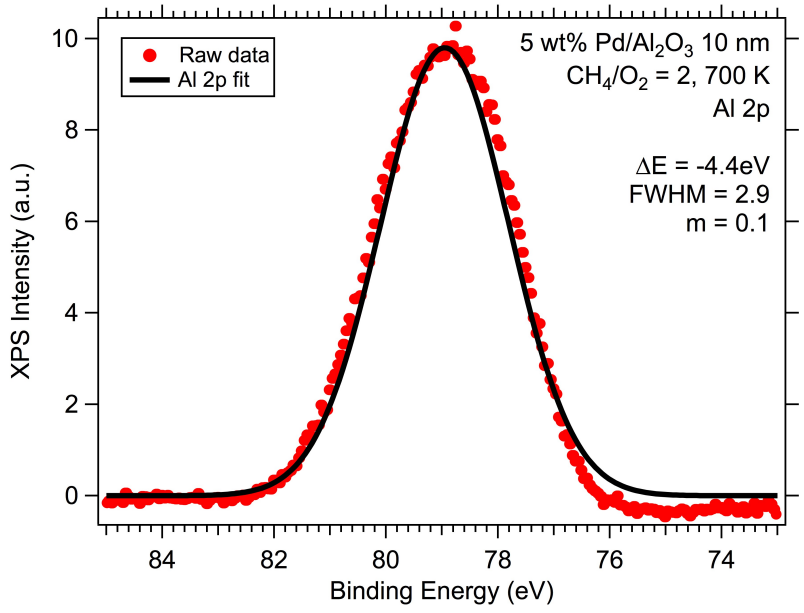

Figure 3.6: Al 2p NAP-XP spectrum of Pd/Al_2O_3 catalyst (10 nm) under partial methane oxidation pressures (700 K, 0.33 mbar $CH_4 + O_2$). The dotted line shows the raw data and the solid line is the fit. $h\nu$ = 450 eV. Fitting parameters: τ = 2.9, m = 0.1

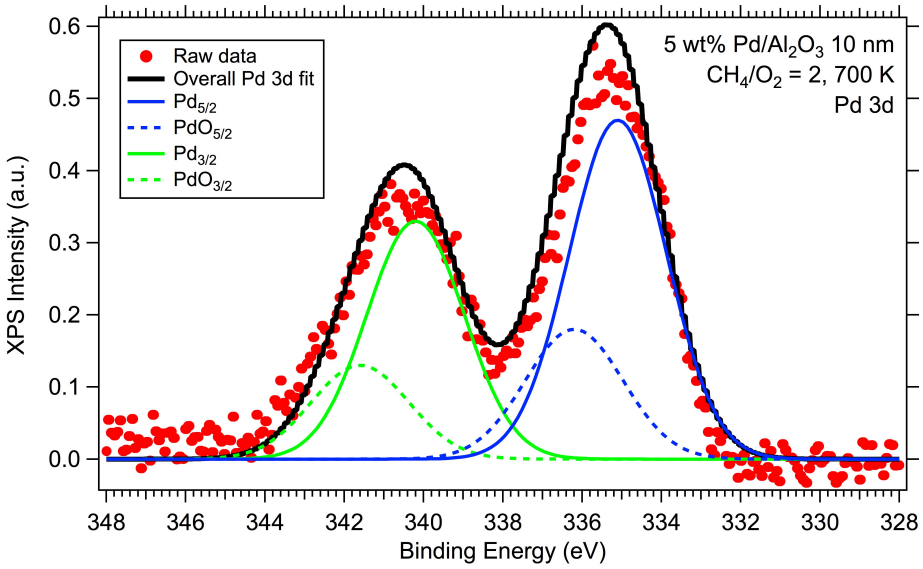

Figure 3.7: Pd 3d NAP-XP spectrum of Pd/Al_2O_3 catalyst (10 nm) taken under the same temperature (700 K) and pressure (0.33 mbar CH_4 + O_2) and with the same photon energy (450 eV) as the Al 2p spectrum shown in Figure 3.6. Dotted line is the raw data, solid lines are the fits. Fitting parameters: τ = 2.9, m = 0.1

3.2.2 Peak Fitting Example: Two Al 2p Peaks

As well as binding energy shifting and peak broadening, another typical artefact of sample charging is peak splitting due to different levels of charging in different regions of the surface [117,157,161]. Figure 3.8 shows an Al 2p spectrum of the same Pd/Al_2O_3 catalyst shown in Figures 3.6 and 3.7 at 550 K. Due to the temperature effect as previously described in Section 3.1, the catalyst exhibits more charging at lower temperatures as seen by the peak splitting at 550 K that is not seen at 700 K in Figure 3.6. The corresponding Pd 3d spectrum in Figure 3.9, recorded under the same conditions and with the same photon energy, does not look typical of a Pd 3d line shape and is likely to also be affected by charging in the same way. To account for this, the Al 2p spectrum must be fitted with two features, as in Figure 3.8. The binding energy shifts (ΔE) from the literature value of 74.5 eV are: –7.2 eV for Peak 1; and –3.9 eV for Peak 2. These are the values used to correct the binding energy scale of the corresponding Pd 3d peaks in Figure 3.9.

In this example, τ_{Al2p} = 2.8 eV and m_{Al2p} = 0.1. These values are included in the fit function of the Pd 3d spectrum shown in Figure 3.9, as well as the values of ΔE. The difference in the case of two Al 2p peaks is that each Pd $3d_{5/2}$ and Pd $3d_{3/2}$ feature must also be split into two; one shifted by ΔE

of Al 2p$_{Peak1}$ (–7.2 eV) and the other shifted by ΔE of Al 2p$_{Peak2}$ (–3.9 eV). The energy separation and the intensity ratios between the spin-orbit components (Pd 3d$_{5/2}$ and Pd 3d$_{3/2}$) are again kept constant at 5 eV ($\pm$ 0.3 eV) and 1.5 ($\pm$ 0.2) respectively. However, such as this case where the individual Pd 3d$_{5/2}$ and Pd 3d$_{3/2}$ peaks are split into two, the intensity ratio of the two split Al 2p peaks (1.08) is used to estimate the height ratio of these (see corresponding green and blue lines in Figure 3.9).

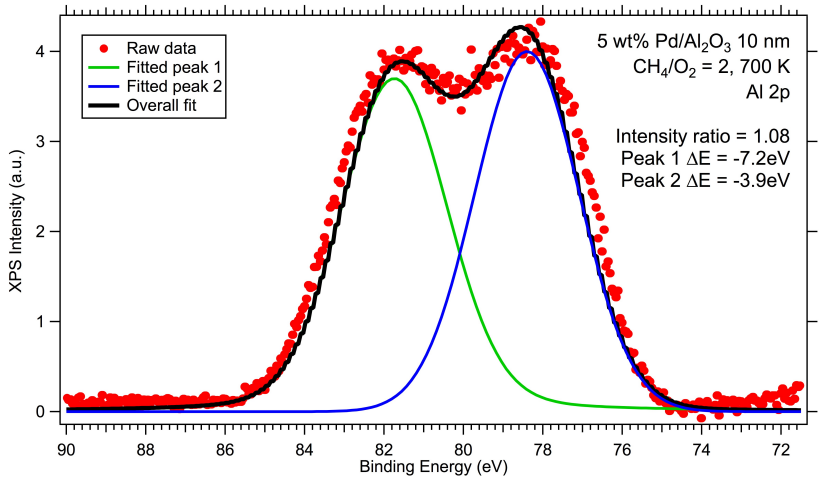

Figure 3.8: Al 2p NAP-XP spectrum of Pd/Al_2O_3 catalyst (10 nm) under partial methane oxidation pressures (550 K, 0.33 mbar $CH_4 + O_2$). The dotted line shows the raw data and the solid line is the fit. $h\nu$ = 450eV. Fitting parameters: τ = 2.9, m = 0.1

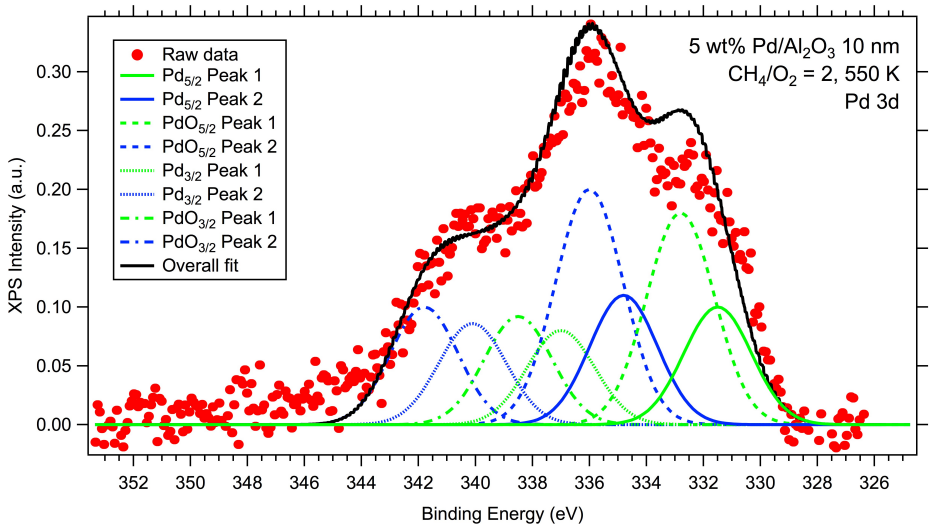

Figure 3.9: Pd 3d NAP-XP spectrum of Pd/Al_2O_3 catalyst (10 nm) taken under the same temperature (550 K) and pressure (0.33 mbar $CH_4 + O_2$) and with the same photon energy (450 eV) as the Al 2p spectrum shown in Figure 3.8. Dotted line is the raw data, solid lines are the fits. Fitting parameters: τ = 2.8, m = 0.1

The splitting of Pd 3d peaks for both PdO_x and PdO species and Pd $3d_{5/2}$ and Pd $3d_{3/2}$ spin-orbit components means there are eight fitted peaks in total. The sum of these should add up to the original spectrum, and in this example the residual fit is 1%. Due to the considerations taken from the Al 2p spectrum, the fits for the Pd 3d spectrum are highly constrained. The FWHM, asymmetry, and peak separation parameters are taken from the corresponding Al 2p spectrum and kept fixed when fitting the Pd 3d spectrum. This only leaves peak position and height parameters free, but peak heights are kept at a 1:2 ratio in accordance with the $3/2$ and $5/2$ spin-orbit coupling.

The NAP-XPS data presented in Chapters 4, 5 and 6 are fitted using this method. The FWHM (τ) is kept constant for each spectrum, rather than species, as the value used is obtained from the Al 2p spectrum. Despite the likelihood of differential charging occurring across the surface of the sample, it is assumed that the level of charging is uniform across the spot size of the beam and no correction factors are applied.

4 Methane Oxidation: NAP-XPS and Pd/Al_2O_3 catalyst

The material in this Chapter has been published as: R. Price, T. Eralp-Erden, E. Crumlin, S. Rani, S. Garcia, R. Smith, L. Deacon, C. Euaruksakul and G. Held, *The Partial Oxidation of Methane Over Pd/Al_2O_3 Nanoparticles Studied In-Situ by NAP-XPS*, Topics in Catalysis, 59:516-525 (2016)

Abstract

Near ambient-pressure X-ray photoelectron spectroscopy (NAP-XPS) is used to study the chemical state of methane oxidation catalysts in-situ. Al_2O_3–supported Pd catalysts are prepared with different particle sizes ranging from 4 nm to 10 nm. These catalysts were exposed to conditions similar to those used in the partial oxidation of methane (POM) to syngas and simultaneously monitored by NAP-XPS and mass spectrometry.

NAP-XPS data show changes in the oxidation state of the palladium as the temperature increases, from metallic Pd^0 to PdO, and back to Pd^0. Mass spectrometry shows an increase in CO production whilst the Pd is in the oxide phase, and the metal is reduced back under presence of newly formed H_2.

A particle size effect is observed, such that CH_4 conversion starts at lower temperatures with larger sized particles from 6 nm to 10 nm. We find that all nanoparticles begin CH_4 conversion at lower temperatures than polycrystalline Pd foil.

4.1 Introduction

Instead of flaring off large quantities of unused natural gas around the world, it could be used in a more environmentally friendly way as fuel for automotive engines. Natural gas vehicles (NGVs) operate under lean conditions with low methane concentrations (500-1000 ppm) and working temperatures typically under 823 K (550°C). The beneficial outcome of these working conditions is that relatively "clean" products are produced (CO_2, H_2, H_2O) in comparison to other fossil fuels producing harmful nitrogen and sulphur containing compounds. In NGVs, NO_x and SO_x exhaust emissions are greatly reduced [162–164]. The challenge lies with the storage and transport of gases, and the conversion into a more useful, transportable product. The C-H bonds in aliphatic hydrocarbons have high dissociation energies (439.3 kJ mol^{-1} in CH_4) and the absence of functional groups leaves the molecule with zero polarity and no sites for either nucleophilic or electrophilic attack. This makes small hydrocarbons, such as methane, very difficult to oxidise without a catalyst at low temperatures [34].

The partial oxidation of methane (POM) uses an oxygen-deficient mixture to produce carbon monoxide and hydrogen:

$$CH_4 + \tfrac{1}{2}O_2 \longrightarrow CO + 2\,H_2$$

This CO/H_2 mixture (commonly known as "syngas") is a useful precursor for methanol synthesis. Methanol is a versatile, clean-burning liquid that is used in many applications, including in the production of animal feed, hydrogen storage and as a precursor for the octane-enhancing additive methyl-tertiary-butyl ether (MTBA) [165]. Moreover, methanol in itself has the potential to become a large-scale renewable alternative to fossil fuels [166]. It is produced by the hydrogenation of CO at 773 – 923 K commercially using a $Cu/ZnO/Al_2O_3$ catalyst [51]:

$$CO + 2\,H_2 \longrightarrow CH_3OH$$

Syngas is not currently produced on a large scale by partial methane oxidation, but instead by steam-reforming, where methane reacts with water, over a nickel-based catalyst, at high temperatures (>1000 K) and pressures [167]:

$$CH_4 + H_2O \longrightarrow CO + 3\,H_2$$

Although this is a high-yielding reaction, the conditions at which it operates are expensive and unsustainable in the long term. Therefore it is of great importance to find a viable catalyst to enable large-scale

POM for syngas production at lower temperatures and atmospheric pressures. POM reaction conditions are generally leaner and more cost effective than those of steam reforming. It has previously been reported that the syngas yield and selectivity is optimised with temperatures above 650 K [168, 169] (a 90% yield is observed at 1050 K with a variety of transition metal-based catalysts [84]). For both methane oxidation and steam-reforming, a catalyst is yet to be developed that can activate this reaction at sustainable and more cost effective, lower temperatures and pressures.

Platinum group metals are widely used as the basis for catalysts for a number of different applications [170]. In particular, Pd and Pt are used for methane activation reactions, in the form of supported nanoparticles. The mechanism by which they operate is still relatively unknown. It has been established that a change in oxidation state of the metal occurs, but in the case of palladium-based catalysts, it is unclear as to which state is the active species. Burch and co-workers reported that for a Pd catalyst the fully oxidized surface is the optimum state [171], but more recently Yang et al. discovered that a mixed phase of PdO and PdO_x (where $0 < x \leq 1$) is the most active state for methane combustion [39]. For the Pd(111) surface, it has been reported that a 2D surface oxide, Pd_5O_4, forms after exposure to oxygen at high temperatures [172].

X-ray photoelectron spectroscopy (XPS) is a useful, surface sensitive technique for identifying the surface chemical state and composition of solids. In order to avoid unintentionally measuring contaminants rather than the species of interest, these experiments are generally performed in an ultra-high vacuum (UHV). However, in catalysis, UHV is not a representative condition and a catalyst under UHV conditions may behave differently compared to reaction conditions. Near ambient-pressure (NAP-) XPS helps to bridge this gap, with pressures up to 100 Torr (130 mbar) now possible [173]. The differential pumping of NAP-XPS systems gradually reduces the pressure in the analysis chamber down to UHV at the analyser [134], and so it is possible to collect information about the chemical state of the surface of the catalyst in-situ, under specific close-to-real-world reaction conditions.

4.2 Experimental

4.2.1 Sample Preparation

Several samples of 5 wt% γ-Al_2O_3 supported Pd nanoparticles were prepared by a colloidal co-precipitation method [87], using a $Pd(NO_3)_2$ precursor (8.34% assay, Alfa-Aesar). A solution of dodecenyl succinic anhydride (DSA) in THF was added to a base solution of aqueous Na_2CO_3. Aqueous palladium nitrate was added to the flask dropwise in molar excess and γ-Al_2O_3 was added as the support material. The resulting slurry was filtered under suction, prior to drying in the oven for 2 hours at 380 K and calcination treatment. The catalyst was crushed and calcined for 2 h in air at a range of temperatures between 300° C to 700° C (573 – 973 K) in order to achieve a range of particle sizes (see Table 4.1).

Catalyst	Calcination (K)	Mean d_{TEM} (nm)	σ (nm)	MSA (m^2/g)	MD (%)
A (4nm)	573 (300°C)	4.06	1.23	0.29	1.30
B (5nm)	773 (500°C)	4.91	1.54	0.15	0.69
C (6nm)	873 (600°C)	6.16	1.56	0.13	0.57
D (7nm)	973 (700°C)	7.12	1.86	0.18	0.80
E (10nm)	873 (600°C)*	9.63	1.98	-	-
F	1273 (1000°C)	186	74	0.07	0.31

Table 4.1: List of samples prepared. The mean diameter (and σ, standard deviation) of Pd/Al_2O_3 nanoparticles calcined to different temperatures as determined by TEM, metal surface area (MSA) and % metal dispersion (MD) as determined from CO chemisorption. (* Batch prepared in a previous study; used here to complete the particle size range.)

Catalysts A (4 nm), B (5 nm), C (6 nm), D (7 nm) and E (10 nm) were chosen as the samples used for these experiments, to give a representative size range. 1 g of Pd/Al_2O_3 nanoparticles and 0.1 g of P3 (to improve adhesion) was added to 3 g H_2O. A P-doped silicon wafer (1 cm^2) was fixed to a hot plate and the nanoparticles were deposited onto the wafer using a spray gun. Each spray lasted for five seconds and the silicon wafers were weighed before and after so the number of Pd atoms and surface area of Pd can be calculated (Table 4.2). The number of Pd nanoparticles deposited on the silicon wafer is calculated using Equation 4.1 and, assuming only half of each nanoparticle is available for catalysis, the Pd surface area is calculated by Equation 4.2:

$$number\ of\ NPs = \frac{amount\ of\ catalyst\ on\ Si\ wafer\ (kg) \times metal\ loading\ (\%)}{\frac{1}{2} \cdot \left(\left(\frac{4\pi}{3} \right) \left(\frac{d}{2} \right)^3 \rho \right)} \tag{4.1}$$

$$area\ of\ one\ NP = \frac{\pi d^2}{2} \tag{4.2}$$

where d is the particle diameter and ρ is the the density of Pd (11.9×10^3 kg m^{-3}). A dry, homogeneous layer of Pd/Al_2O_3 nanoparticles remains on the surface of the silicon wafer, with an available surface area 100 – 500 $\times$ greater than a single crystal.

d (nm)	N_{NP}	A_{NP} (m^2)	Pd surface area (m^2)	Pd surface area (cm^2)
4.1	1.14×10^{15}	2.64×10^{-17}	3.01×10^{-2}	301.3
5.0	3.47×10^{14}	3.93×10^{-17}	1.36×10^{-2}	136.1
6.2	8.55×10^{14}	6.04×10^{-17}	5.16×10^{-2}	516.4
7.1	5.34×10^{14}	7.92×10^{-17}	4.23×10^{-2}	422.5
9.6	9.43×10^{13}	1.45×10^{-16}	1.37×10^{-2}	136.6

Table 4.2: Surface areas of 5 wt% Pd/Al_2O_3 catalysts spray coated on silicon wafer. N_{NP} = number of Pd nanoparticles, A_{NP} = area of one Pd nanoparticle

4.2.2 Sample Characterisation

Laboratory-based XPS was used to determine the elemental composition of the catalysts. The Pd/Al_2O_3 nanoparticles were mounted onto adhesive carbon tape and inserted into a Thermo Escalab 250 photoelectron spectrometer, which is equipped with a monochromatised Al K-α source ($h\nu$ = 1486.6 eV) with a large spot to maximise count rate, a flood gun, and an electromagnetic lens. The nanoparticles were probed to identify surface elemental composition at room temperature and ultra-high vacuum (base pressure 10^{-8} mbar). Overview spectra determined the levels of contamination and high-resolution spectra obtained in the Pd 3d, O 1s, Al 2p and regions confirmed the relative presence and oxidation state of each element. Spectra taken in the Pd 3d region suggest the nanoparticles are in their oxidised state, with Pd $3d_{5/2}$ peaks at 336 eV representative of a PdO species. This is to be expected as alumina has Lewis acid sites on the surface, rendering the metal electron-deficient and increasing the oxidation

state [174]. The electron-deficient Pd^{2+} species is then free to bond with oxygen atoms from the air, resulting in PdO.

Transmission electron microscopy (TEM) was used to determine the mean particle size of each synthesised sample (Figure 4.1). The samples were each ground between two glass slides and dusted onto a holey carbon coated copper grid prior to examination in a Tecnai F20 transmission electron microscope. The samples were analysed using 200 kV and 30 μm C2 aperture at a variety of magnifications ranging from 5 nm to 100 nm. Approximately 100 nanoparticles in each sample were measured at different magnifications and in different areas to gain a representative mean particle size. The metal surface area and % metal dispersion were measured using a Micromeritics AutoChem II 2920 analyser. Pulses of CO were passed through 0.1 g of catalyst sample at 308K and the adsorbed CO was determined by a thermal conductivity detector. A reduction step prior to the CO pulses ensured that all the palladium had been reduced to a metallic state. The surface area of palladium in each catalyst is given by:

$$\text{Area of Pd} = \frac{\text{molecules of CO adsorbed}}{\text{molecules per m}^2}$$

The percentage metal dispersion is calculated using:

$$\text{MD(\%)} = \frac{N_S}{N_T} \times 100$$

where N_S is the number of atoms on the surface and N_T is the total number of atoms in the sample. The results are shown in Table 4.1.

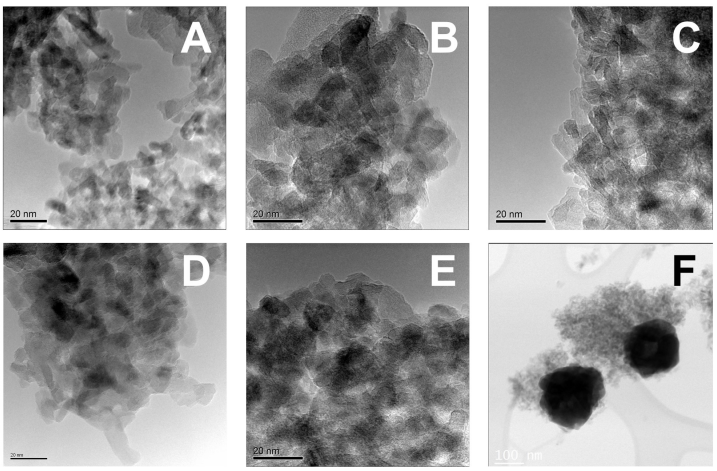

Figure 4.1: TEM images of Pd/Al_2O_3 catalysts calcined to different temperatures. A = 573 K, B = 773 K, C = 873 K, D = 973 K, E = 873 K (from a different batch), F = 1273 K.

The reactivity of Pd/Al_2O_3 catalysts A (4 nm), B (5 nm), D (7 nm) and E (10 nm) was tested using a batch flow reactor. Each catalyst was pressed into a pellet, crushed and sieved at 250-355 μm. 0.4 g of each catalyst was exposed to 1000 ppm of CH_4/N_2 and various concentrations of O_2 (1%, 5%, 12%) in N_2 as the temperature was ramped from 400 – 800 K (ramp rate 10 K/min). The products were measured by FT-IR, and the y-axis in Figure 4.2 (% CH_4 conversion) is calculated based on the amount of CH_4 converted to CO_2 and H_2O as a function of temperature. The data show that there is very little difference between the light-off temperatures when different sized nanoparticles and $[CH_4] : [O_2]$ ratios are used in these concentrations, with the exception of 10 nm nanoparticles which begin methane conversion at almost 100 K lower. Catalyst E is the only catalyst to reach 100% conversion before 800 K, suggesting they are the most active nanoparticles under these conditions.

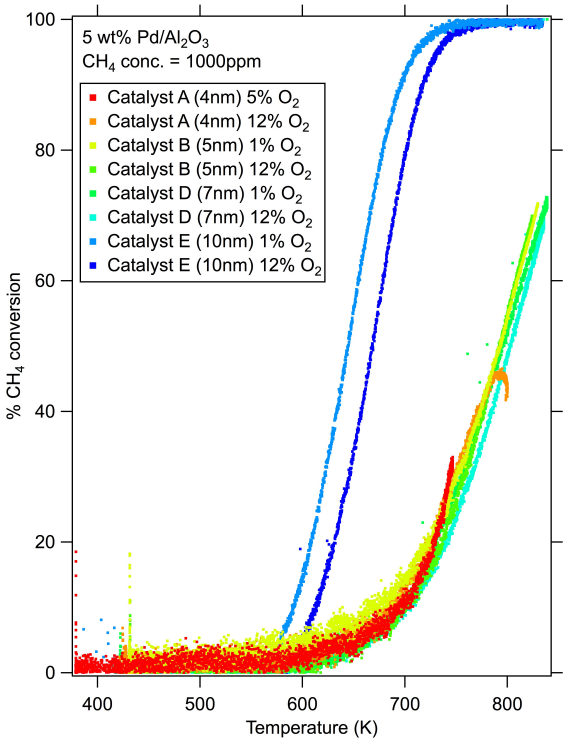

Figure 4.2: Synthetic Catalyst Activity Test (SCAT) data of 5 wt% Pd/Al_2O_3 catalysts under 1000 ppm methane and various oxygen concentrations.

4.2.3 Synchrotron Experiments

Near ambient-pressure X-ray photoelectron spectroscopy studies were carried out at beam line 9.3.2 of the Advanced Light Source (ALS), National Lawrence Berkeley Laboratory, USA [132]. The endstation is equipped with a Scienta 4000 HiPP analyser with a custom designed differential pumping system that allows pressures of up to 1 Torr in the analysis chamber, enabling in-situ data collection. A mass spectrometer is placed in the first differential pumping stage, which was used to quantify the gas composition during the reaction. The samples were individually mounted onto a UHV compatible sample holder connected to thermocouple wires for controlled heating.

Each sample was fully characterised by XPS in UHV at 450 K, a temperature at which the sample is much less affected by charging than at room temperature (see Figure 3.3 of Chapter 3), before being exposed to a 240 mTorr gaseous mixture of oxygen and methane. Partial methane oxidation ($[CH_4] : [O_2] = 2$) was studied for various Pd particle sizes, and a variety of gas compositions (oxygen to methane ratios of 5:1, 2:1, 1:1 and 1:2) were tested using one particle size (4 nm). The temperature of the sample was increased in steps of 50 K or 100 K between 400 – 700 K. In-situ high-resolution XPS measurements were taken at constant temperature during this temperature ramp. Pd 3d, Al 2p and C 1s spectra were obtained using the same incident photon energy of $h\nu$ = 450 eV, with the binding energies being calibrated to the literature value for Al 2p (74.5 eV). QMS data were collected throughout the XPS measurements.

The NAP-XP spectra obtained were normalised and a Shirley background [175] was subtracted. The difference in binding energy between the literature value of the Al 2p peak (74.5 eV [149]) and the experimental value was determined and applied to correct the binding energy scale of the corresponding Pd 3d and C 1s spectra. This is based on the assumption that, both Pd and C, sitting on the Al_2O_3 support are affected by the same charging shifts. Although not proving to be a problem for data collection, the lack of sample conductivity occasionally broadens the Al 2p peak. The extent to which these peaks broaden is taken into account when fitting the corresponding Pd 3d peaks. In some cases, where sample charging was inhomogeneous, the Al 2p peak is split into two. Each Pd 3d peak (both $\frac{5}{2}$ and $\frac{3}{2}$ spins-orbit peaks of metallic Pd and Pd oxides) is therefore also split into two totalling eight fitted peaks in one spectrum, which is evident in Figures 4.3 and 4.7. In these cases the BE correction was applied to the higher BE peaks of each doublet, therefore the peaks around 332 eV are charging-induced "satellites". The intensity ratio of the two Al 2p peaks is used to split the Pd 3d peaks of each species. The Pd 3d

peaks were fitted using fit functions which were customized for each spectrum on the basis of the parameters from the corresponding Al 2p fit, notably peak broadening and splitting. The fit function was designed around the pseudo Voigt function:

$$I(BE) = H\left\{m \cdot \frac{\tau^2}{2(BE-P)^2+\tau^2} + (1-m) \cdot \exp\left[-\left(\frac{BE-P}{0.601\,\tau}\right)^2\right]\right\}$$

where BE is the binding energy, P the peak position, H is the peak height, τ the FWHM, and m is the Gaussian-Lorentzian mixing parameter (usually constant at 0.1). The FWHM and mixing parameters are dependent on the corresponding Al 2p spectrum and vary from spectrum to spectrum. The separation between the spin-orbit components Pd $3d_{5/2}$ (low binding energy, 335 – 337 eV) and Pd $3d_{3/2}$ (high binding energy, 340 – 342 eV) is always kept fixed at 5 eV ($\pm$ 0.3 eV). The relative peak height ratios, calculated using a fixed FWHM, are fixed at 1.5 ($\pm$ 0.2) [158,159]. More information on the fitting procedure, including examples, can be found in Chapter 3.

Mass spectrometry data were recorded in-situ in order to help quantify methane to syngas conversion at different constant temperatures (during the XPS data acquisition) and while cooling down from $>$ 700 K in a 0.33 mbar (240 mTorr) mixture of CH_4 and O_2 ([CH_4] : [O_2] = 2). Methane conversion was calculated as the percentage of the partial pressures of each gas observed with respect to the partial pressure of methane at 350 K where no reaction is observed. For example, the conversion to CO is:

$$\text{Conv(CO)}_T = \frac{\text{partial pressure of CO at } T}{\text{partial pressure of CH}_4 \text{ at 350 K}} \times 100\ \%$$

No correction factors were used to calculate the conversion of each gas.

4.3 Results

4.3.1 Particle Size Effect: Partial Oxidation of Methane

Particle size effects are observed in the near ambient-pressure XP spectra and mass spectrometry data. NAP-XPS in the Pd 3d region is most useful to monitor the chemical state of the metal and therefore the nature of the catalytically active oxide. Figures 4.3 – 4.7 show the in-situ data for Catalysts A-E respectively: near ambient-pressure XPS in the Pd 3d region, and the corresponding reactant to product conversion as calculated from mass spectrometry data. High resolution in-situ XPS was taken at 50 K intervals between 500 K and 700 K, under 0.33 mbar (240 mTorr) of CH_4 + O_2 ([CH_4] : [O_2] = 2).

The peaks at lower binding energies (335.0 $\pm$ 0.2 eV) are characteristic of metallic Pd (Pd^0) with PdO_x species appearing slightly higher at 336 – 337 eV. Due to the catalyst preparation method and storage (i.e. exposure to air), Pd shows some degree of oxidation for all samples at 500 K, but metallic Pd peaks at 335.0 $\pm$ 0.2 eV are dominant at these lower temperatures. As the temperature is increased to 600 K and again to 650 K, an XPS signal characteristic of a PdO_x species at 336.0 – 336.2 eV becomes dominant for most particle sizes. The CH_4 conversion plots associated with the NAP-XPS measurements in Figures 4.3 – 4.7, calculated from mass spectrometry data, indicate an increase in syngas production around these temperatures. Our activity studies have shown that under similar conditions CH_4 begins conversion to POM products between 550 K and 600 K (see Figure 4.2. In addition, metallic Pd (335.0 $\pm$ 0.2 eV) also has a strong contribution in the XP spectra, and the data show that a mixture of both Pd metal and Pd oxide is needed to continue the reaction, after the oxide has initially been formed. At temperatures above 700 K the oxide species is reduced to metallic Pd and the product formation of CO and H_2 slows down. The NAP-XPS data in Figures 4.3 – 4.7 also show that at 700 K the oxide species is almost fully reduced to metallic Pd. This is reflected in the CH_4 conversion plots which indicate a slowing down of CO and H_2 formation. It could be argued that for Catalyst E (10 nm, Figure 4.7) the reaction rate does not slow at 700 K and this could be because a larger ratio of metallic Pd to oxide Pd is present than for other catalysts (see Table 4.3), further supporting the hypothesis that metallic Pd is key for continuing the reaction.

The CH_4 conversion plots in the lower panels of Figures 4.3 – 4.7 show that complete oxidation of methane to CO_2 and H_2O occurs at low temperatures. The selectivity of these catalysts changes towards partial oxidation to syngas at temperatures above 570 K. There is also a distinct difference between cat-

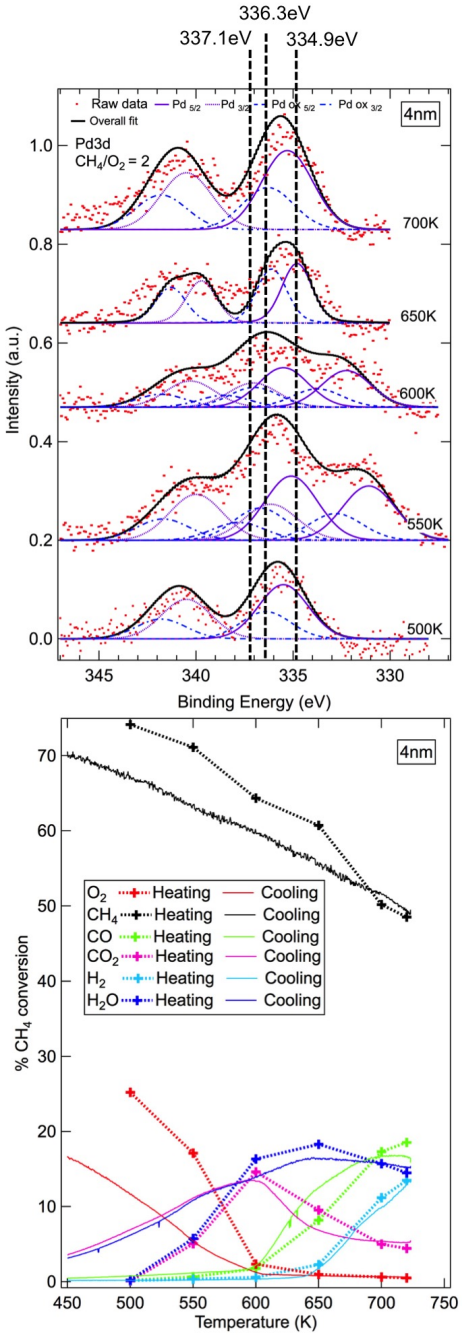

Figure 4.3: Catalyst A (Pd/Al_2O_3 nanoparticles of average size 4 nm). NAP-XP spectra in the Pd 3d region (top) and CH_4 conversion, calculated from mass spectroscopy data (bottom), recorded in the temperature range from 450 K to 720 K under 240 mTorr O_2:CH_4 pressure (1:2). "Heating": mass spectrometry at constant temperature during NAP-XPS measurements; "Cooling": recorded during continuous cooling from 720 K to 450 K. Binding energies are corrected to corresponding Al 2p spectra at 74.5 eV. $h\nu$ = 450 eV.

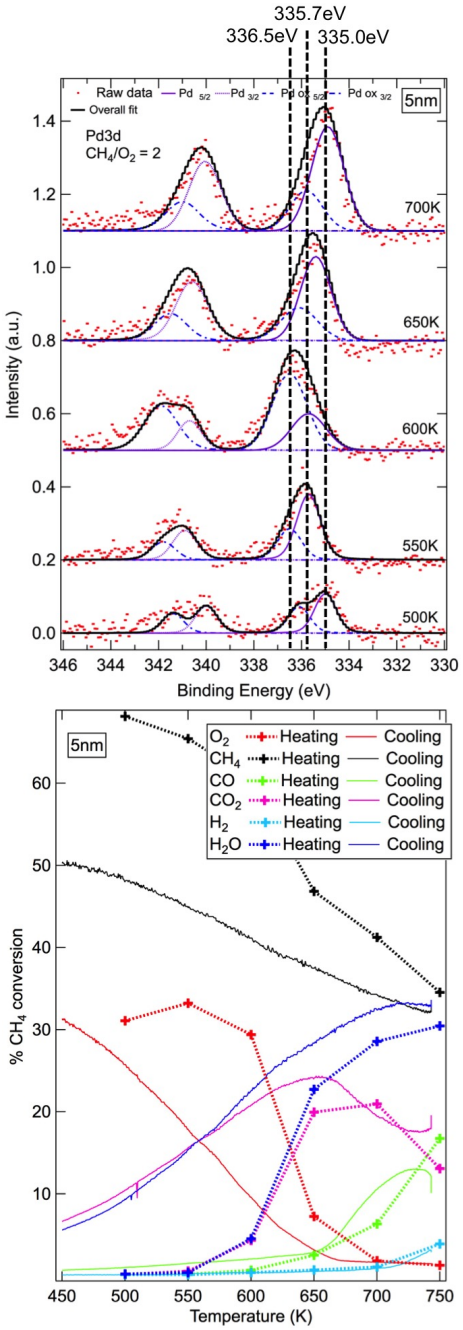

Figure 4.4: Catalyst B (Pd/Al_2O_3 nanoparticles of average size 5 nm). NAP-XP spectra in the Pd 3d region (top) and CH_4 conversion, calculated from mass spectroscopy data (bottom), recorded in the temperature range from 450 K to 750 K under 240 mTorr O_2:CH_4 pressure (1:2). "Heating": mass spectrometry at constant temperature during NAP-XPS measurements; "Cooling": recorded during continuous cooling from 750 K to 450 K. Binding energies are corrected to corresponding Al 2p spectra at 74.5 eV. $h\nu$ = 450 eV.

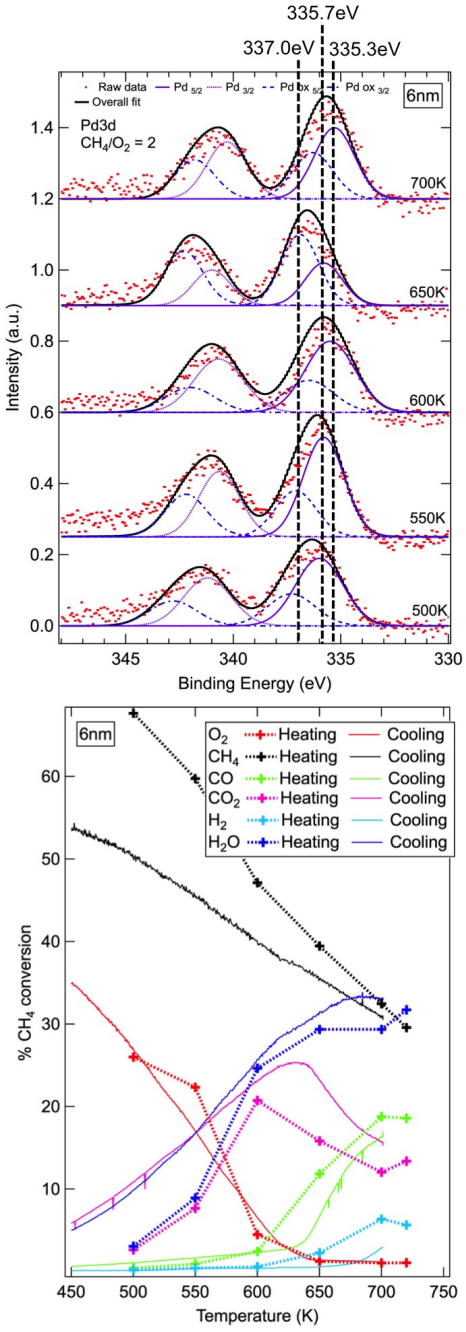

Figure 4.5: Catalyst C (Pd/Al_2O_3 nanoparticles of average size 6 nm). NAP-XP spectra in the Pd 3d region (top) and CH_4 conversion, calculated from mass spectroscopy data (bottom), recorded in the temperature range from 450 K to 720 K under 240 mTorr O_2:CH_4 pressure (1:2). "Heating": mass spectrometry at constant temperature during NAP-XPS measurements; "Cooling": recorded during continuous cooling from 720 K to 450 K. Binding energies are corrected to corresponding Al 2p spectra at 74.5 eV. $h\nu$ = 450 eV.

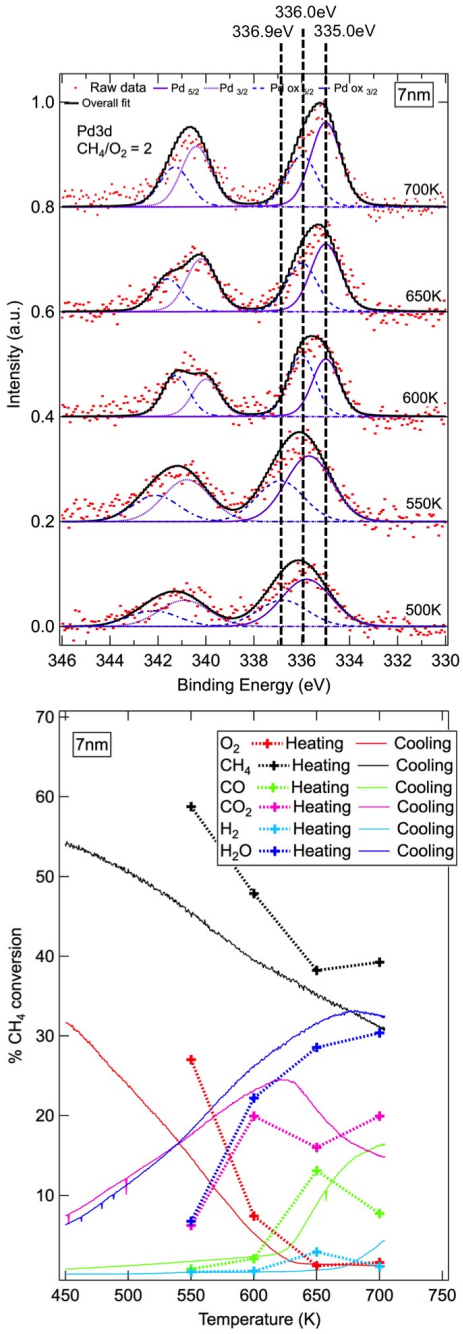

Figure 4.6: Catalyst D (Pd/Al_2O_3 nanoparticles of average size 7 nm). NAP-XP spectra in the Pd 3d region (top) and CH_4 conversion, calculated from mass spectroscopy data (bottom), recorded in the temperature range from 450 K to 700 K under 240 mTorr O_2:CH_4 pressure (1:2). "Heating": mass spectrometry at constant temperature during NAP-XPS measurements; "Cooling": recorded during continuous cooling from 700 K to 450 K. Binding energies are corrected to corresponding Al 2p spectra at 74.5 eV. $h\nu$ = 450 eV.

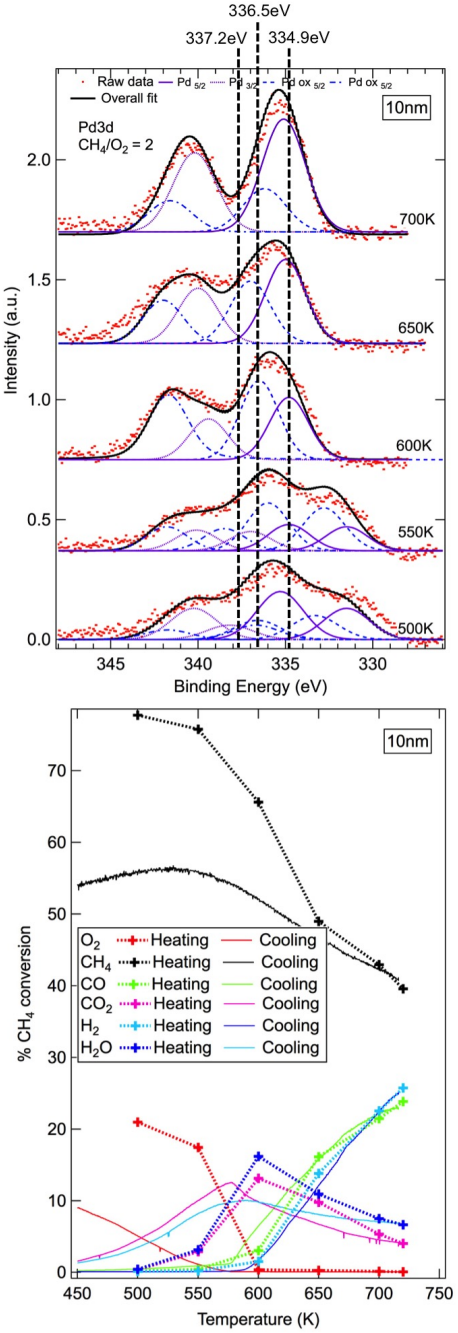

Figure 4.7: Catalyst E (Pd/Al_2O_3 nanoparticles of average size 10 nm). NAP-XP spectra in the Pd 3d region (top) and CH_4 conversion, calculated from mass spectroscopy data (bottom), recorded in the temperature range from 450 K to 720 K under 240 mTorr O_2:CH_4 pressure (1:2). "Heating": mass spectrometry at constant temperature during NAP-XPS measurements; "Cooling": recorded during continuous cooling from 720 K to 450 K. Binding energies are corrected to corresponding Al 2p spectra at 74.5 eV. $h\nu$ = 450 eV.

Catalyst	Pd 3d $_{5/2}$ Pd area	Pd 3d $_{5/2}$ PdO area	Pd : PdO ratio
A (4nm)	0.53	0.28	**1.89**
B (5nm)	0.49	0.19	**2.58**
C (6nm)	0.47	0.30	**1.57**
D (7nm)	0.27	0.16	**1.69**
E (10nm)	1.45	0.56	**2.59**

Table 4.3: Areas of Pd 3d $_{5/2}$ metallic Pd and Pd oxide peaks for Catalysts A – E at 700 K to three significant figures.

alysts of different sizes with respect to the temperature at which CO and H_2 are produced. Catalyst E (Figure 4.7, 10 nm) produces CO and H_2 at the lowest temperature (570 K) and, with the exception of Catalyst A (Figure 4.3, 4 nm), the catalytic activity with respect to syngas production decreases with decreasing particle size (Figure 4.17). The XPS data for Catalyst A (Figure 4.3) show a prominent peak at 337.1 eV at 550 K and 600 K, characteristic of a divalent Pd species (Pd^{2+}) [176]. This peak corresponds to the temperature at which POM products are starting to form according to the mass spectrometry data, suggesting PdO is the active phase of the catalyst. A slight hysteresis is observed, but the process is generally reversible on cooling down. Note, the modes of recording the mass spectrometry data were different: the temperature was increased in steps of 50 K and held constant for about 30 min while the NAP-XP spectra were recorded, after the experiments at the highest temperature (700 – 750 K) had been completed, the sample was allowed to cool down while recording mass the reactant and product partial pressure. The NAP-XPS data in Figure 4.4 for Catalyst B (5 nm) are slightly different from Catalyst A as the peak at 337.1 eV is not observed. At 600 K, a peak at 336.5 eV appears in the NAP-XP spectrum, which shifts downwards in binding energy with an increase in temperature. Syngas (CO and H_2) production, as shown in the conversion plot in Figure 4.4, does not occur until 700 K, suggesting the absence of the high binding energy peak (337.0 $\pm$ 2 eV) is reflective in the activity of Catalyst B.

In the CH_4 conversion data in Figure 4.3 for Catalyst A (4 nm) it can be observed that the increase in CO pressure begins just under 600 K. H_2 is produced around 650 K, which can explain why the peak at 334.9 eV reappears as the oxide has been reduced back to Pd^0. In comparing Catalysts C and D (Figures 4.5, 6 nm, and 4.6, 7 nm, respectively), there is a significant temperature dependence at which point the metallic Pd oxidises to the PdO_x species and the reverse reduction. The XPS data shown in Figure

4.5 for Catalyst C (6 nm) show the presence of a higher binding energy peak at 337.0 eV (PdO) slowly increasing from 550 K to 650 K, whereas the spectra for Catalyst D (7 nm, Figure 4.6) show a quick conversion from 336.9 eV to 336.0 eV between 550 K and 600 K. The peak at 336.9 eV in Figure 4.6 can be attributed to PdO. Its downward shift to 336.0 eV at 600 K could suggest a subsurface oxygen species, a surface 2D oxide such as Pd_5O_4 [177] or even a PdC species [178].

A large peak is observed in the C 1s spectra at 285 eV (Figure 4.8). This could be indicative of a PdC surface species, however adventitious carbon from impurities and the reactant gas CH_4 would also appear at this binding energy. Therefore it is impossible to identify whether a surface PdC species is present. The Pd appears predominately reduced again by 650 K, when the selectivity shifts towards partial oxidation. This can be correlated to the mass spectrometry data, which show that H_2 formation occurs at a lower temperature with Catalyst C (650 K) than with Catalyst D (677 K). XPS data for all catalysts show the reduced species is favoured at 700 K, which is supported by mass spectrometry showing an increase in H_2 formation at much higher temperatures, between 700 K and 750 K. Pd/Al_2O_3 nanoparticles with an average diameter of 10 nm (Catalyst E, Figure 4.7) also exhibit a PdO species (337.2 eV) that, on heating, reduces to a PdO_x or a subsurface-O species (336.5 eV). This reduction occurs at 600 K; the same temperature as the onset of CO formation, as shown in the lower panel of Figure 4.7. This suggests that the catalyst exists as a more reduced state during the production of syn-gas.

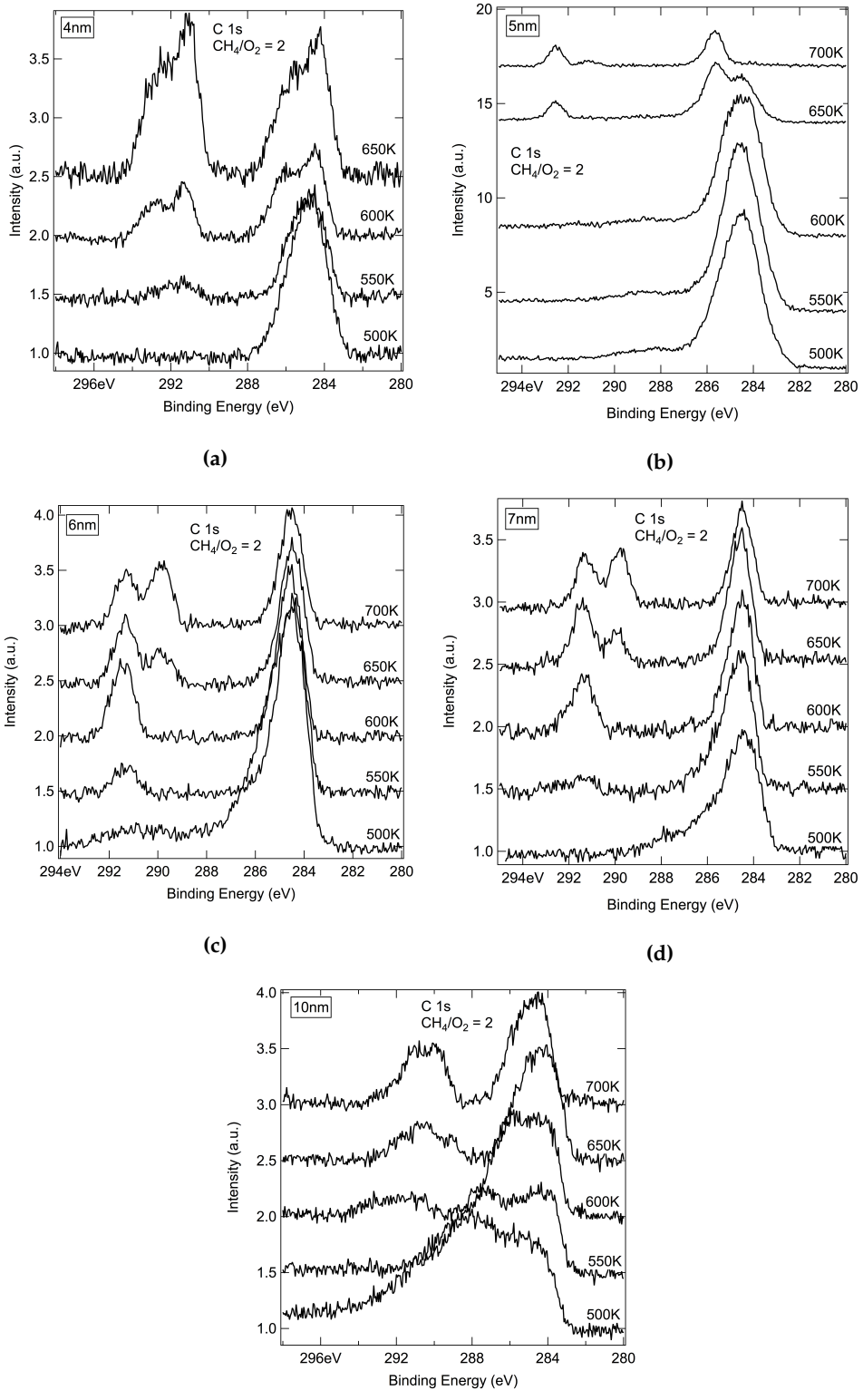

Figure 4.8: NAP-XP spectra in the C 1s region for 5 wt% Pd/Al_2O_3 catalysts with particle sizes 4 – 10 nm at a range of temperatures. $h\nu$ = 450 eV.

4.3.2 Gas Composition Effect: Complete oxidation vs Partial oxidation

Oxidising, or lean, conditions are favourable in diesel and natural gas vehicles because they significantly reduce the amount of NO_x emissions. High air to fuel ratios enable lower temperature combustion and as a result, NO_x emissions are greatly reduced from typically 5 g/kWh to 2 g/kWh [162]. With oxygen in excess, the favoured reaction should be complete oxidation of methane with the favoured products being CO_2 and H_2O:

$$CH_4 + 2\,O_2 \longrightarrow CO_2 + 2\,H_2O$$

In order to test the reactivity and surface chemistry of Pd/Al_2O_3 catalysts under different methane to oxygen ratios, the 4 nm catalyst was subjected to various gas compositions. Keeping the total pressure constant at 0.33 mbar, a series of NAP-XPS measurements were taken under excess oxygen concentrations: $[O_2]$:$[CH_4]$ = 5 and 2. Figure 4.9 shows the NAP-XP spectra in the Pd 3d region of 5 wt% Pd/Al_2O_3 4 nm catalyst under both gas compositions at increasing temperatures. At lower temperatures (500 – 600 K), the spectra show signs of charging by peak broadening and splitting. The charging is accounted for by fitting the spectra using the method outlined in Chapter 3.

The spectra under both conditions show the Pd is mainly in a PdO_x oxidised form until 650 K and 750 K under $[O_2]$:$[CH_4]$ = 2 and $[O_2]$:$[CH_4]$ = 5 respectively. Under $[O_2]$:$[CH_4]$ = 5 conditions, the Pd appears reduced only at 750 K (Figure 4.9a, Pd $3d_{5/2}$ = 335.7 eV), due to the high oxygen concentration in the gas feed. Under a lower concentration of O_2, the Pd reduces at a lower temperature and, as shown in Figure 4.10, the rate of CO formation is higher than under a higher O_2 concentration. The data suggest that the active phase of the catalyst for CO_2 production under oxidising conditions is Pd oxide. CO_2 formation begins at 550 K (Figure 4.10) for both complete oxidation gas compositions and Pd is still oxidised at this temperature, according to the NAP-XPS data (Figure 4.9).

For comparison, the binding energy values and mass spectrometry data have been included in Figures 4.9c and 4.10 respectively from the same catalyst under partial oxidation conditions, where $[O_2]$:$[CH_4]$ = 0.5. With reduced oxygen concentrations in the reaction feed, CO_2 production occurs 50 K lower than under highly oxidising conditions. Once Pd reduces at 600 K, CO_2 production decreases as the partial oxidation of methane becomes the dominant reaction.

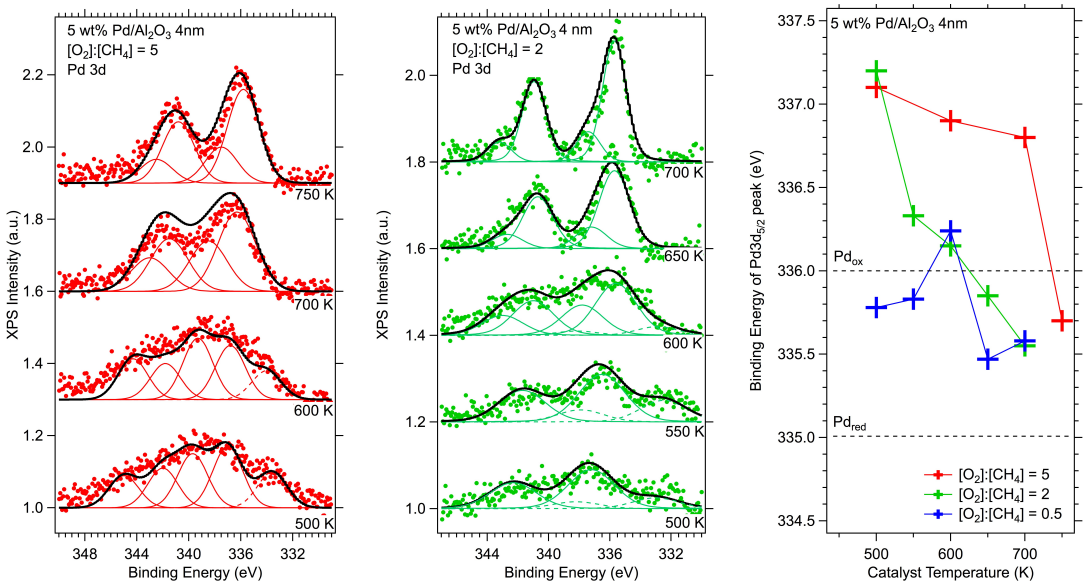

Figure 4.9: NAP-XPS data in the Pd 3d region for a 5 wt% Pd/Al_2O_3 catalyst (d = 4 nm) at increasing temperature under the gas feed ratios (a) $[O_2]$:$[CH_4]$ = 5 and (b) $[O_2]$:$[CH_4]$ = 2. $h\nu$ = 450 eV. (c) Plot of binding energy of the Pd $3d_{5/2}$ peak as a function of temperature for different gas feed ratios $[O_2]$:$[CH_4]$ = 5, 2 and 0.5.

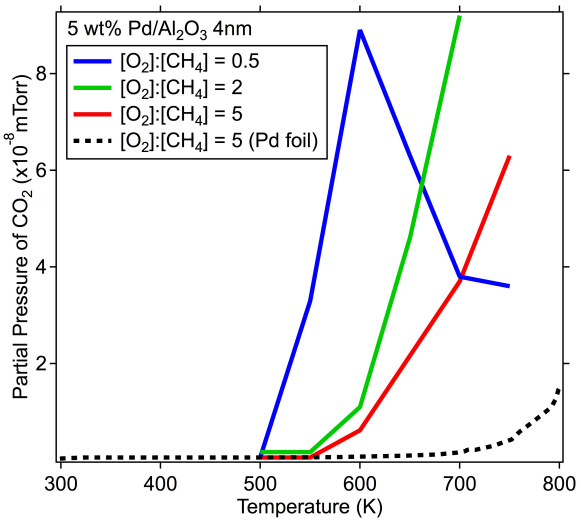

Figure 4.10: Mass spectrometry data showing the partial pressure of CO_2 as a function of temperature for the different gas feed ratios $[O_2]$:$[CH_4]$ = 5 (red line), 2 (green line) and 0.5 (blue line) with a 5 wt% Pd/Al_2O_3 catalyst (d = 4 nm). The CO_2 production with a polycrystalline Pd foil catalyst is also shown for comparison (black dotted line).

The same 5 wt% Pd/Al_2O_3 catalyst (d = 4 nm) was studied under equal pressures of oxygen and methane. According to mass spectrometry data (Figure 4.11d), there is a 5% conversion to CO, but the majority of methane is converted to complete oxidation products CO_2 and H_2O. The NAP-XPS data in the Pd 3d region (Figure 4.11a) show how the Pd in the catalyst reduces over time and with increased temperature as the oxygen is being used up in the reaction. The metal is in a PdO_x state until 750 K when it reduces, as shown by the binding energy shift from 336.1 eV at 700 K to 335.5 eV at 750 K. The oxidised surface for the majority of the temperature ramp causes complete methane oxidation to be the dominating reaction. CO_2 formation is also evident in the C 1s NAP-XP spectra in Figure 4.11c, as shown by the growing peak at 292 eV.

Table 4.4 shows the percentage conversion of methane to all main oxidation products for each gas composition. Complete oxidation of methane to CO_2 and H_2O occurs at lower temperatures than partial oxidation to H_2 and CO, so the percentages used for conversion to CO_2 and H_2O are the maximum values reached over the temperature ramp. The values used for conversion to H_2 and CO are the % conversions at the end of the temperature ramp, as this reaction occurs at higher temperatures at the product conversion reaches its maximum at the maximum temperature. Interestingly, the equal concentrations of oxygen and methane yield the highest conversion of methane to the complete oxidation products; carbon dioxide and water.

Reactants		Products (% CH_4 conversion)			
$[O_2]$	$[CH_4]$	H_2*	CO*	H_2O**	CO_2**
0.5	1	21	30	25	19
1	1	1	5	52	44
2	1	0.2	3	30	26
5	1	0.2	3	36	32

Table 4.4: The percentage conversions of methane to each main oxidation product for each gas composition studied. *Partial oxidation products: % CH_4 conversion taken at end of temperature ramp ($\sim$ 750 K)

**Complete oxidation products: maximum CH_4 conversion used

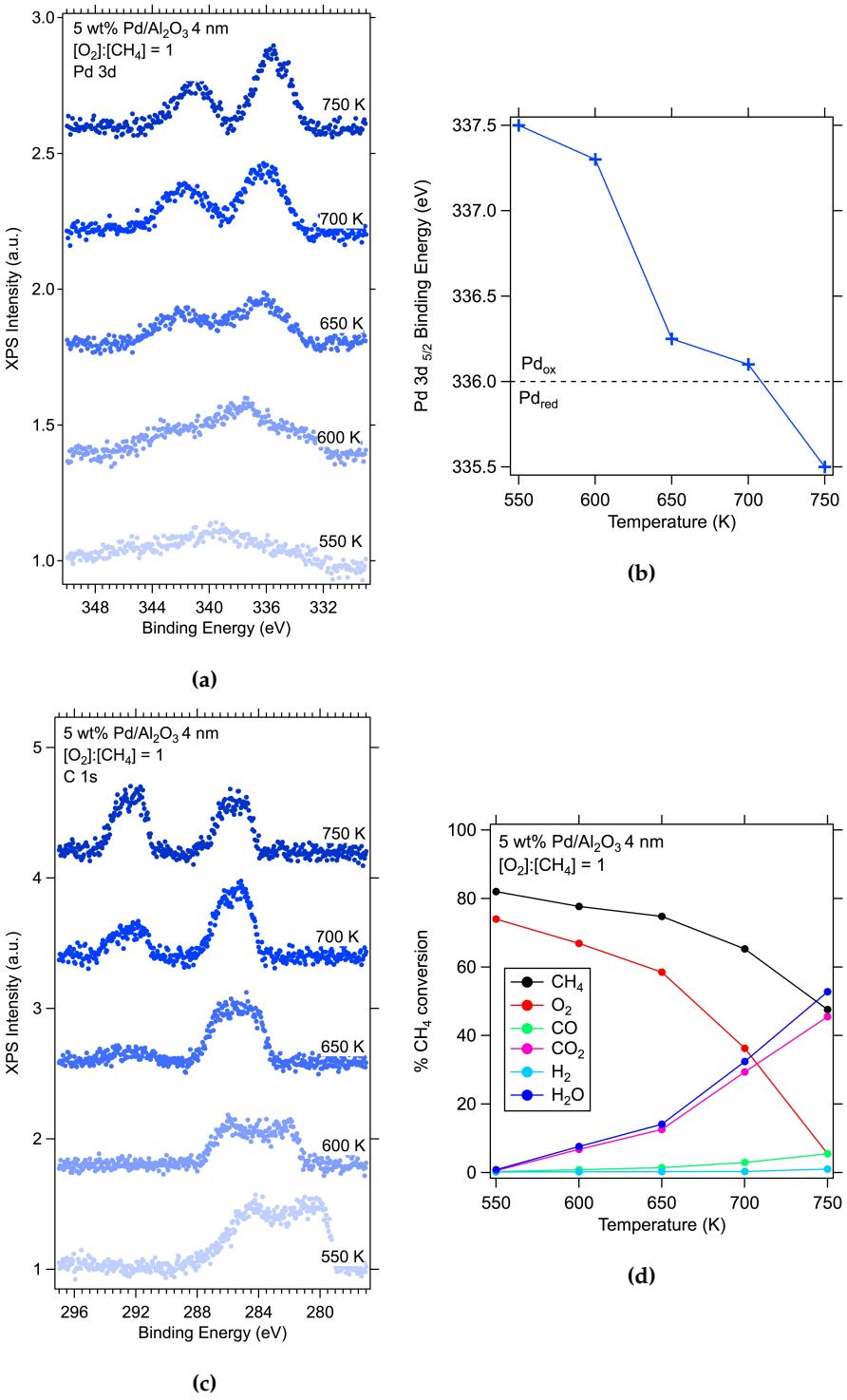

Figure 4.11: NAP-XPS data in Pd 3d (a) and C 1s (c) regions of 5 wt% Pd/Al_2O_3 catalyst (d = 4 nm) under equal pressures of O_2 and CH_4 (total pressure = 0.33 mbar) from 550 K to 750 K. $h\nu$ = 450 eV. (b) Plot of Pd $3d_{5/2}$ binding energy as a function of temperature to show how the Pd reduces with increased temperature. (d) % CH_4 conversion to oxidation products as a function of temperature, determined by mass spectrometry.

4.3.3 Synthesis Method Effect: Co-precipitation vs Impregnation

The Pd/Al_2O_3 catalysts used in the NAP-XPS study were all prepared using the co-precipitation technique, in which a colloidal solution of a palladium precursor is formed, the support material is added, and the solid supported catalyst is precipitated out [88, 179]. This method yields a small distribution of Pd particle size after calcination and a reasonably good dispersion of metal, although the completed reaction for each catalyst takes almost 36 h. Impregnation is an alternative method of producing highly dispersed supported Pd catalysts taking only approximately 30 min per catalyst.

A 5 wt% Pd/Al_2O_3 catalyst was prepared using by the incipient wetness impregnation technique. 5 wt% of Pd from a $Pd(NO_3)_2$ precursor solution (6.6 g), diluted with 2-3 ml of water, was added dropwise to 20g of γ-Al_2O_3 with constant stirring. More water was used to wash out the remaining $Pd(NO_3)_2$ and added to the mixture. The catalyst was then dried in an oven at 105 °C for four hours. The dried catalyst was either calcined at 500 °C or 1000 °C.

Both catalysts were subject to the in-house characterisation techniques at Johnson Matthey, which included TEM, CO chemisorption and lab-source XPS. TEM images of the catalyst are shown in Figure 4.12 for each calcination temperature, and the difference in size between the high and low calcination temperatures can easily be seen from the scale bars. The particles are generally elliptical with mean diameters of 5.5 nm (σ = 2.7 nm) and 34.5 nm (σ = 11.0 nm) for calcination at 500 °C and 1000 °C respectively. Metal dispersion is determined by CO chemisorption and the catalysts prepared by the impregnation method yielded a higher % Pd dispersion than the catalysts prepared by the co-precipitation method and calcined to the same temperatures, as illustrated in Figure 4.13. Metal dispersion decreases with increasing calcination temperature, due to the increased sintering at high calcination temperatures.

Despite a higher Pd dispersion with catalysts prepared by the impregnation method, the intensity of XPS signals is larger with the catalysts prepared by co-precipitation. Figure 4.14 shows lab-source XPS data of both catalysts at two different calcination temperatures (500 °C and 1000 °C). It is clear from the spectra that the catalyst prepared by co-precipitation gives a much higher XPS signal in the Pd 3d region for high and low calcination temperatures, and so this technique was the synthesis method used for the catalysts in the synchrotron NAP-XPS experiments.

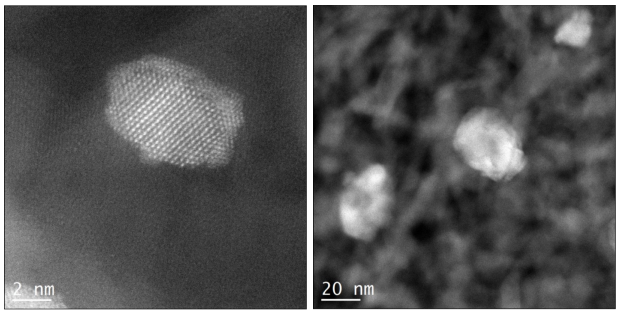

(a) 500 °C **(b)** 1000 °C

Figure 4.12: TEM images of 5 wt% Pd/Al_2O_3 catalyst prepared by the impregnation method, calcined to (a) 500 °C and (b) 1000 °C.

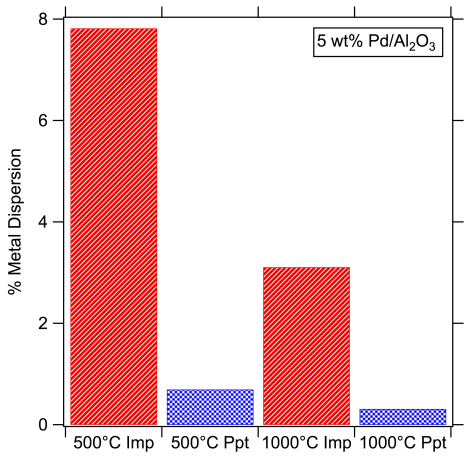

Figure 4.13: % dispersion of Pd atoms on the surface of 5 wt% Pd/Al_2O_3 catalysts prepared by co-precipitation and impregnation, as determined by CO chemisorption.

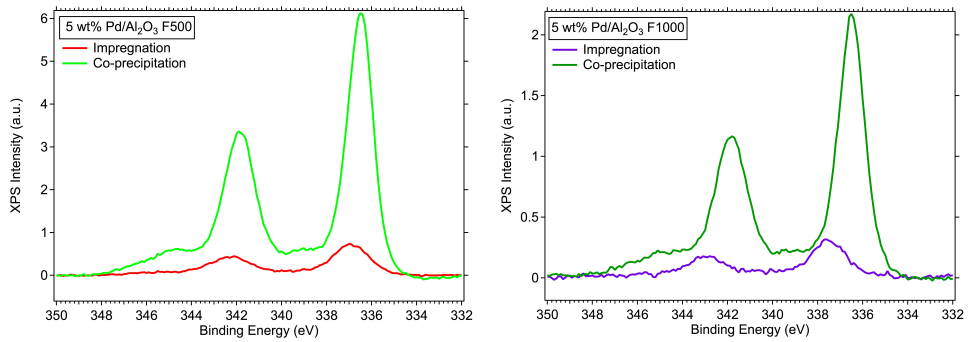

(a) **(b)**

Figure 4.14: Lab-source XPS data of 5 wt% Pd/Al_2O_3 samples prepared by co-precipitation and impregnation methods, calcined at (a) 500 °C and (b) 1000 °C.

4.4 Discussion

4.4.1 Activation Energy

Arrhenius plots of the mass spectrometry data recorded during cooling of the catalysts can be used to determine the activation energy of the formation of each product:

$$\ln(P) = \text{const.} - \frac{E_a}{R}\left(\frac{1}{T}\right) \tag{4.3}$$

where P is the partial pressure of each product, R is the gas constant (8.314 J mol^{-1} K^{-1}) and T is the sample temperature. Figure 4.15 shows the Arrhenius plots for each methane oxidation product where the activation energies are calculated from the gradient of the straight line and stated in Table 4.5. The complete oxidation of methane (Reaction 4.4) occurs at a lower temperature than the partial oxidation of methane (Reaction 4.5), and as a result the complete methane oxidation products (H_2O and CO_2) have much lower activation energies than the partial oxidation products (H_2 and CO):

$$\mathrm{CH_4} + 2\,\mathrm{O_2} \longrightarrow \mathrm{CO_2} + 2\,\mathrm{H_2O} \qquad (E_a = 17.9 - 36.5\ \mathrm{kJmol^{-1}}, 400 - 570\ \mathrm{K}) \tag{4.4}$$

$$\mathrm{CH_4} + \frac{1}{2}\,\mathrm{O_2} \longrightarrow \mathrm{CO} + \mathrm{H_2} \qquad (E_a = 109.7 - 218.8\ \mathrm{kJmol^{-1}}, 590 - 740\ \mathrm{K}) \tag{4.5}$$

Catalyst	**H_2**	**CO**	**H_2O**	**CO_2**
Pd/Al_2O_3	E_a (kJ mol^{-1})	E_a (kJ mol^{-1})	E_a (kJ mol^{-1})	E_a (kJ mol^{-1})
4 nm	186.8	146.7	25.1	25.1
5 nm	154.7	109.7	20.6	17.9
6 nm	178.8	128.5	24.9	23.5
7 nm	176.6	132.8	21.9	18.6
10 nm	218.8	159.1	36.5	36.4

Table 4.5: Calculated activation energies (E_a) for the onset of each product formation for Pd/Al_2O_3 catalysts under partial methane oxidation conditions ([CH_4]:[O_2] = 2 (0.33 mbar total pressure)).

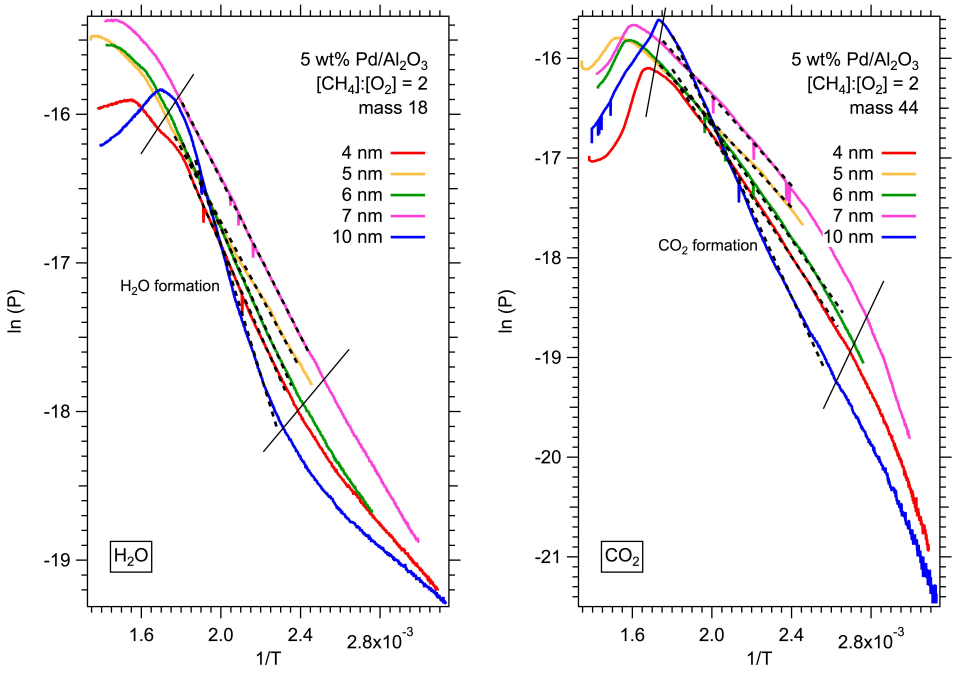

(a) H_2O (mass 18) **(b)** CO_2 (mass 44)

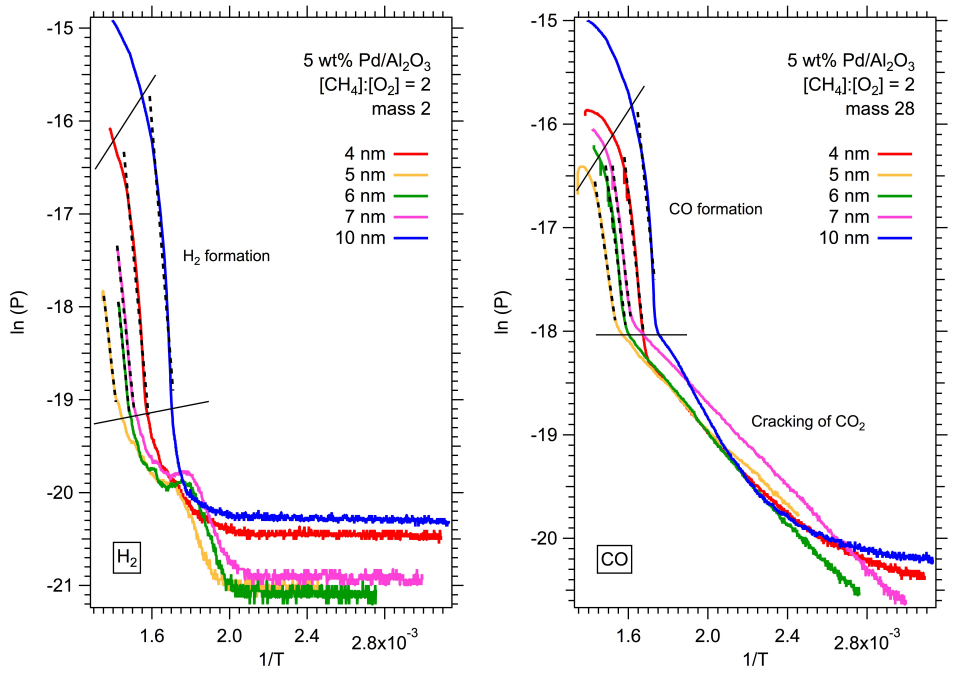

(c) H_2 (mass 2) **(d)** CO (mass 28)

Figure 4.15: Arrhenius plots of the partial pressures of each methane oxidation product produced with 5 wt% Pd/Al_2O_3 catalysts of different Pd particle sizes under 0.33 mbar ($[CH_4]:[O_2] = 2$). Partial pressures obtained from mass spectrometry on cooling of the catalyst. (a) H_2O, (b) CO_2, (c) H_2 and (d) CO.

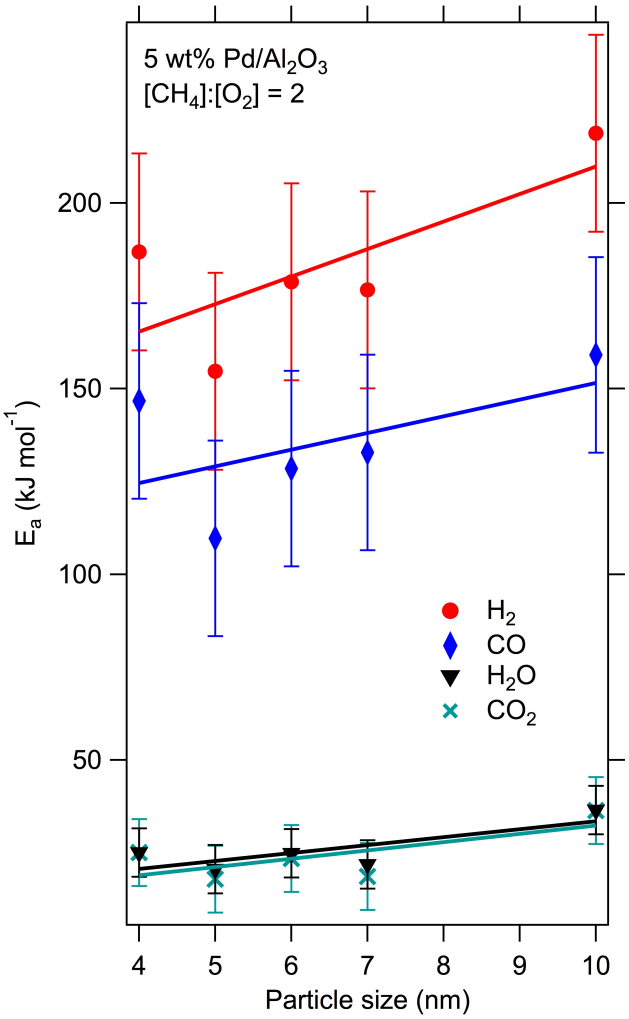

Figure 4.16: Activation energies for each methane oxidation product formation for each particle size. Error bars are calculated from the linear fit line for each product.

There is no significant particle size effect in terms of activation energy, as although the activation energies increase slightly with particle size, the values remain inside the error bar (Figure 4.16). However, particularly for CO_2 and H_2O, the activation energies for the 10 nm sample are different to those for the smaller particle sizes. This may be due to a difference in the number of available active sites in this sample, and the reduction of Pd at lower temperatures for larger particles affects the reactivity towards complete methane oxidation to CO_2 and H_2O.

4.4.2 Particle Size Effects and Oxidation States

These studies show that the catalytic activity, in terms of the temperature at which CH_4 conversion to CO and H_2 begins, increases with increasing particle size for Pd/Al_2O_3 nanoparticles over a range of particle sizes from 5 to 10 nm (Figure 4.17). Nanoparticles with an average diameter above 10 nm were not available in this study. Therefore, it is not clear whether there is an optimum particle size or a continuous trend. Pd single crystals and polycrystalline foils have been used as model catalysts in similar AP-XPS studies before [180,181] however, and show an onset of CO production at higher temperatures.

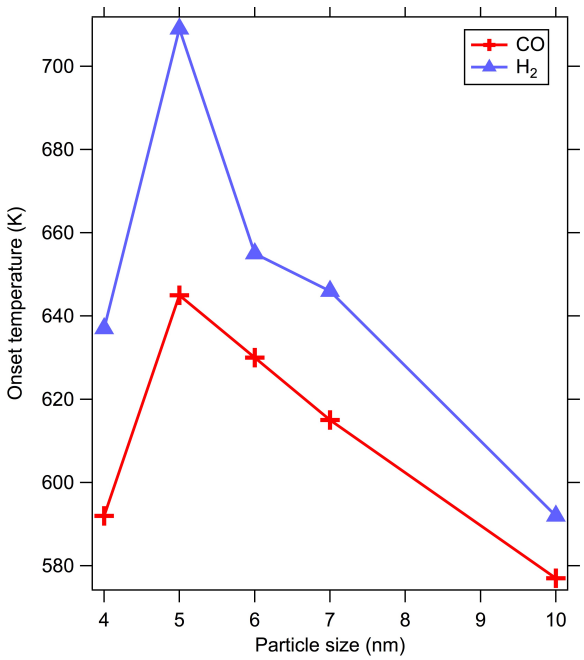

Figure 4.17: Temperature of CO and H_2 initial production vs. particle size.

Figure 4.18 shows the relative CO_2 production of polycrystalline Pd foil compared with Pd/Al_2O_3 nanoparticles when exposed to an oxygen-rich CH_4 environment ($[O_2] : [CH_4] = 5$). In comparison to supported metallic nanoparticles, the catalytic activity of polycrystalline Pd foil is insignificant. This would suggest that there is a volcano-type distribution of particle size as a function of activity, with an optimum size at some point between 10 nm and the grain size of the polycrystalline foil ($> 1\mu$m). Other studies using Pd/Al_2O_3 catalysts have also found activity increases with increasing particle size [182,183], explained by differences in electronic structure of nanoparticles < 3 nm that form stronger interactions with the reactant molecules [184]. Similar trends have been reported in the literature [185,186]

for palladium catalysts, in which there is an optimum or critical nanoparticle size for enhanced reactivity when testing a range of particle sizes. Semagina and co-workers [186] tested a size range of Pd nanoparticles from 6 nm to 14 nm and Pd black, and found that a significant increase in turnover frequency was observed with nanoparticles of 11 to 14 nm, but decreased with a Pd black catalyst in the micrometer range. It has also been previously reported that smaller particles have stronger metal-support interactions, which can render them less reactive with the reactant molecules because the palladium content on the surface decreases [187], and conversely, a weaker metal-support interaction makes the catalyst more active [164, 174].

The need for fundamental knowledge of how catalytic nanoparticles behave in-situ is becoming increasingly important. Model catalysts such as polycrystalline foils and single crystals cannot be used to study size effects and metal-support interactions of industrial catalysts. The NAP-XP spectra and mass spectrometry data shown in Figure 4.18, are indicative that a polycrystalline Pd foil behaves differently from supported nanoparticles under catalytic reaction conditions. At 700 K, a sharp PdO peak at 336.1 eV in the Pd foil spectrum is consistent with the rise in CO_2 formation shown in Figure 4.18. The peaks in the spectra for the nanoparticles are much broader, suggesting a mixture of both oxide and metal, contributing to a rise in catalytic activity at lower temperatures. It could be argued that reactant pressures of around 1 mbar are not representative of industrial catalysis conditions, as syngas is currently produced in a large scale reactor at 5-40 bar [188]. However, NAP conditions are considerably more realistic than ultra-high vacuum and reproduce the reaction yields achieved under industrial conditions.

The exact oxidation state of Pd during the reaction cannot be confirmed by XPS measurements alone. PdO_x species have binding energies between 335.5 eV to 337.0 eV [170, 176, 178]; therefore the exact nature of the oxide is not clear. It could be subsurface oxygen, bulk or surface PdO oxide, or a surface 2D oxide such as Pd_5O_4. These peaks could also indicate a carbon build-up on the Pd surface from the cracking of the reactants and products in the gas phase [189]. The particle size may have a direct impact on the nature of PdO_x, as smaller nanoparticles have increased metal-support interactions, which can in turn affect their thermal stability [190]. This would therefore lead to an increase in binding energy of the Pd $3d_{5/2}$ peak of the PdO_x species in smaller particles (<5 nm). It is probable that more than one oxidation state is present in the oxidised metal, as the fitted XPS peaks are still quite broad over this range and the increasing concentration of newly formed H_2 is simultaneously reducing Pd. Despite this

uncertainty in the exact nature of the oxidation state, in-situ XPS shows distinct changes in chemical state of the Pd surface as a function of temperature and a clear correlation with the catalytic activity.

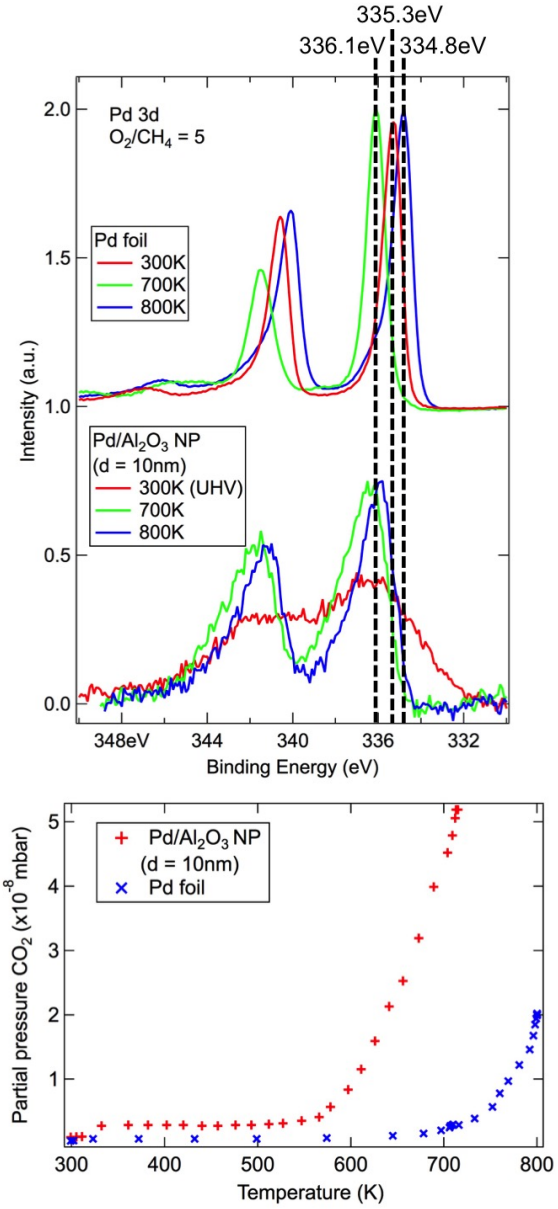

Figure 4.18: Comparison of polycrystalline Pd foil and Pd/Al_2O_3 nanoparticles calcined to 600°C (d = 10 nm): AP-XP spectra and partial pressure of CO_2 produced under O_2/CH_4 = 5 (total gas pressure = 0.33 mbar/240 mTorr) at 300 K, 700 K and 800 K.

4.5 Conclusions

A particle size effect has been observed in Pd/Al_2O_3 nanoparticles catalysing the partial oxidation of methane to syngas (CO and H_2). In general, CH_4 conversion to POM products occurs at lower temperatures for larger particles from 5 nm to 10 nm although no particle size effect is observed for activation energies of the formation of each product. This suggests that a pre-exponential factor should be considered in the Arrhenius equation that takes into account the reducibility and stability of the PdO. NAP-XPS data show the appearance of a metal oxide species around 550 – 650 K for all particle sizes, whilst mass spectrometry indicates the start of syngas production during these temperatures. As H_2 is produced, the oxide species on the Pd surface reduces to metallic Pd by 700 K, slowing down the production of CO. This suggests the formation of the oxide species is the driving force in initial product formation. A mixture of PdO and metallic Pd is needed to maintain the reaction as we observe an increase in intensity of the Pd metal NAP-XPS peaks (335 eV) at the same temperatures at which product formation increases, as shown by mass spectroscopy. A full reduction of the oxide to metal is detrimental to the catalytic process.

5 Partial Oxidation of Methane: NAP-XPS and Pd/SiO_2 catalyst

Abstract

Four 5wt% Pd/SiO_2 catalysts prepared with various nanoparticle sizes were studied with near-ambient pressure x-ray photoelectron spectroscopy (NAP-XPS), whilst under partial oxidation of methane conditions. The catalysts, ranging in average particle diameter from 2 – 6nm, were each exposed to 0.33 mbar total pressure of methane and oxygen in a 2:1 ratio. The chemical state of the surface of the catalysts and the reaction products (CO, CO_2, H_2O and H_2) were monitored before, during and after the reaction by NAP-XPS and mass spectrometry.

NAP-XPS data show the Pd in its oxide form between 500 – 600 K. At these lower temperatures, mass spectrometry data show an increase in partial pressures of CO_2 and H_2O. As the temperature is increased, reduction of Pd occurs whilst CO_2 and H_2O formation slows. This reduction of PdO to PdO_x ($0 \leq x < 1$) corresponds to syngas formation, as shown by an increase in the mass spectrometer signal of both masses 2 and 18 at this temperature. The temperature at which this reduction occurs is dependent on particle size: the larger the particle size, the lower the temperature at which Pd reduces from its oxide state to a more reduced state.

A binding energy shift within the Pd $3d_{5/2}$ region is observed and changes with particle size. The fitted peak representing the reduced Pd species shifts during a 500 K to 700 K temperature ramp, ranging from a 0.6 eV shift for 2 nm nanoparticles to a 1.7 eV shift for 6 nm nanoparticles. In general, the activity of Pd/SiO_2 catalysts towards syngas formation is increased with a larger average particle diameter.

5.1 Introduction

Natural gas, comprising predominately of methane, is a preferable candidate for environmentally friendly fuel due to the relatively "clean" emissions it produces on burning in comparison with other hydrocarbons and fossil fuels [56]. According to the Intergovernmental Panel on Climate Change (IPCC), methane contributes to 16% of the total greenhouse gases emitted globally by human activities [191], superseded only by carbon dioxide. Converting methane to its oxidation products H_2 and CO, or synthesis gas ("syngas"), is an economically viable route to hydrogen production, which can be separated and used in fuel cells [192, 193]. Pd/SiO_2 is a traditional catalyst used in the complete combustion and partial oxidation of natural gas [56, 194–197] and the role of silica as a support material is a much argued debate amongst the literature [195, 198–200].

Silica is a common support for many catalysts due to its high thermal stability [56]. SiO_2 is favoured over other catalytic supports such as TiO_2 for this reason. Veith and co-workers report the use of silica as the support for gold nanoparticles to catalyse CO oxidation for its thermal stability (up to 500°C under an oxygen environment) and facile regeneration [201]. Joo and co-workers used Pt/SiO_2 nanoparticles for high temperature CO oxidation and ethylene hydrogenation, as they were found to be more stable (and hence more active) than pure Pt nanoparticles [202]. Mesoporosity is another property of silicas that make them good catalytic supports. With potentially tunable pore sizes in the nanometer range, mesoporous silica as a support can increase the metal surface area, distribution and stability [203–206]. It is these features as to why silica is the predominantly used material in zeolite frameworks, with many reporting higher catalytic activity with an increase in Si/Al ratio [204, 207]. Wragg et al. report the flexibility of the O-Si-O bond angle and variety of bond lengths in a pure silica zeolite are the properties accounting for the uniqueness of this material, and lead to a wide range of possible SiO_2 and SiO_4 structures [204].

The morphology of silica can be tuned by controlling temperature, pH, precursor concentrations and calcination conditions. These same factors can also determine how the surface of the silica is terminated and, depending on the desired outcome of the reaction, the nature of this surface termination can be altered accordingly [206]. The most stable surface groups formed on silica as a result of chemically bound water are hydroxyl, or silanol, groups (Figure 5.1). The silanol moieties (SiOH) can either be single stand-

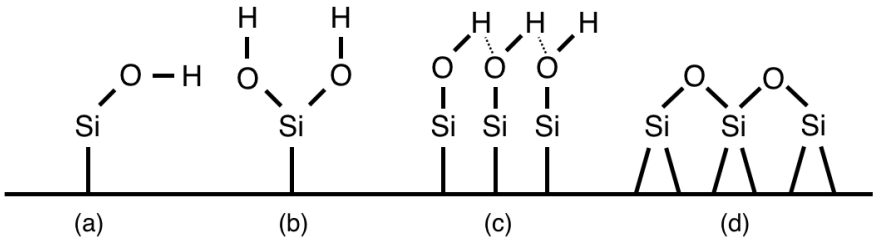

Figure 5.1: Possible silanol terminations of silica. (a) Single silanol, (b) geminal silanol, (c) vicinal silanols formed through hydrogen bonding and (d) siloxanes.

alone hydroxyls (Figure 5.1a) or an SiO_2 termination can be hydrogenated to form $Si(OH)_2$ (Figure 5.1b). A third outcome is also possible, in which multiple neighbouring single silanol moieties are hydrogen bonded (Figure 5.1c). Other terminations such as siloxanes are also common in a pure silica support material, whereby two neighbouring Si atoms are separated by a bridging O atom (Figure 5.1d) [206, 208]. The differing terminal silanol groups can determine the activity of the catalyst and the reaction pathway of the reactants [209], as the hydrophobicity of the silica is altered [208]. It is for this reason that understanding how including water in the reaction feed for methane oxidation affects the catalyst is currently of great interest [38]. It has also been reported in the literature that water as a reaction product of the complete oxidation of methane is enough to negatively affect the activity of the catalyst [38,45], by reacting with PdO to form $Pd(OH)_2$ species that subsequently block and diminish PdO active sites [210,211].

In terms of methane oxidation, reports suggest the reaction orders of silica-supported catalysts are lower than alumina-supported palladium [162, 195] and supposedly due to a weak metal-support interaction, Pd/SiO_2 catalysts have exhibited higher activity than Pd/Al_2O_3 catalysts [195]. Baldwin and Burch reported that activation of silica-supported Pd was faster than alumina-supported Pd due to a quicker reconstruction of the palladium [212], although Pd/Al_2O_3 catalysts exhibit higher activity overall [35]. Pd/SiO_2 catalysts have been shown to be reasonably unaffected by sulphur poisoning. Hoyos et al. reported that, under lean methane oxidation conditions, the addition of H_2S into the reaction feed caused the formation of a palladium sulphate species which initially deactivated the reaction. However, this species decomposes at high temperatures, therefore the Pd active sites are regenerated as well as the catalytic activity. This effect was not seen in a Pd/Al_2O_3 catalyst, in which H_2S became trapped and subsequently fully oxidised to SO_2 and SO_3 [37, 162]. Like many Pd catalysts, a Mars-van Krevelen

mechanism has been suggested for Pd/SiO_2 during methane oxidation, in which the rate determining step is the reduction of PdO by dissociated methane [24]. Thus, the methane oxidation activity of Pd catalysts is perhaps dependent on its ability to be reduced by methane [40].

There are different ways in which methane can react with oxygen, independent of the methane to oxygen ratio in the reaction feed (Reactions 5.1, 5.2 and 5.3). Therefore, although this Chapter focusses on the partial oxidation of methane, it is still possible that a reasonable concentration of CO_2 and H_2O will be produced alongside syngas.

$$\mathrm{CH_4} + \frac{1}{2}\,\mathrm{O_2} \longrightarrow \mathrm{CO} + \mathrm{H_2} \tag{5.1}$$

$$\mathrm{CH_4} + \frac{3}{2}\,\mathrm{O_2} \longrightarrow \mathrm{CO} + 2\,\mathrm{H_2O} \tag{5.2}$$

$$\mathrm{CH_4} + 2\,\mathrm{O_2} \longrightarrow \mathrm{CO_2} + 2\,\mathrm{H_2O} \tag{5.3}$$

Few spectroscopic studies explore the *in-situ* behaviour of silica and silica-supported catalysts, and so the metal-support interaction between palladium and silica under reaction conditions is still not fully known. Lamber et al. observed formation of palladium silicides (Pd_2Si, Pd_3Si) with high temperatures and hydrogen atmosphere, due to an increase in Pd-Si interaction under these conditions [213, 214]. There are different theories as to how the intermetallic compounds are formed: either by metal particle migration facilitated by mobile surface silanol groups [214], or by diffusion of Pd atoms into bulk vacant oxygen sites in the silica support [199, 215, 216]. Despite these observations, there is no definitive evidence to suggest this behaviour makes for a less active catalyst in comparison to other supports. Activity and selectivity appear to be dependent on reaction conditions, metal atom and pretreatment of the catalyst. This Chapter aims to clarify and explore the activity of Pd/SiO_2 catalysts under partial oxidation of methane conditions and to characterise the chemical state of the metal, the support and their interaction *in-situ*.

5.2 Experimental

5.2.1 Sample Preparation

5 wt% Pd/SiO_2 nanoparticles were prepared by a colloidal co-precipitation technique, using a $Pd(NO_3)_2$ precursor (8.34% assay, Alfa-Aesar). The aqueous $Pd(NO_3)_2$ solution was added dropwise to a stirring solution of aqueous Na_2CO_3 (Sigma-Aldrich) and dodecenyl succinic anhydride (Sigma-Aldrich) in THF. The combined solutions were heated to reflux and stirred for 24 h before the silica was added. After stirring for a further 2 h, the slurry was filtered off and dried under suction. The solid catalyst was then dried in an oven for 2 h at 105 °C.

The dried Pd/SiO_2 samples were separated into different batches for calcination. Each batch was crushed and calcined in a dry oven at a different temperature in order to achieve a range of average Pd particle diameters. The calcination temperatures ranged from 573 – 1273 K (300 – 1000 °C). The average particle diameter achieved at each temperature are outlined in Table 5.1. The particle sizes obtained for Pd/SiO_2 were smaller than for Pd/Al_2O_3, despite calcining to the same temperatures. The maximum diameter obtained was 6 nm by calcining to 700 °C. Higher calcination temperatures (up to 1000 °C) caused sintering of the Pd and low dispersion.

5.2.2 Sample Characterisation

The Pd/SiO_2 catalysts were characterised using a number of techniques available at Johnson Matthey Technology Centre, Sonning Common, UK. Properties of the catalysts including surface composition, mean particle diameter and reactivity were determined in-house.

The surface composition of each catalyst was measured by x-ray photoelectron spectroscopy (XPS), using a Thermo Escalab 250 equipped with an Al Kα x-ray source ($h\nu$ = 1486 eV). The samples were prepared for XPS by mounting the catalysts directly onto adhesive carbon tape. Trace contaminants were identified by overview spectra, spanning the binding energy range 1350 – -10 eV (pass energy = 150 eV), whilst high-resolution scans were executed on the regions of interest: Pd 3d, Si 2p and O 1s (pass energy = 30 eV). Charge compensation methods were employed during the data collection to replenish the electrons lost from the x-ray ionisation and therefore preventing a build up of negative charge on

the insulating support.

Figure 5.2 shows the high-resolution XP spectra in the Pd 3d, Si 2p and O 1s regions for each of the calcined Pd/SiO_2 catalysts, at room temperature under an ultra-high vacuum (base pressure 10^{-9} mbar). A linear background has been subtracted from the normalised spectra, and the binding energy for each sample was corrected using the Si 2p signal as a reference and the literature value for SiO_2 as 103.3 eV [217]. The binding energy of the Pd $3d_{5/2}$ peak (dotted line Figure 5.2(a)) is 336.3 eV ($\pm$ 0.1 eV), suggesting the palladium is in its most stable oxide form, PdO. The catalyst calcined to 1273 K (blue curve) has a slightly higher binding energy (337.0 eV), but this can still be attributed to PdO [218]. The oxygen peak (O 1s, Figure 5.2(c)) at 532.8 eV ($\pm$ 0.1 eV) represents the oxide in the silica support [219]. Figure 5.3 shows the area under the Pd 3d spectral lines as a function of temperature. There is a strong correlation between peak area and calcination temperature from 573 – 973 K, although the peak area of the catalyst calcined to 1273 K is much lower than any other catalyst, likely due to sintering of the Pd.

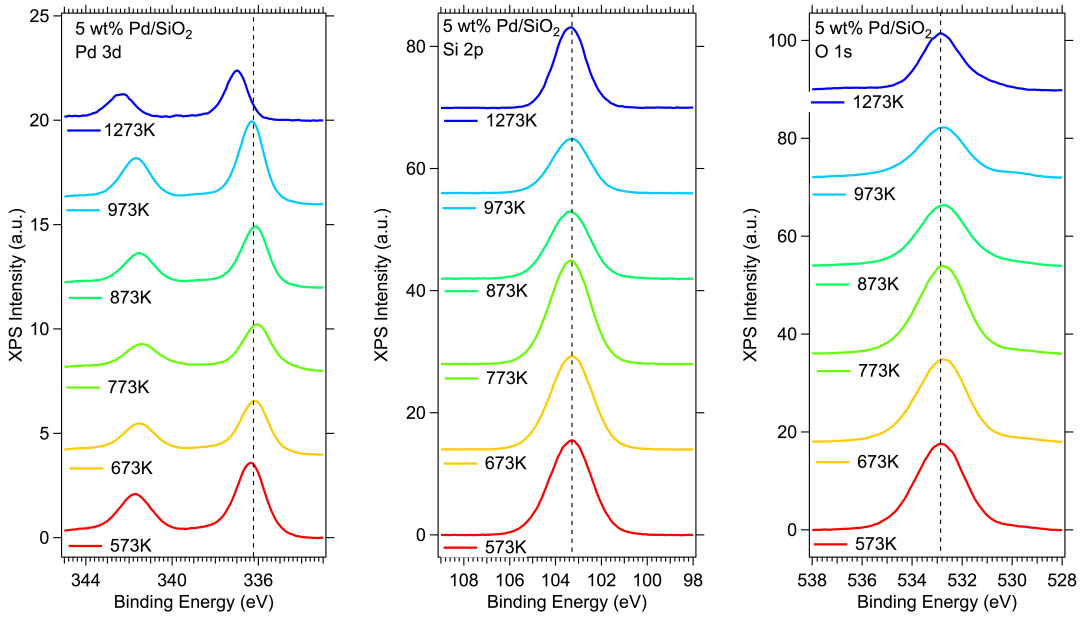

(a) Pd 3d **(b)** Si 2p **(c)** O 1s

Figure 5.2: High-resolution XPS data of Pd/SiO_2 catalysts, each calcination temperature represented by a different colour. (a) Pd 3d region, (b) Si 2p region and (c) O 1s region ($h\nu$ = 1486 eV)

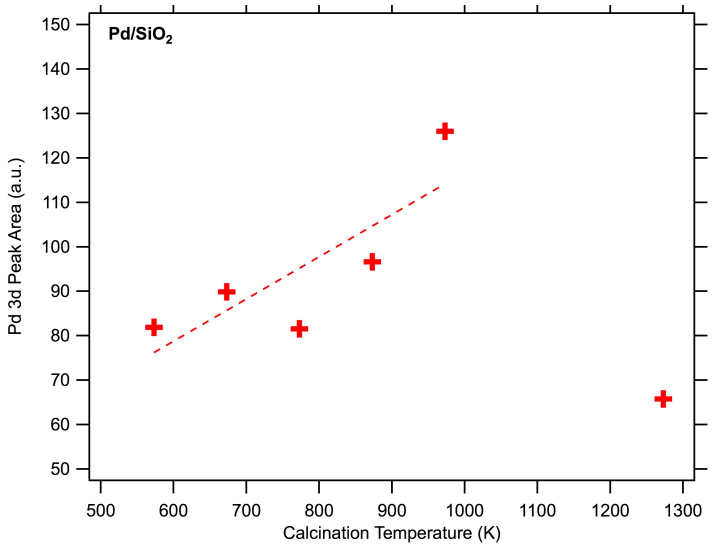

Figure 5.3: Peak area of Pd 3d spectral lines as a function of calcination temperature

Transmission electron microscopy (TEM) was used to determine the average size of each batch of calcined nanoparticles. The particle size analysis was completed by removing the background of the images and measuring the remaining particles with respect to the scale bar. Where possible, approximately 50 particles were counted and their diameters averaged, except in the case of Catalyst A where not enough particles were found to conduct a proper analysis. The resulting diameters and standard deviations are listed in Table 5.1. Crystallite sizes were also determined using x-ray diffraction (XRD). XRD data was collected by a Bruker AXS D8 diffractometer and a Cu Kα x-ray source. The Pd crystallite sizes obtained from XRD are also shown in Table 5.1 and are in good agreement with the TEM particle size analysis. Pd dispersion and surface area were determined by pulse CO chemisorption, using a Micromiretics AutoChem II 2920 instrument at Johnson Matthey. The catalyst samples are first flushed with H_2 to reduce the Pd before CO is pulsed through the catalyst. Adsorbed CO is measured by a thermal conductivity detector. Metal surface area and dispersion are calculated using Equations 5.4 and 5.5 respectively, where N_S is the number of surface Pd atoms available for catalysis and N_T is the total number of Pd atoms in the catalyst sample.

$$Area\ of\ Pd = \frac{molecules\ of\ CO\ adsorbed}{molecules\ per\ m^2} \tag{5.4}$$

$$MD(\%) = \frac{N_S}{N_T} \times 100 \tag{5.5}$$

		Mean Particle Diameter (nm)			
Catalyst	Calcination Temp. (K)	TEM*	XRD**	MSA (m^2/g)***	MD (%)***
A	573 (300°C)	–	~ 2	0.22	0.97
B	673 (400°C)	2.4 ± 0.8	2.7 ± 0.2	0.67	2.99
C	773 (500°C)	3.1 ± 1.8	3.4 ± 0.3	0.65	2.90
D	873 (600°C)	3.4 ± 1.0	3.7 ± 0.3	0.87	3.89
E	973 (700°C)	5.9 ± 2.5	5.9 ± 0.4	0.18	0.81
F	1273 (1000°C)	300 – 400	–	0.03	0.14

Table 5.1: *Average particle size determined by TEM

**Average particle size determined by XRD

***Metal Dispersion (MD) and Metal Surface Area (MSA) per gram of sample determined by CO chemisorption

5.2.3 Synchrotron Experiments

Catalysts A, B, D and E (2 nm, 3 nm, 4 nm and 6 nm) from Table 5.1 were selected and pre-prepared for synchrotron experiments by spray-coating 1 cm $\times$ 1 cm pieces of P-doped silicon wafers with an aqueous suspension of the catalyst. The water was left to evaporate to leave a homogenous layer of catalyst on the silicon wafer substrate. The silicon wafers were weighed on a four-place balance before and after spray coating in order to quantify the amount of catalyst. The surface area of Pd can therefore be determined knowing that the total surface area is the product of the number of Pd nanoparticles and the area of one nanoparticle. The number of nanoparticles and the area of one nanoparticle (assuming only half the nanoparticle is available for catalysis) are determined by Equations 5.6 and 5.7 respectively:

$$number\ of\ NPs = \frac{amount\ of\ catalyst\ on\ Si\ wafer\ (kg) \times metal\ loading\ (\%)}{\frac{1}{2} \cdot \left(\left(\frac{4\pi}{3}\right) \left(\frac{d}{2}\right)^3 \rho \right)} \tag{5.6}$$

$$area\ of\ one\ NP = \frac{\pi d^2}{2} \tag{5.7}$$

where d is the particle diameter and ρ is the the density of Pd (11.9×10^3 kg m^{-3}). The calculated values for the Pd/SiO_2 catalysts used here are shown in Table 5.2. The Pd surface areas are in the 10^{-3} m, or 10 cm^2 range, 20 – 75$\times$ larger than that of a single crystal.

d (nm)	N_{NP}	A_{NP} (m^2)	Pd surface area (m^2)
2	6.02×10^{14}	6.28×10^{-18}	3.78×10^{-3}
2.7	6.52×10^{14}	1.15×10^{-17}	7.47×10^{-3}
3.7	9.51×10^{13}	2.15×10^{-17}	2.04×10^{-3}
5.9	6.25×10^{13}	5.47×10^{-17}	3.42×10^{-3}

Table 5.2: Surface areas of Pd/SiO_2 catalysts coated on silicon wafer. N_{NP} = number of Pd nanoparticles, A_{NP} = area of one Pd nanoparticle

The presented NAP-XPS and mass spectrometry data were recorded at beam line 9.3.2 at the Advanced Light Source, USA [132]. The NAP-XPS chamber was set up as described previously [65] and the spray-coated silicon wafer was secured via tungsten clips to a custom-designed, UHV compatible sample holder with a ceramic button heater. To ensure charging of the insulating support would not be a problem at higher temperatures, one sample was heated in an ultra-high vacuum to 800 K. Figure 5.4 shows a time-resolved, two-dimensional x-ray photoelectron spectrum in the Si 2p region taken during a temperature ramp from room temperature (300 K) to 800 K, and how the conductivity of silica increases with increasing temperature. The peak at 99.0 eV is representative of the silicon wafer substrate, which is silicon in its elemental form and therefore already conducting. The silicon dioxide peaks are split into two (111.0 eV and 103.5 eV) at 300 K, corresponding to native oxides on the wafer and SiO_2 support. With increasing temperature they begin to converge by the higher binding energy peak shifting back, indicating that the conductivity of the oxide is increasing.

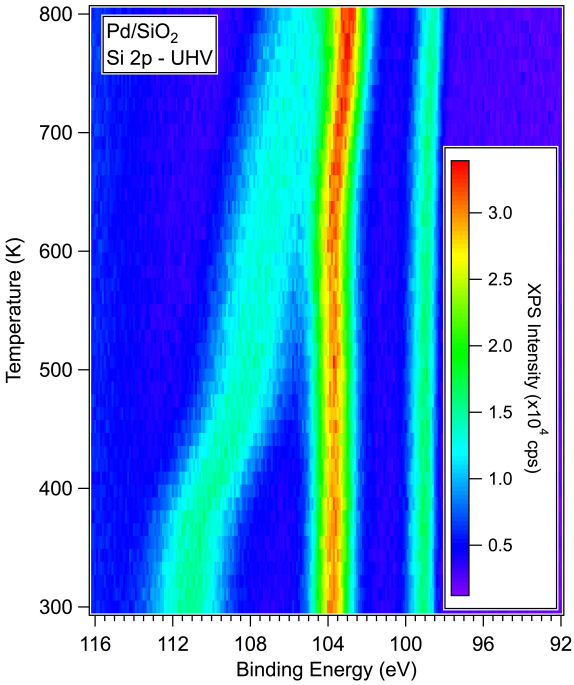

Figure 5.4: Temperature-programmed XP spectrum of Si 2p, showing conductivity as a function of temperature. $h\nu$ = 650 eV.

For the methane oxidation experiments, the sample was initially heated to 500 K and characterised in UHV before introducing 160 mTorr (0.22 mbar) of CH_4, followed by 80 mTorr (0.11 mbar) of O_2. The gas composition ratio was $[CH_4]$:$[O_2]$ = 2 in order to mimic the stoichiometric ratio of partial methane oxidation to syngas. The catalyst was then heated in 50 K intervals and stabilised at each temperature for NAP-XP spectra to be recorded. Under ambient pressures, the temperature of the sample is limited to 750 K and so this was the maximum temperature studied. Time resolved spectra in the Si 2p region were also recorded ($\sim$90 s/spectrum) during cooling of the sample to 300 K before pumping out the gases fully. A quadruple mass spectrometer located between the analyser nozzle and first differential pumping stage was continuously running throughout the experiment to quantify gas conversion and production. NAP-XPS data were taken in the Pd 3d, O 1s and Si 2p regions using a photon energy of 650 eV. C 1s spectra were recorded with 400 eV photon energy, with a Si 2p spectrum also taken at 400 eV to use for the binding energy correction. 100 eV pass energy was used for all spectra in order to maximise signal intensity. All spectra were normalised with respect to the background count rate at the low binding energy side and a linear background was subtracted. The peaks were fitted using a custom fitting procedure based on the psuedo-Voigt function, as described in Chapter 3.

5.3 Results

The series of Pd/SiO_2 catalysts as described above were studied by NAP-XPS and mass spectrometry in-situ. Two primary effects were observed: a particle size effect in which the reduction of the Pd and subsequent syngas formation occurs at different temperatures depending on the particle size; and an interaction between the silica support and the palladium nanoparticles.

5.3.1 NAP-XPS

Figure 5.5 shows the NAP-XP spectra in the Pd 3d region for each particle size studied under partial methane oxidation conditions. The temperature was held at intervals of 50 K where a spectrum was taken in the Pd 3d, O 1s, Si 2p regions at $h\nu$ = 650 eV, and also in the C 1s region, with a corresponding Si 2p spectrum, at $h\nu$ = 400 eV. Data acquisition for each temperature took approximately 1 h. The binding energy was corrected with respect to the Si 2p (SiO_2) peak at the same photon energy. The peaks were fitted using the custom fit function as described previously [65] taking the binding energy shift, peak width and peak splitting of the Si 2p (SiO_2) peak into consideration. Each Pd $3d_{5/2}$ peak is fitted with two peaks representing two different Pd phases; PdO (higher binding energy, 336.5 – 338.0 eV) and PdO_x, a more reduced Pd species where $0 \leq x < 1$ (lower binding energy, 335.0$\pm$1.0 eV). Using the literature value for the spin-orbit spacing between the Pd $3d_{5/2}$ and Pd $3d_{3/2}$ peaks (5.27$\pm$0.2 eV [220]) and a 2:1 intensity ratio, the Pd $3d_{3/2}$ PdO and PdO_x peaks can also be fitted. The value for the full width of half maximum is determined from the SiO_2 peak in the Si 2p region and so is kept constant for each of the fits in each Pd 3d spectrum, independent of Pd species. In Figure 6.3, the oxidised Pd species and reduced Pd species are represented by blue and red lines respectively. In some cases, particularly for the larger particle sizes (Figures 5.5c and 5.5d), each spin-orbit Pd 3d peak is fitted with three peaks (black dotted line). This extra peak is likely to be an artefact of sample charging.

Each series of NAP-XP spectra taken for each particle size show the reduction of PdO to PdO_x at some stage during the temperature ramp. The reduction is noted by the change within the Pd $3d_{5/2}$ peak, wherein both the intensity and area ratios of the PdO:PdO_x peaks shift in favour of the PdO_x peak, suggesting a more reduced surface (Figure 5.6a).

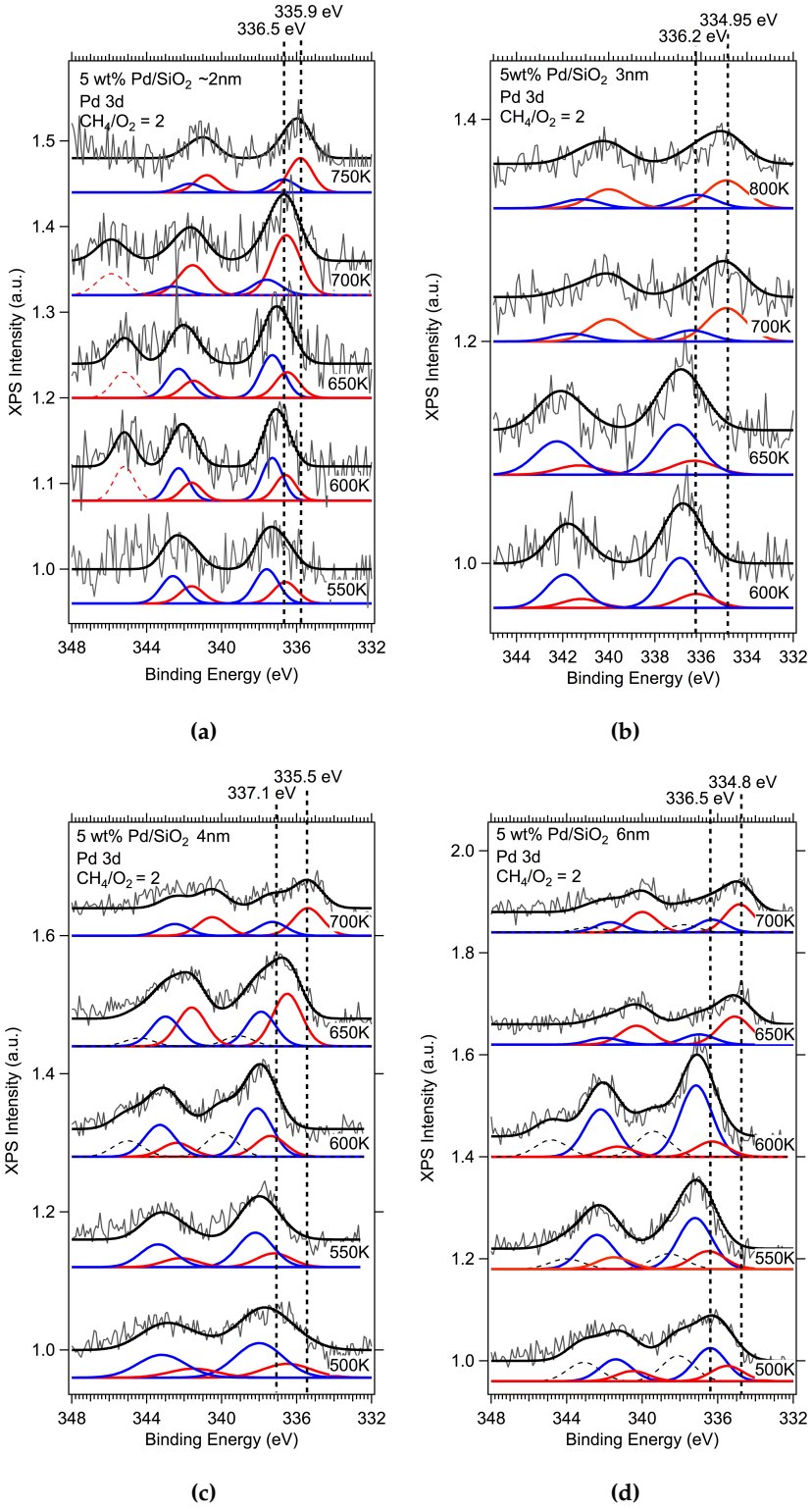

Figure 5.5: NAP-XPS: Pd/SiO_2 nanoparticles, mean crystallite size ranging from 2 – 6 nm. Pd 3d region at $h\nu$ = 650 eV, total gas pressure = 0.33 mbar ($[CH_4]/[O_2] = 2$). Raw data represented by dotted lines, data fits represented by solid lines. Dashed vertical lines represent the highest and lowest binding energies of the PdO_x peaks within each sample. Differences between these energies are plotted in Figure 5.6b.

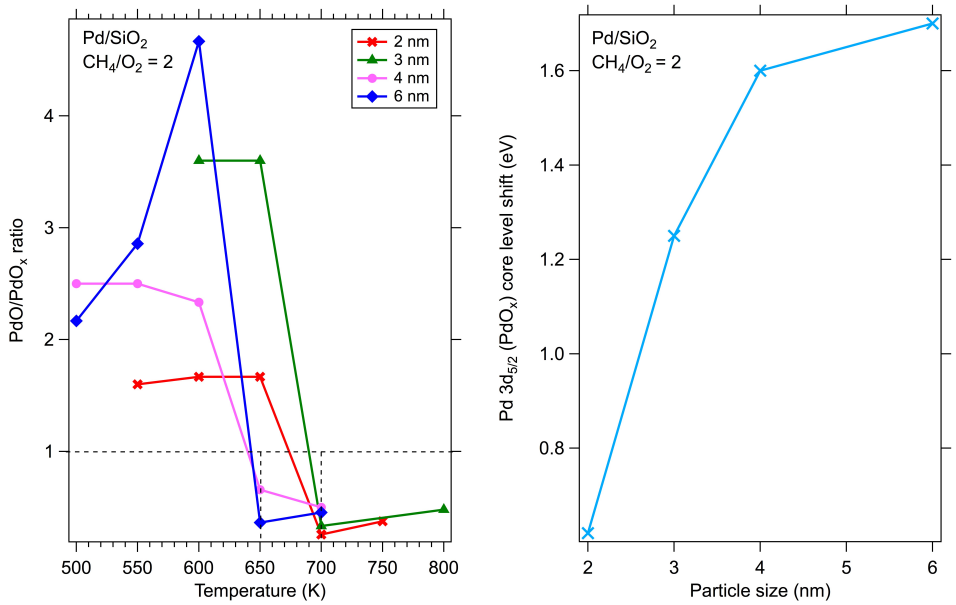

(a) **(b)**

Figure 5.6: (a) Ratio of PdO/PdO$_x$ peak areas in the Pd 3d$_{5/2}$ region from NAP-XP spectra shown in Figure 5.5 vs sample temperature for each particle size. Points beneath dashed horizontal line are when Pd is reduced, dashed vertical lines show temperature at which each catalyst becomes reduced. (b) Binding energy difference between highest energy PdO$_x$ peak and lowest energy PdO$_x$ peak in NAP-XP spectra from Figure 5.5 (see vertical dashed lines) versus particle size.

The peak areas of the Pd 3d$_{5/2}$ PdO and PdO$_x$ fits in Figure 5.5 were determined, and the peak area ratio of PdO to PdO$_x$ was calculated for each sample at each temperature. In Figure 5.6a, these PdO/PdO$_x$ ratios are shown as a function of sample temperature. PdO/PdO$_x$ values less than 1 suggest the Pd is in a predominately reduced state. The temperature at which the PdO/PdO$_x$ ratio changes from $>$1 (PdO) to $<$1 (PdO$_x$) appears to be dependent on Pd particle size. The vertical dotted lines on Figure 5.6a show this reduction temperature for each catalyst, which happens to be lower for larger nanoparticles ($\geq$4 nm, 700 K) and higher for smaller nanoparticles ($\leq$3 nm, 650 K). The PdO is most likely reduced by dissociated CH$_4$ binding to the surface in a Mars-van Krevelen mechanism [24], and it appears that this effect occurs more readily with larger Pd nanoparticles.

As well as the Pd phase change and an overall binding energy shift of the Pd 3d$_{5/2}$ peak, we also observe a binding energy shift within the Pd 3d$_{5/2}$ peak. The fitted PdO$_x$ and PdO peaks also shift during the reaction. The difference in binding energy between the highest and lowest binding energy position is plotted as a function of particle size in Figure 5.6b and it is clear that a larger shift occurs with larger particles.

Si 2p spectra taken under the same conditions are shown in Figure 5.7. The binding energy of each spectrum has been shifted with respect to the SiO_2 peak (103.3 eV), and the same ΔE applied to the corresponding Pd 3d spectrum (Figure 5.5). A linear background was subtracted after intensity normalisation. With the exception of 3 nm particles (5.7b), the signal from the silicon wafer substrate (Si^0) can be observed at 99 eV, fitted with two peaks (ΔE = 0.6 eV [221]) to account for the spin-orbit coupling of Si $2p_{3/2}$ and Si $2p_{1/2}$. The peak assigned to SiO_2 can be fitted with two main peaks; SiO_2 (Si^{4+}) and SiO (Si^{2+}) at 103.3 eV and 102.6 eV respectively. SiO_2 is the most stable oxide of silicon and so this is always the predominant oxide peak. The fitted peaks at 105 – 106 eV are represented by the dashed lines in Figures 5.7a – 5.7d are most likely native oxides of the silicon wafer, or possibly signal from different silica terminations such as siloxanes or silanols in which methane has substituted an oxygen atom [222]. There are no silicon wafer signals in Figure 5.7b, neither at 99 eV nor 106 eV, which is likely due to a thick layer of catalyst on the silicon wafer. The area under the SiO_2 fitted peak was calculated and plotted as a function of temperature for each catalyst (Figure 5.8), and there appears to be a positive correlation between peak area and temperature. This suggests that over the course of the reaction, silica particles (SiO_2) are moving towards the surface of the catalyst. There is no correlation between particle size and SiO_2 peak area, although there is a general increase of a SiO_2 species for all particle sizes.

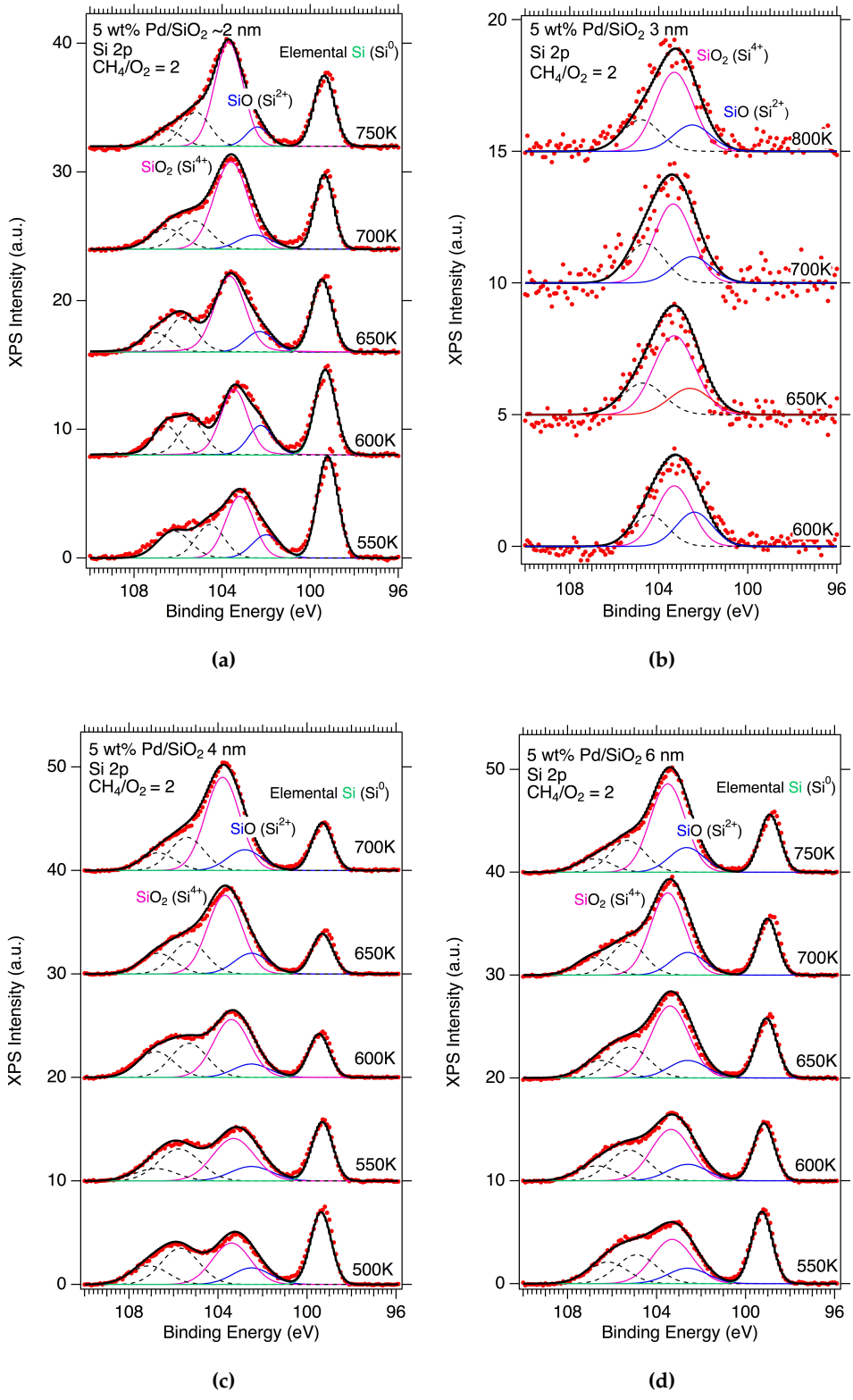

Figure 5.7: NAP-XPS: Pd/SiO_2 nanoparticles, mean crystallite size ranging from 2 – 6 nm. Si 2p region at $h\nu$ = 650 eV, total gas pressure = 0.33 mbar ($[CH_4]/[O_2] = 2$). Raw data represented by dotted lines, data fits represented by solid lines.

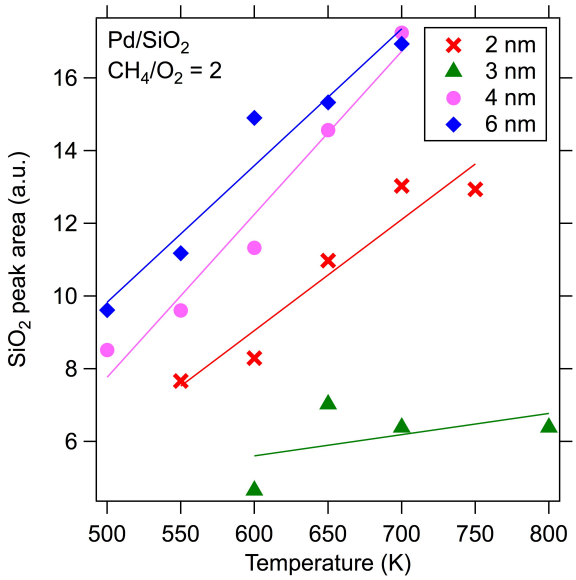

Figure 5.8: Quantification of SiO_2 species from NAP-XPS peak area calculation (SiO_2 peak at 103.3 eV in Figure 5.7), plotted as a function of sample temperature.

NAP-XP spectra taken in the C 1s region can give evidence for carbon-containing intermediates that may form on the surface during the reaction. Figure 5.9 shows the NAP-XPS data in the C 1s region for the Pd/SiO_2 catalysts at different temperatures, taken under partial methane oxidation conditions ($[CH_4]/[O_2] = 2$, total pressure = 0.33 mbar). The intensity is normalised with respect to the background and the binding energy is shifted with respect to Si 2p spectra taken with the same photon energy (400 eV). In this case under partial methane oxidation conditions, no carbon species are adsorbed on the surface of the catalyst as a function of temperature (Figure 5.9). The spectra taken at 500 K show some degree of carbon contamination, shown by the peaks at 286 eV. However for all catalysts, with increasing temperatures, this species desorbs. The species at 286 eV is also indicative of surface-bound CO_2 (286.3 eV [223]) and so it is possible there is some CO_2 adsorbed on the surface before desorption into the gas phase, although this is not distinguishable from the contaminant carbon. In Figure 5.10a, the C 1s spectra for the 6 nm catalyst show a growing peak at 291.6 eV at and above 750 K. This is gas phase CO and CO_2 produced from the catalytic reaction. The area of this peak at 291.6 eV is plotted in Figure 5.10b as well as the area of the peak at 286 eV. Figure 5.10b shows the decline of the contaminant carbon and the surface-bound CO_2 (286 eV) and how the products in the gas phase increase at higher temperatures. The C 1s spectra for the other particle sizes do not show any differences in carbon signal as a function of temperature.

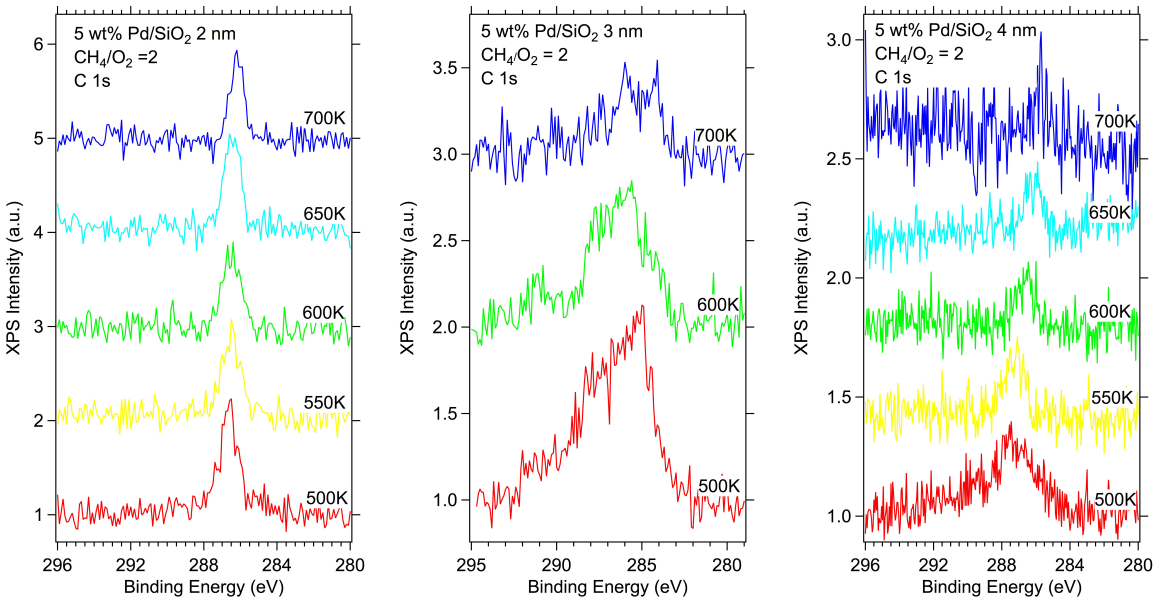

Figure 5.9: NAP-XPS data in the C 1s region for Pd/SiO_2 catalyst with d = 2 nm (a), d = 3 nm (b) and d = 4 nm (c) at different temperatures. C 1s region at $h\nu$ = 400 eV, total gas pressure 0.33 mbar ($[CH_4]/[O_2] = 2$).

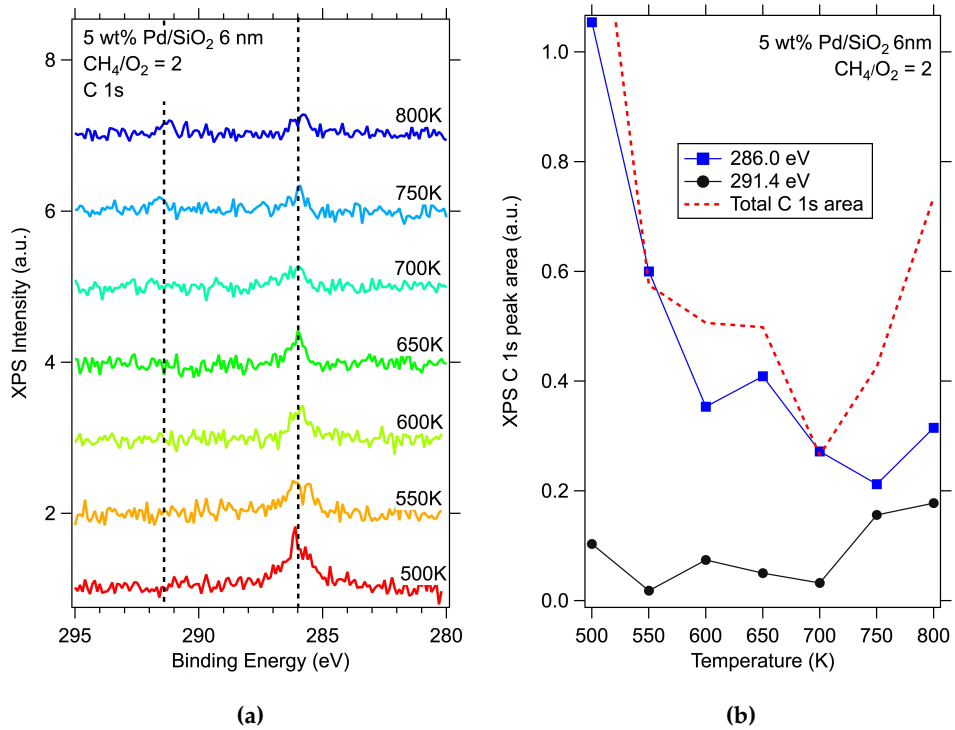

Figure 5.10: (a) NAP-XPS data in the C 1s region for Pd/SiO_2 catalyst with d = 6 nm for the temperature range 500 – 800 K. $h\nu$ = 400 eV, total gas pressure 0.33 mbar ($[CH_4]/[O_2] = 2$). (b) Areas of peaks at 286.0 eV, 291.4 eV (dotted lines on Figure 5.10a) and total area of the C 1s region as a function of temperature for Pd/SiO_2 catalyst with d = 6 nm.

5.3.2 Gas Phase Analysis

The NAP-XPS data in the Pd 3d, Si 2p and C 1s regions provide a novel and useful insight into how the chemical state of the catalyst changes as a function of temperature under ambient pressures of methane and oxygen. However, these spectra alone do not verify that the catalytic reaction is actually taking place. In order to validate whether the catalysts are active, gas phase spectra can be collected. The sample is retracted a few millimetres away from the analyser and so the gas phase in front of the sample is ionised and the photoelectrons reach the analyser cone. With this set-up, it is possible to detect molecules that may not be visible on the surface of the sample because the higher concentration is in the gas phase after desorption from the active sites.

Figure 5.11 shows the NAP-XPS in the C 1s (Figure 5.11a) and O 1s (Figure 5.11b) regions, taken with the 4 nm sample retracted away from the analyser. For comparison, the spectra in the same regions taken with the sample directly in front of the analyser in the usual NAP-XPS position are shown on the figure in dashed lines. In the case of Figure 5.11a, the spectra taken of the sample surface at this scale are flat, suggesting no significant amount of carbon species on the surface. However, when the sample is retracted away from the analyser (solid lines), the spectral lines show peaks with a relatively high intensity. The C 1s spectra are dominated by the peak at 284.5 eV, which is indicative of a reduced carbon species. Based on the fact that is the only peak present at low temperatures and that the intensity of this peak appears to decrease with temperature, we assign this peak to CH_4. At 650 K, a peak starts to appear at 291.2 eV. With a binding energy 7 eV higher than that of methane, it can be assumed this is a highly oxidised carbon species and so is assigned to CO_2. The partial pressure of CO_2 is also increasing in the mass spectra (Figure 5.13c) at this temperature. At 700 K, the partial pressure of CO exceeds that of CO_2 in Figure 5.13c, in addition to the appearance of an XPS peak at 289.7 eV. This can therefore be assigned to CO [224]. The literature tells us that the complete oxidation of methane to CO_2 has a significantly lower standard heat of formation (–802 $kJmol^{-1}$) than the partial oxidation of methane to syngas (–35 $kJmol^{-1}$) [225], and therefore CO_2 formation would occur at a lower temperature than CO formation. This is in agreement with the mass spectra in Figure 5.13c and these XP spectra, as the CO_2 peak appears before the CO peak in Figure 5.11a. Overall, the appearance of the CO and CO_2 peaks at elevated temperatures are indicators that a methane oxidation reaction is taking place. Likewise in the O 1s spectra in Figure 5.11b, CO and CO_2 peaks are observed at 537.7 eV and 536.2 eV respectively [224]. There is also another peak at 535 eV which starts to appear at 650 K, at the same temperature as the CO_2 peak.

This can be assigned to H_2O, another product of complete methane oxidation, whose partial pressure increases in the mass spectrum around this temperature also. The intensity between 529 – 534 eV, in both the gas phase spectra and the surface spectra, is likely due to a mixture of oxides coming from both the silica support and the PdO, but the large dominating peak at 539 eV at 500 K is indicative of gas phase oxygen. This assignment is further validated by how it diminishes with increasing temperature (Figure 5.11d), suggesting it is being used in the reaction. Figures 5.11c and 5.11d show that both reactant gases, O_2 and CH_4, are being used up in the reaction, as the areas of both these peaks in the NAP-XP O 1s and C 1s spectra respectively decrease with time and temperature. Meanwhile, the peaks corresponding to the oxidation products (CO, CO_2 and H_2O) in both spectra are rising in intensity, suggesting products are being formed and can be identified with NAP-XPS of the gas phase.

The asymmetry towards the higher binding energy side of the peaks at 284.5 eV in the C 1s spectra (Figure 5.11a) may either suggest a carbon-containing species is forming as a result of methane fragmentation or decomposition, in addition to the expected products, or due to vibrational broadening of the C-H bond (ν(C-H) $\approx 3200\ cm^{-1}$, 0.4 eV).

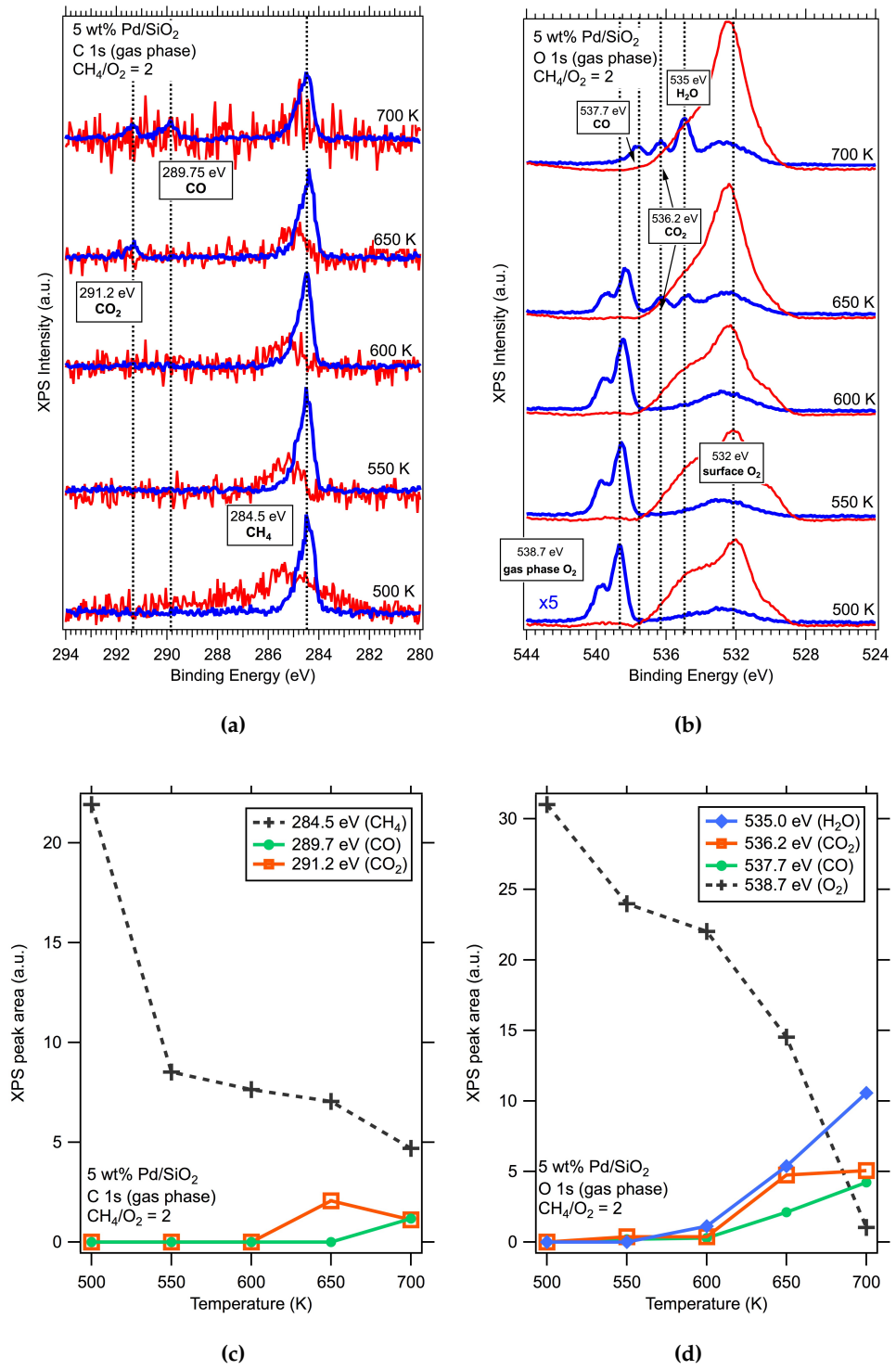

Figure 5.11: Gas phase NAP-XPS data for 5 wt% Pd/SiO_2 (4 nm) catalyst under partial oxidation of methane conditions ($[CH_4]/[O_2] = 2$) in the C 1s (a) and O 1s (b) regions. The dashed lines are the spectra taken with the sample taken directly in front of the analyser, for comparison. (c) and (d) show the peak areas corresponding to each species within the C 1s and O 1s spectra respectively as a function of temperature.

In addition to the NAP-XPS data, the catalyst activity was monitored in-situ by mass spectrometry. A quadrupole mass spectrometer is situated in between the analyser cone and the second differential pumping stage, which can identify products and reactants as they are pumped through the nozzle. The mass spectrometer was set up to detect masses 2 (H_2), 16 (CH_4), 18 (H_2O), 28 (CO), 32 (O_2) and 44 (CO_2) as the main molecules of interest. Masses 29 (CHO) and 31 (CH_3O) were also recorded to check for any methanol formation, although the partial pressures detected for both of these masses were negligible. The mass spectrometer was recording throughout the experiment, and so have information about the gas composition during NAP-XPS data collection is obtained, as well as during a slow, controlled cooling of the sample after the NAP-XPS experiment. Mass spectrometry showed the partial pressures of each gas increased on heating, and stabilised with stable temperature throughout the NAP-XPS acquisition after a slight dip in pressure, as illustrated in Figure 5.12. The data are not corrected for sensitivity.

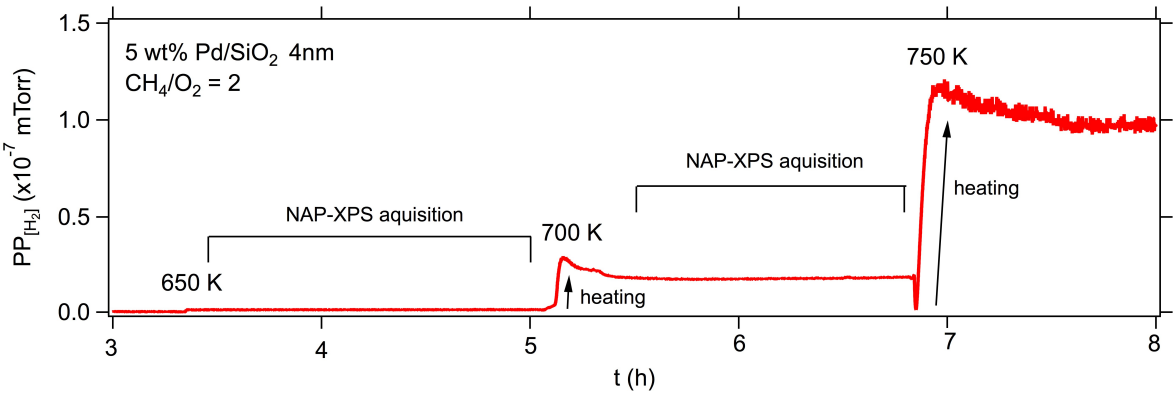

Figure 5.12: Raw mass spectrometry data. H_2 production by a Pd/SiO_2 4 nm catalyst under partial methane oxidation conditions as a function of time.

The percentage conversion for each gas is calculated with respect to methane pressure at 350 K and plotted as a function of temperature for both heating and cooling of the catalyst (Figure 5.13). The Pd/SiO_2 2 nm catalyst is not included here, as the mass spectrometer had reached saturation for masses 16 and 32. Instead, the partial pressures of the products are normalised to 1 and plotted as a function of temperature (heating and cooling separately) in Figure 5.14.

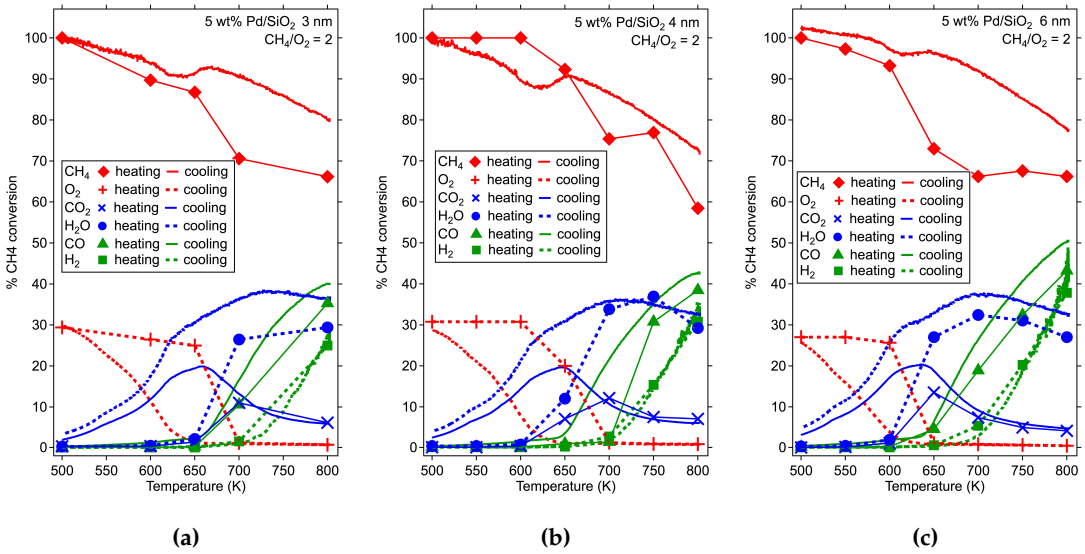

Figure 5.13: % CH_4 conversion of reactant and product gases calculated from partial pressures recorded from mass spectrometer in NAP-XPS chamber for Pd/SiO_2 3 nm (a), Pd/SiO_2 4 nm (b) and Pd/SiO_2 6 nm (c)

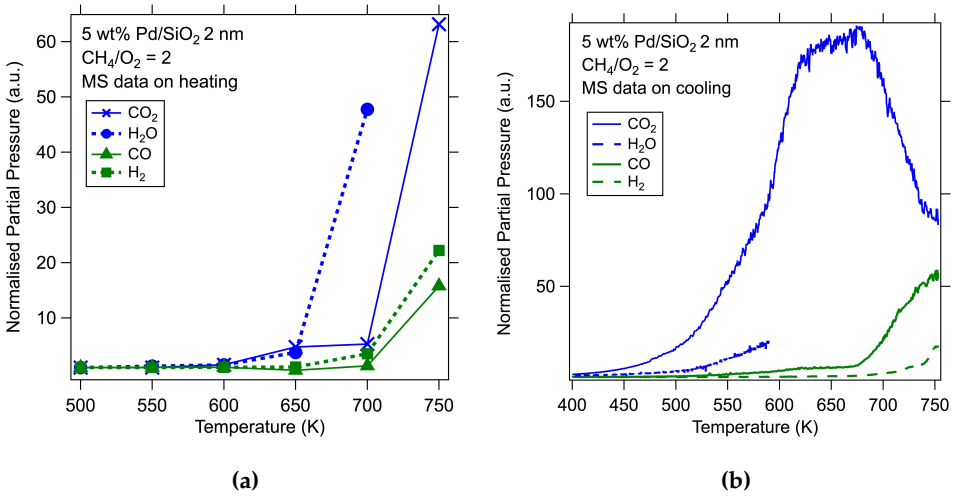

Figure 5.14: Normalised partial pressures of products using a Pd/SiO_2 catalyst with a mean Pd particle diameter of 2 nm. Figure (a) shows the product formation during an ascending temperature ramp, and (b) shows the product formation during a descending temperature ramp.

The percentage methane conversion to CO, for example, in Figure 5.13 is calculated by Equation 5.8:

$$\%\ Conv(CO)_T = \frac{partial\ pressure\ of\ CO\ at\ T}{partial\ pressure\ of\ CH_4\ at\ 350\ K} \times 100 \tag{5.8}$$

where T is each temperature of the catalyst and the partial pressure of CH_4 at 350 K is the point at the start of the reaction where no conversion is observed. Despite only seeing around 40% conversion of methane, there is a significant increase in concentrations of both complete combustion products, CO_2 and H_2O, CO and H_2. There is a hysteresis between the heating curves and the cooling curves, likely due to catalyst ageing and differences in heating and cooling rates, although after cooling to room temperature all gases return to the original concentrations. The mass spectrometry data are consistent with the gas phase NAP-XPS data in Figure 5.11, in which CO_2 and H_2O are observed at lower temperatures than CO. Both heating and cooling curves exhibit the trend that shows CO_2 and H_2O, the complete oxidation products, appear as the initial products formed. The % conversion to these products, during both heating and cooling, tails off at a similar temperature to when the corresponding partial oxidation products begin to form; CO and H_2 respectively. The formation of syngas can be correlated to the Pd 3d NAP-XP spectra in Figure 5.5. At temperatures below 600 K, where CO_2 and H_2O are the main products, the Pd is mostly oxidised. However as the temperature increases and the Pd reduces, as shown by a dominance of the lower binding energy fitted peak, methane conversion to syngas begins and increases. This would suggest that more reduced Pd is required for syngas formation, and is more evidence for the Mars-van Krevelen mechanism, whereby the rate determining step for syngas formation is the reduction of PdO [24].

5.4 Discussion and Conclusions

5.4.1 Activation Energy

Cooling of the catalyst at a constant rate yields a continuous partial pressure curve that can be plotted as a log plot as a function of the inverse temperature. Using the natural logarithm form of the Arrhenius equation (Equation 5.9), the activation energy (E_a) of each product can be determined from the slope of the curve:

$$\ln(P) = \text{const.} - \frac{E_a}{R}\left(\frac{1}{T}\right) \tag{5.9}$$

where P is the partial pressure, R is the gas constant (8.314 J mol^{-1} K^{-1}) and T is the temperature of the catalyst. Figures 5.15 and 5.16 show the Arrhenius plots of each of the complete oxidation and partial oxidation products respectively. The activation energies for each product are plotted as a function of particle size in Figure 5.17 and the possible competing reactions, in order of the temperature they occur, are outlined below:

$$\mathrm{CH_4} + 2\,\mathrm{O_2} \longrightarrow \mathrm{CO_2} + 2\,\mathrm{H_2O} \qquad (E_a = 40 - 50\ \mathrm{kJmol^{-1}}, 510 - 625\ \mathrm{K}) \tag{5.10}$$

$$\mathrm{CH_4} + \frac{3}{2}\,\mathrm{O_2} \longrightarrow \mathrm{CO} + 2\,\mathrm{H_2O} \qquad (E_a = 30 - 35\ \mathrm{kJmol^{-1}}, 510 - 625\ \mathrm{K}) \tag{5.11}$$

$$\mathrm{CH_4} + \frac{1}{2}\,\mathrm{O_2} \longrightarrow \mathrm{CO} + \mathrm{H_2} \qquad (E_a = 160 - 180\ \mathrm{kJmol^{-1}}, 625 - 750\ \mathrm{K}) \tag{5.12}$$

$$\mathrm{CO_2} + \mathrm{H_2} \longrightarrow \mathrm{CO} + \mathrm{H_2O} \qquad (E_a = 11 - 14\ \mathrm{kJmol^{-1}}, 625 - 715\ \mathrm{K}) \tag{5.13}$$

There is no significant difference in the activation energy for the same product between different particle sizes. Syngas, H_2 and CO, has a much higher activation energies than complete oxidation products, CO_2 and H_2O, that form at a lower temperature (Reaction (5.10)). CO appears to form at two different temperature ranges; 510 – 625 K and 625 – 750 K. The lower temperature range has a much lower activation energy, similar to that of CO_2 and H_2O formation which also occur at this temperature. Reactions (5.11) and (5.12) show how CO can be produced in two different reactions; the former a partial oxidation reaction forming syngas, and the latter the Water-Gas Shift (WGS) reaction where a slight excess of oxygen is used to produce H_2O and CO. The formation of CO at lower temperatures is attributed to Reaction (5.13), in addition to the instability and subsequent cracking of CO_2 in the mass spectrometer (Figure 5.16b). Although the partial pressure of H_2O eventually diminishes, it does not fall significantly.

It is possible that a small concentration of newly formed H_2 in the partial oxidation of methane reaction (Reaction (5.12)) reacts with CO_2 to form H_2O as in WGS (Reaction (5.13)). The dominating reaction at this temperature (625 – 750 K) is the partial oxidation of methane (Reaction (5.12)), and so only the high activation energy for CO formation is seen in Figure 5.16b. The H_2O produced in the WGS reaction is evident in Figure 5.15a. The values for E_a and error bars in Figure 5.17 are stated in Table 5.3.

H_2		CO			H_2O			CO_2	
d (nm)	E_a (kJ mol^{-1})	d (nm)	E_a (kJ mol^{-1})		d (nm)	E_a (kJ mol^{-1})		d (nm)	E_a (kJ mol^{-1})
2	187.9	2	31.5*	162.3	2	-	46.4	2	48.8
3	175.4	3	34.0*	158.1	3	11.1**	40.8	3	43.5
4	180.2	4	33.3*	160.0	4	11.8**	40.9	4	42.2
6	181.0	6	33.1*	170.9	6	14.0**	40.1	6	40.6
	error = $\pm$ 8.18		error = $\pm$ 6.16			error = $\pm$ 3.22			error = $\pm$ 4.55

Table 5.3: Calculated activation energies (E_a) for the formation of each methane oxidation product for each Pd/SiO_2 catalyst with mean particle size d and error calculated from straight line plot.

*CO formed as in Reaction (5.11) and from cracking of CO_2

**H_2O formed in WGS reaction (Reaction (5.13))

The reported values of activation energy for methane oxidation are not consistent, and depend heavily on the catalyst and reaction conditions. Venezia et al. reported that a Pd/SiO_2 catalyst gave an activation energy of 86 kJmol^{-1} under complete oxidation conditions [226], whilst others calculate the activation energy of Pd supported on a zeolite to be 131 – 169 kJmol^{-1} [227]. However, the activation energies reported here for complete oxidation (Reactions (5.10) and (5.11)) are in good agreement with Otto [228], who reported activation energies with a Pt catalyst between 26 – 36 kJmol^{-1} depending on Pt loading. Raj and co-workers reported an activation energy of partial methane oxidation to syngas with a palladium catalyst to be 162 kJmol^{-1} [229], which agrees with the data presented here for partial oxidation. Au-Yeung et al. state that the activation energy for methane oxidation is 176 kJmol^{-1} [230], which Zhang et al. attribute to oxidation on metallic Pd and not the oxide phase [231]. This also agrees with the activation energies obtained here for syngas formation on metallic Pd.

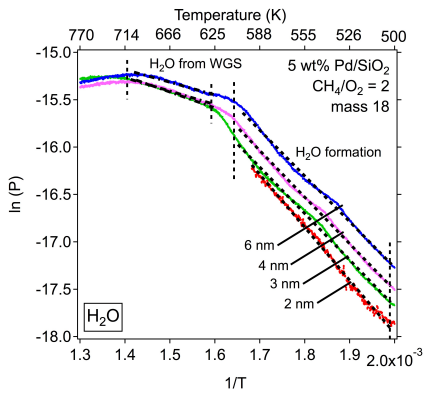

(a) H_2O (mass 18)

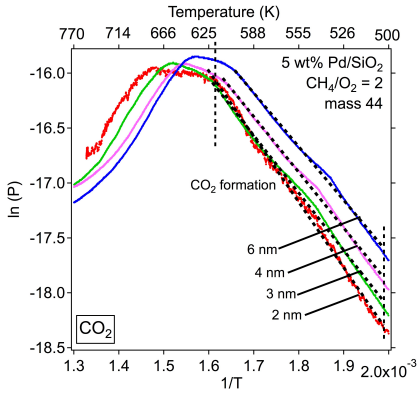

(b) CO_2 (mass 44)

Figure 5.15: Arrhenius plots of the onset temperatures of complete methane oxidation products from mass spectrometry determined partial pressures.

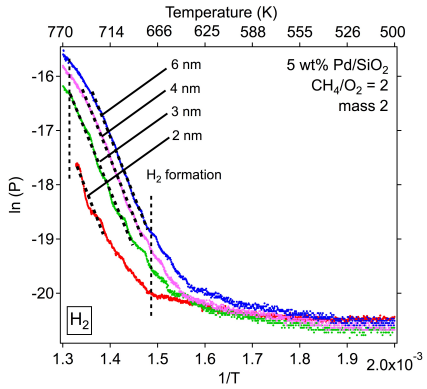

(a) H_2 (mass 2)

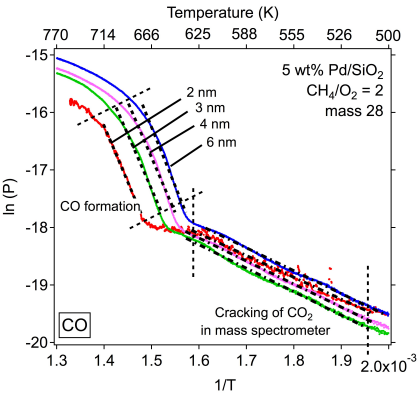

(b) CO (mass 28)

Figure 5.16: Arrhenius plots of the onset temperatures of partial methane oxidation products from mass spectrometry determined partial pressures.

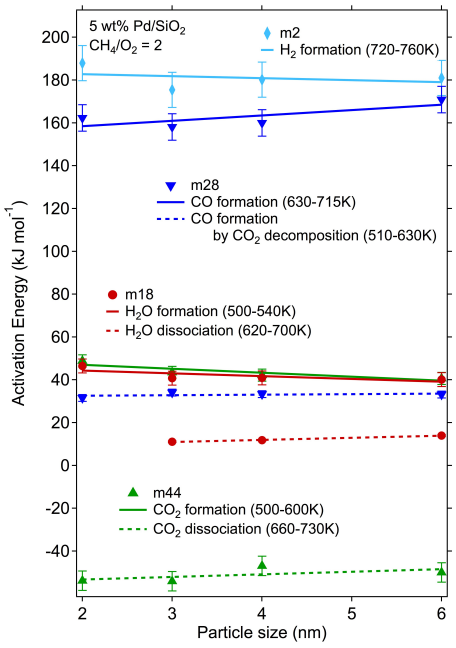

Figure 5.17: Activation energies for the formation of each product for each catalyst, determined by the - $\frac{E_a}{R}$ value from Figures 5.15 and 5.16. Fitted with a linear line and error bars dependent on the fit line.

5.4.2 Particle Size Effects

The relative activity of the catalysts towards syngas production can be determined by plotting the onset temperatures of CO and hydrogen, as shown in Figure 5.18. Figure 5.18 shows the onset temperature of syngas for each particle size. The plot shows that the catalysts with a higher mean particle diameter have a higher activity, or a lower onset temperature of CO and H_2. In addition, Figure 5.18 shows the temperatures at 20% methane conversion to syngas for catalysts with a mean Pd particle diameter ≥ 3. There is no CH_4 data available for the catalyst with 2 nm particles and so this sample is not included. However, the same trend is observed: an increase in particle diameter renders a lower temperature at which 20% methane conversion to syngas is achieved, indicating a more active catalyst. The dashed lines on the figure are the reverse reaction, in which the catalyst was cooled. Again, the same trend is observed and a hysteresis can be clearly seen, suggesting the reaction is not fully reversible.

The activation energies for different products are the same for different particle sizes. However, due the difference in onset temperatures for different particle sizes, the pre-exponential factor must be dependent on particle size. The NAP-XP Pd 3d spectra and the trend plotted in Figure 5.6a show that smaller particle sizes (2 – 3 nm) reduce at higher temperatures than larger particles (4 – 6 nm). Given that the active site of the catalyst for partial oxidation of methane is reduced Pd, this suggests that the transition from PdO_x to Pd inhibits the onset of partial oxidation for smaller particles. In this case, the pre-factor to the Arrhenius equation is dependent on the number of active sites, or reduced Pd.

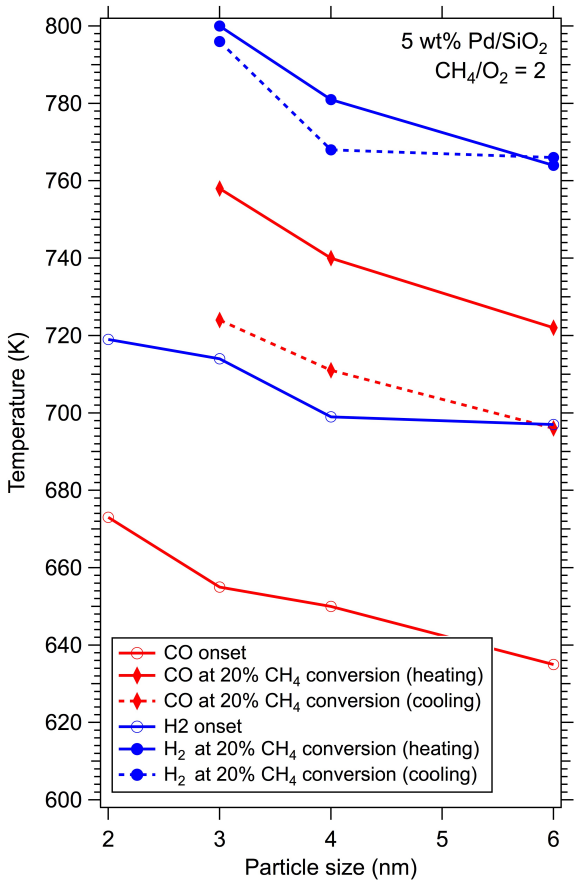

Figure 5.18: (a) Onset temperature of syngas as a function of particle size and temperature at 20% CH_4 conversion (reverse axis) to syngas as a function of particle size for catalysts with $d \geq 3$. Data shown for both heating and cooling of the catalyst. Determined from mass spectrometry data.

H_2 formation occurs at a higher temperature than CO formation for all catalysts. The high activation energy of H_2 calculated by the Arrhenius plot (Figures 5.16 and 5.17) reflects this, and is also in line with the data in Figure 5.13, which show that the slowing and decrease of CO_2 production occurs at a lower temperature than that of H_2O. The onset temperatures of syngas also coincide with the NAP-XPS data in Figure 6.3, which show the switch from a PdO species in excess to a PdO_x species dominating. The temperature at which this oxidation state change occurs decreases with increasing particle diameter and also matches the temperature at which CO is detected by the mass spectrometer. Thus, it would appear the complete oxidation reaction occurs on a more oxidised surface and the partial oxidation reaction occurs on a more reduced surface.

No catalysts with an average Pd particle diameter above 6 nm were tested in this way, and so it is not possible to say with confidence that the trend of increasing activity with increasing particle size

will continue. Despite a decrease in surface area with larger particles, it has been reported that catalytic activity and selectivity of Pd nanoparticles increases with increasing particle size up to 20 nm [64, 65, 186, 232]. However, on polycrystalline Pd foil under complete oxidation conditions, CO_2 production occurs ~150 K higher than for Pd/Al_2O_3 nanoparticles with an average particle diameter of 10 nm [65]. This suggests that a maximum is reached >6 nm, and so a bell-like curve would be expected.

5.4.3 Metal-Support Interactions

The interaction between the metal and the support material is widely considered to be a factor influencing the activity of a catalyst and has been a topic of consideration for decades [233–235]. There are still many open questions regarding the nature of the metal-support interaction, although it is generally agreed that a stronger metal-support interaction of a non-transition metal-oxide-supported catalyst has a deactivation effect due to sintering, encapsulation or interdiffusion [200, 236, 237]. Strong metal-support interactions can be induced by high temperatures and reducing atmospheres. In addition, metal particle size can also play a role in the extent of metal-support interaction. Both Müller et al. and Hicks et al. have reported separately that larger metal particles (up to 15 nm) show a weaker influence from the support material, and therefore larger particles may exhibit a higher catalytic activity [40, 238].

Zhu et al. discussed that migration of oxidised silicon and Pd nanoparticles deactivates the catalyst by blocking active sites, hence affecting the reactivity of silica-supported catalysts. They hypothesise that a combination of high reaction temperature (600 K) and the presence of water, a product of methane oxidation, aids the silicon particles to further oxidise and spread over the Pd nanoparticles [199]. Understanding this process is vital for understanding the nature of the metal-support interactions and whether they affect the activity of the catalyst. Others have reported different findings, in which palladium silicides such as Pd_2Si [214], Pd_3Si [216] and Pd_4Si [239] were found on the surface of the catalyst after treatment with hydrogen at high temperatures (>723 K). Juszczyk and Karpinski report that these intermetallic species are formed by Pd atoms filling the oxygen vacancies of the silica support [215, 216]. Lamber and co-workers suggest that it is the silanol groups (Si-OH) that enable migration by coalescence, rather than diffusion, and that the presence of this reduced silica facilitates the intermetallic compound formation [214]. In some cases [216], this is not detrimental to the catalyst's activity and can even enhance certain reactions, if not necessarily the desired reaction. Silicon migration has also been seen to occur under reducing conditions at lower temperatures (573 K) by Crozier and co-workers, who used in-situ

electron microscopy to discover silica overlayers on the PdO surface [240]. It appears that under a variety of conditions the mobility of both reduced and oxidised silicon is facilitated by hydrogen or water. Both hydrogen and water are products of methane oxidation and are therefore present in the reaction vessel. According to the gas phase NAP-XP spectra and mass spectrometry data in Figures 6.6 and 5.13 respectively, H_2O is produced in reasonably high quantities at temperatures as low as 600 K. Significant amounts of H_2 are not produced below $\sim$ 700 K, but H_2 could still have an effect even at low pressures.

Due to an increase in inelastic scattering of the photoelectrons by gas molecules in NAP-XPS, attenuation of the signal is a common feature of NAP-XP spectra [103]. The fact that the XPS signal is attenuated by matter can be used to identify the extent of migration of silicon from the support to the PdO under high pressures. Figure 5.19 shows Pd 3d (5.19a) and Si 2p (5.19b) NAP-XP spectra of a Pd/SiO_2 catalyst taken under both ultra-high vacuum conditions and reaction conditions. Due to attenuation of the signal under high pressures, it is expected that the spectra taken under a 0.33 mbar mixture of CH_4 and O_2 would be weaker in intensity. After normalisation and subtraction of a linear background, the area under each spectrum, both under UHV and ambient-pressures, has been calculated and plotted as a function of temperature (Figure 5.20). Figure 5.20a shows that the Pd 3d XPS signal intensity is higher under UHV conditions (10^{-9} mbar) than under methane oxidation conditions (0.33 mbar). However, the opposite effect is seen for the Si 2p spectra, as shown in Figure 5.20b, in which the signal intensity is higher under 0.33 mbar of CH_4 and O_2. This is contradictory to the theory that XPS signal intensity is attenuated under higher pressures and the increase in Si 2p photoelectrons could be an indication that there is simply more silicon at the surface of the catalyst. It is clear from the Si 2p spectra in Figure 5.19b that the silicon species change under partial methane oxidation conditions. Most notably, an increase in the SiO_2 species at 103.3 eV occurs at 700 – 750 K. At these temperatures, both water and hydrogen are present in the reaction chamber and could be facilitating movement of silicon from the support material to the empty PdO sites. Interestingly, the effect appears to be reversible. Figure 5.21 shows XP spectra of the same catalyst under 0.33 mbar and UHV at 300 K post-reaction. The peak area for the spectrum taken under UHV conditions is higher than for under ambient pressures, suggesting the silicon has migrated back to the bulk on cooling.

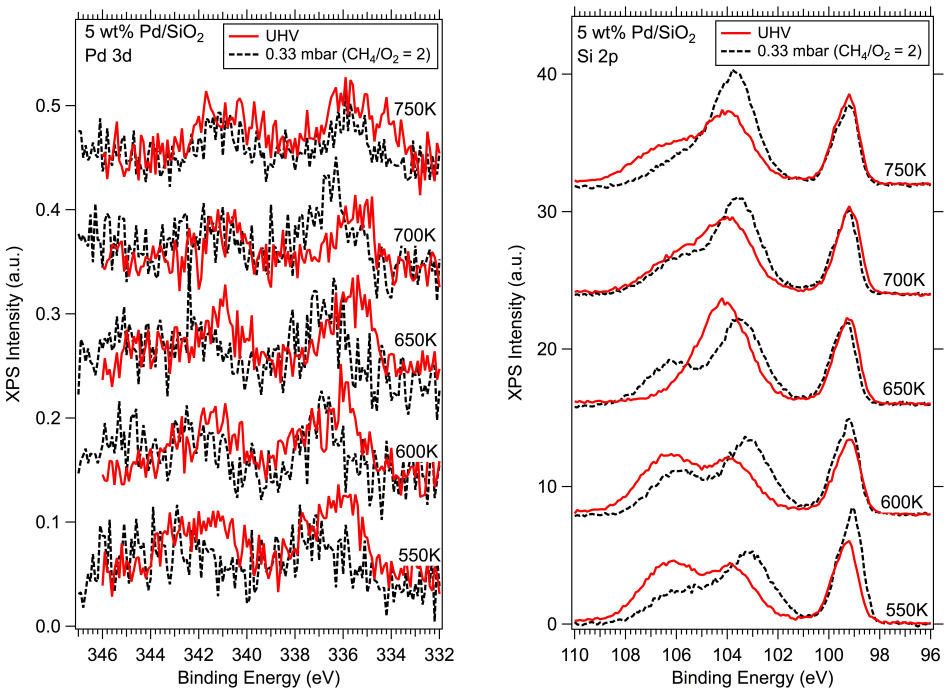

(a) **(b)**

Figure 5.19: NAP-XP spectra of Pd/SiO_2 catalyst in Pd 3d region (a) and Si 2p region (b) taken under UHV conditions (red solid lines) and partial methane oxidation conditions (black dashed lines) at a range of temperatures from 550 – 750 K. $h\nu$ = 650 eV.

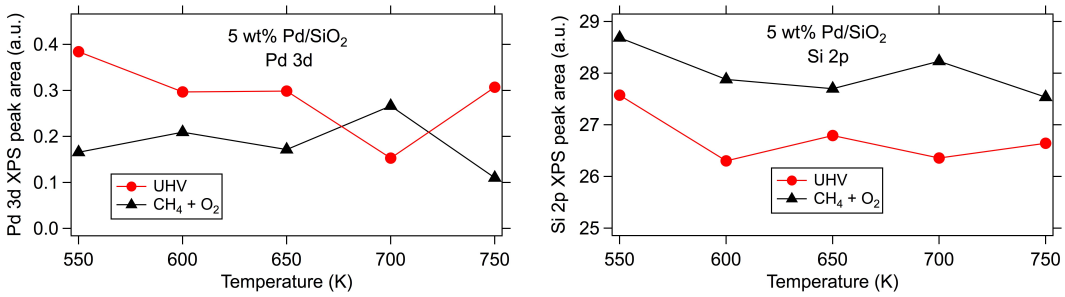

(a) **(b)**

Figure 5.20: Areas of XP spectra taken under UHV (10^{-9} mbar) and ambient pressures (CH_4/O_2 = 2, total pressure 0.33 mbar) from Figure 5.19 at different temperatures. (a) Peak areas of Pd 3d spectra from Figure 5.19a, (b) peak areas of Si 2p spectra from Figure 5.19b.

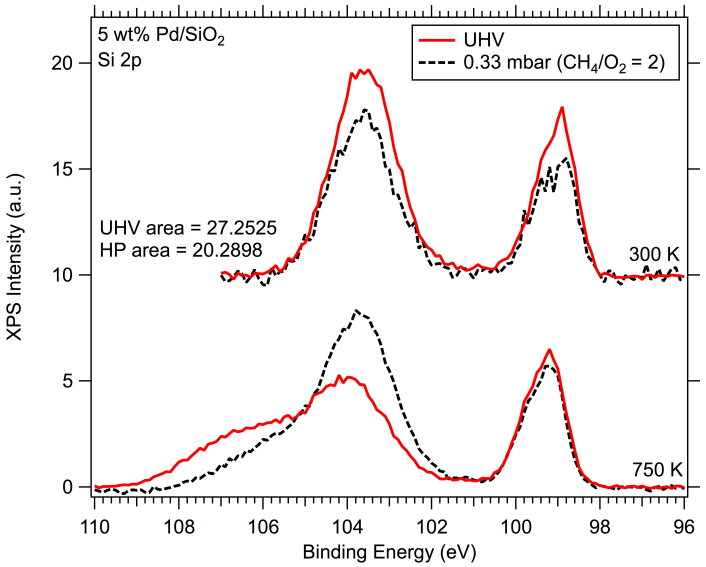

Figure 5.21: XPS data of Pd/SiO_2 catalyst in the Si 2p region under ambient pressures (black dashed lines) and UHV (red solid lines) at 750 K and 300 K (post-reaction after cooling). $h\nu$ = 650 eV.

It is difficult to know for certain if palladium silicides are formed, as the binding energy for these overlap with PdO in the Pd 3d region (336.2–336.8 eV) [241, 242] and elemental Si in the Si 2p region (99.5–100.5 eV) [243]; both of which are present in these spectra. However, it can be said with some certainty that silicon oxides are migrating to the surface due to the increase in intensity at 103.3 eV under the presence of methane, oxygen, water and hydrogen at temperatures above 700 K. Water plays a key role in catalyst deactivation [46, 210] and silicon migration [199, 244] although the mechanism by which this occurs is not yet clear.

5.5 Summary

NAP-XPS has been used to show how the surface chemistry of Pd/SiO_2 catalysts evolves during the partial oxidation of methane. Complementary mass spectrometry data provide information regarding the reaction products and are compared to the NAP-XPS data in order to identify which surface state correlates with which reaction product. In conclusion, we are able to state that, even under an oxygen-deficient atmosphere, complete combustion products (CO_2 and H_2O) are formed first and formation occurs between 600 – 650 K, according to the mass spectrometry data. At this temperature, the NAP-XP spectra show the Pd is in its oxidised form, PdO. With an increase in temperature to 700 – 750 K, the partial pressures of masses 2 and 28 increase on the mass spectra, suggesting the partial oxidation of methane has become the dominating reaction. Here, due to a negative shift in binding energy in the Pd 3d region, the NAP-XPS data confirm that the PdO is reduced to a PdO_x species where $0 \leq x < 1$. Evidence of both complete and partial oxidation products is shown in the NAP-XP spectra of the gas phase in the C 1s and O 1s regions.

A particle size effect is observed with regards to the catalyst's ability to be reduced. The reduced Pd species appears to be the dominant oxidation state at high temperatures for all catalysts, though for larger nanoparticles (4 – 6 nm) the oxidation state switch occurs 50 K lower than for smaller nanoparticles (2 – 3 nm). A particle size effect is also observed for syngas formation, for which the reduced Pd appears to be the catalytic species. Both the onset temperature of syngas and the temperature at which 20% of CH_4 is converted to syngas decrease with increasing particle size (up to 6 nm). This suggests that a larger mean diameter of the metal species renders a more active catalyst for the partial oxidation of methane, which is in agreement with a number of previous studies on methane oxidation catalysts [24, 40, 64, 65, 89]. The calculated activation energies are four-fold higher for partial oxidation than for complete oxidation under a methane rich gas feed, although no particle size effect is seen with regards to activation energies. The pre-exponential factor must therefore be dependent on particle size, the number of active sites and the nanoparticle's ability to be reduced. However, the onset temperatures for Pd/SiO_2 catalysts appear to be $\sim$50 K higher than for Pd/Al_2O_3 catalysts tested in a previous study under the same conditions [65]. A possible reason for this could be due to silicon migrating from the support material to the surface and blocking Pd active sites. An increase in SiO_2 signal intensity in the NAP-XPS Si 2p region under ambient-pressures suggest that more silicon oxides have reached the sur-

face of the catalyst. This is not seen in the Al 2p spectra of the Pd/Al_2O_3 catalyst. The mechanism is yet unclear, but it is proposed that the water and hydrogen formed in the reaction are facilitating movement of silicon to the surface. Blocking of the active sites would decrease the catalytic activity of the Pd and hence higher onset temperatures.

6 Partial Oxidation of Methane: NAP-XPS and $Pd/SiO_2–Al_2O_3$ catalyst

Abstract

Mixed $SiO_2–Al_2O_3$ powders were used as supports for Pd catalysts with pre-prepared SiO_2:Al_2O_3 ratios of 60:40, 70:30 and 80:20 in order to determine whether a combination of both alumina and silica is more reactive than the pure support. The catalysts with 60:40 and 80:20 SiO_2:Al_2O_3 supports were exposed to partial oxidation of methane conditions ([CH_4]:[O_2] = 2) and a temperature ramp up to 800 K, whilst the chemical state of the catalysts was monitored by near-ambient pressure x-ray photoelectron spectroscopy (NAP-XPS) as a function of temperature at the Advanced Light Source, Berkeley. Mass spectrometry was used in conjunction with NAP-XPS to identify the reaction products and hence determine the reactivity of each catalyst.

For both support ratios, NAP-XPS data show changes in the oxidation state of the palladium as the temperature increases, from oxidic Pd to reduced Pd, and in both cases, the Pd is fully reduced by 700 K. Likewise to catalysts with pure supports, Pd/Al_2O_3 and Pd/SiO_2, the mass spectrometry data show an increase in partial pressures of CO_2 and H_2O whilst the Pd is in the oxide phase ($\sim$550 – 600 K), followed by CO and H_2 at higher temperatures and on the reduced surface. In terms of the onset temperatures of products, the order of reactivity is SiO_2:Al_2O_3 = 60:40 > SiO_2:Al_2O_3 = 80:20 for the production of CO_2 and H_2O. The reactivity is similar for the onset of syngas (H_2 + CO), although the overall percentage conversion of methane to syngas at the end of the reaction is greater for the 60:40 catalyst.

6.1 Introduction

Traditionally, methane oxidation catalysts consist of a pure support material, such as Al_2O_3, SiO_2, ZrO_2 and TiO_2, loaded with various catalytic metals and yield high conversion rates [39, 43, 53, 245]. Silica-alumina species are found in zeolites, which can self-generate oxygen species that activate C-H bonds in methane [246]. Selective oxidation by surface oxygen from zeolites has been successful in producing methanol in the partial oxidation of methane at room temperature [247, 248].

Mixed SiO_2-Al_2O_3 is an acidic catalytic support used in the cracking of hydrocarbons and as a component in many zeolite-based catalysts. The SiO_2-Al_2O_3 is doubly functional in that it itself is responsible for the hydrocarbon cracking, whilst also serving as a support material for the hydrogenation metal [249]. Mixed silica-aluminas are usually prepared by an impregnation of Al_2O_3 with collodial silica or silicic acid [250–253]. This results in an amorphous structure with varying porosities depending on the SiO_2:Al_2O_3 ratio. Changing the SiO_2:Al_2O_3 ratio also changes the ratio of Brønsted and Lewis acid sites, which in turn alters the acidity of the surface and is related to the configuration of the free hydroxyls. A higher ratio of Brønsted acid sites to Lewis sites would lead to enhanced oxidation of methane [254]. Pure silica is predominately terminated by silanols; Si-OH moieties that exhibit little Brønsted acidity [255]. However, the addition of alumina to silica creates tetrahedrally co-ordinated Al that carries an extra proton to compensate for its negative charge [249] or bridged Si-O-Al sites. In both cases, a Brønsted acid site is created. Stabilising alumina with silica and vice versa has also been shown to improve the durability of a Pd catalyst in maintaining a high conversion of hydrocarbons in the methane oxidation reaction [256]. There are few studies reported that use a SiO_2-Al_2O_3 catalyst support for methane oxidation, but mixed silica-alumina supports have shown to exhibit high selectivities towards Fischer-Tropsch reactions, in comparison to pure aluminas and silicas and zeolites [253].

This Chapter looks to explore the surface chemistry of mixed supports under partial oxidation of methane conditions with NAP-XPS and whether the difference in surface composition of different ratios of SiO_2:Al_2O_3 has an effect on the catalytic activity.

6.2 Experimental

6.2.1 Sample Preparation

5 wt% Pd/SiO_2-Al_2O_3 catalysts were prepared from a $Pd(NO_3)_2$ precursor (Alfa-Aesar, 8.34% assay) using the same co-precipitation method as described in Chapters 4 and 5. Three different silica-alumina supports from the SIRAL range (Sasol GmbH) were used as the support material with the SiO_2:Al_2O_3 ratios: 60:40, 70:30 and 80:20. The BET surface area and pore volumes were determined by the manufacturer and are listed in Table 6.1. The catalysts were all calcined to 600°C in order to remove any contaminants or unreacted precursor, before each being spray coated onto 1 cm $\times$ 1 cm pieces of a P-doped silicon wafer in preparation for synchrotron experiments. The metal particle size of these catalysts were not determined by TEM, but calcining at 600 °C would yield particles in the range of 6 – 10 nm.

SiO_2:Al_2O_3	Surface area (m^2g^{-1})*	Pore volume (ml g^{-1})**
60:40	476	0.51
70:30	376	0.40
80:20	344	0.35

Table 6.1: Surface area and pore volume of SIRAL supports used. *Determined by BET measurements. **Determined by mercury porosimetry. [257]

The exact structure of the commercially sourced SiO_2-Al_2O_3 supports is unclear due to their amorphicity and inhomogeneity. The preparation method of the SIRAL range of silica-aluminas involves the impregnation of alumina with silicic acid and sintering to fuse them together [252].

6.2.2 Sample Characterisation

The elemental composition and metal dispersion of each Pd/SiO_2-Al_2O_3 catalyst were characterised by XPS and CO chemisorption, respectively. XPS data were collected using a Thermo Escalab 250 photoelectron spectrometer, equipped with with a monochromatised Al K-α x-ray source ($h\nu$ = 1486.6 eV). An electron flood gun was used to compensate for sample charging. High-resolution scans were recorded at room temperature and under a base pressure of 10^{-8} mbar in the Pd 3d (Figure 6.1a), Si 2p (Figure 6.1b) and Al 2p (Figure 6.1c) regions with 30 eV pass energy, and lower resolution overview scans (pass energy = 150 eV) were taken to check for impurities. The XPS data in Figure 6.1 show the Pd, Al and

Si content of each SiO_2:Al_2O_3 ratio. There is no trend with Pd content as a function of silica content, although Si content and Al content increase and decrease respectively with an increase in SiO_2 in the support material. Note that the Si 2p peak area at 60% SiO_2 is significantly lower compared to 80%, suggesting that Al_2O_3 displaces SiO_2 at the surface even with only 40% Al_2O_3 content. The peak areas for the SiO_2 peak (103.3 eV) and the Al 2p peak (74.5 eV) are shown in Table 6.2 and Figure 6.2. The peak in the Si 2p region at 99.6 eV is characteristic of elemental Si from the silicon wafer substrate, and so is not included in the peak area calculation.

A Micromeritics AutoChem II 2920 analyser was used to determine the metal surface area and metal dispersion by CO chemisorption. Pulses of CO are passed through 0.2 g of the powder sample at 299 K before ramping to 573 K at a ramp rate of 10 K/min. The adsorbed CO is measured by a thermal conductivity detector and used to calculate metal area and dispersion:

$$\text{Area of Pd} = \frac{\text{molecules of CO adsorbed}}{\text{molecules per m}^2}$$

$$\text{Pd dispersion (\%)} = \frac{N_S}{N_T} \times 100$$

where N_S and N_T are the number of surface Pd atoms measured and the total number of Pd atoms in the sample respectively [236]. The values for Pd surface area and Pd dispersion are also stated in Table 6.2.

% SiO_2	Si 2p peak area (103.3 eV)	Al 2p peak area (74.5 eV)	Pd surface area (m^2/g sample)	Pd dispersion (%)
100	39.7	0	0.868	3.895
80	34.5	316	0.231	1.036
70	6.37	383	-	-
60	1.88	400	0.291	1.306

Table 6.2: Si 2p and Al 2p peak areas obtained from ESCA data in Figure 6.1 to three significant figures. Pd surface area and Pd dispersion obtained from CO chemisorption measurements.

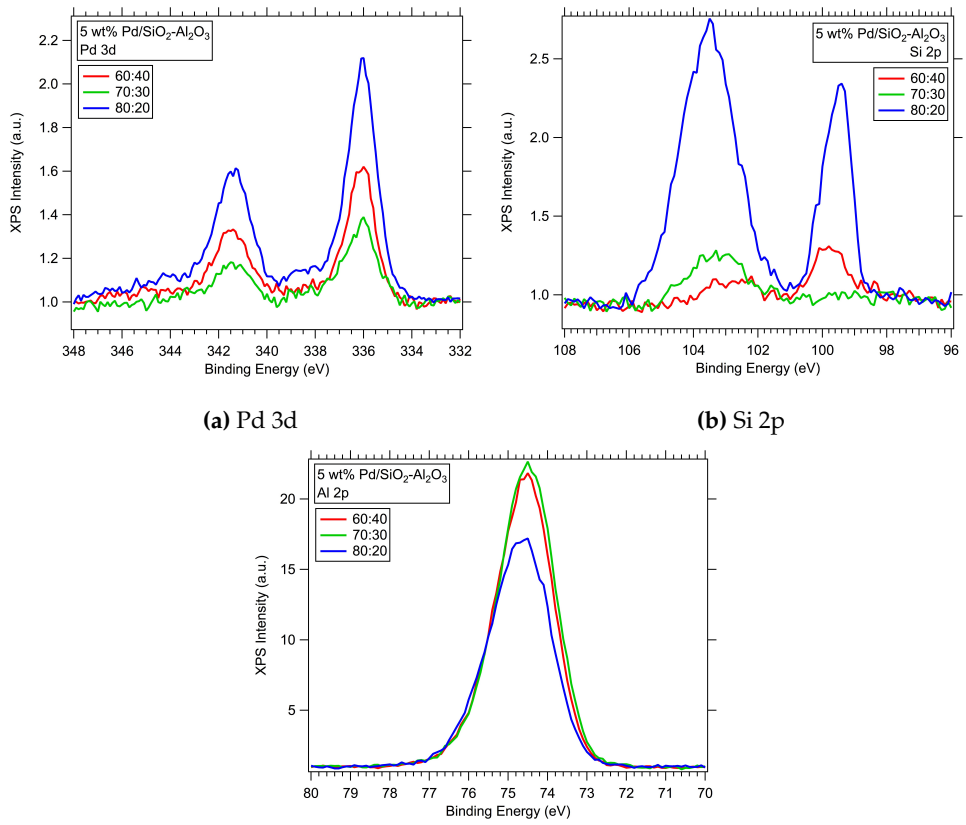

(a) Pd 3d **(b)** Si 2p

(c) Al 2p

Figure 6.1: XPS data recorded at 30 eV pass energy at $h\nu$ = 1486.6 eV in (a) Pd 3d, (b) Si 2p and (c) Al 2p regions. All spectra are normalised with respect to the background and a linear background has been subtracted.

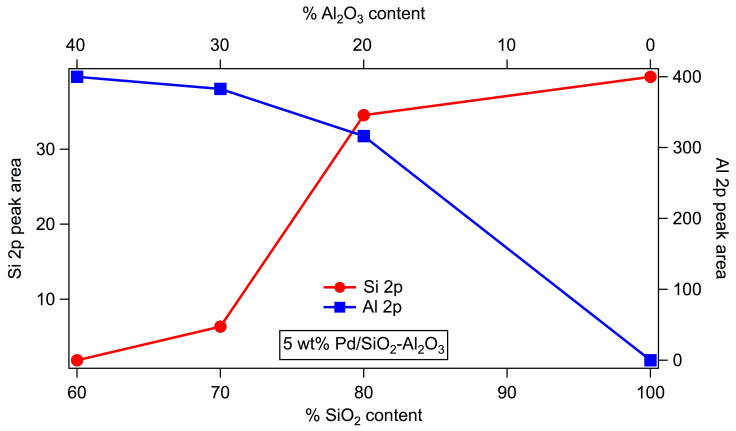

Figure 6.2: Si 2p and Al 2p peak areas obtained from ESCA data in Figure 6.1 as a function of silica content

6.2.3 Synchrotron Experiments

The Pd/SiO_2-Al_2O_3 catalysts were each spray coated onto a silicon wafer in preparation for synchrotron experiments. A thin coating enables the catalyst to stick to the substrate and a P-dopant in the wafer helps to improve the conductivity of the sample. The catalysts were studied at beam line 9.3.2 [132] at the Advanced Light Source (ALS) in Berkeley, USA, with near-ambient pressure x-ray photoelectron spectroscopy (NAP-XPS) and mass spectrometry. The 9.3.2 endstation is equipped with a Scienta 4000 HiPP analyser and a specially designed differential pumping system, with an in-built mass spectrometer, enabling pressures of up to 1 Torr in the analysis chamber. In-situ data collection including surface characterisation with NAP-XPS and quantification of the gas composition with mass spectrometry is therefore facilitated.

The catalyst samples were characterised with NAP-XPS in UHV, 10^{-9} mbar base pressure, at 450 K in order to check the degree of sample charging and that the elemental composition was as prepared. Methane and oxygen gases were leaked into the analysis chamber by leak valves and stabilised at 160 mTorr (0.22 mbar) and 80 mTorr (0.11 mbar) respectively in order to mimic the stoichiometric ratios of the partial oxidation of methane reaction. Once the pressures of the gases are stable at a combined pressure of 240 mTorr (0.33 mbar) in a 2:1 [CH_4]:[O_2] ratio, the temperature of the sample was increased to 500 K where high-resolution NAP-XPS measurements are taken in the Pd 3d, Si 2p and Al 2p regions using the same incident photon energy of $h\nu$ = 650 eV. The temperature was increased and stabilised at 50 K intervals up to 800 K, where at each temperature NAP-XP spectra in each region were recorded. Binding energies of the NAP-XP spectra were all calibrated to the literature value of the SiO_2 spectral line at 103.3 eV [242], whereby the difference in binding energy between the experimental value for the SiO_2 peak and 103.3 eV was used to shift the binding energies of the other spectra taken with the same photon energy and under the same conditions. The resulting spectra were then normalised with a linear background subtraction. Charging of the sample was minimised by the increased temperatures and addition of a dopant in the Si wafer substrate, however some artefacts of sample charging were still visible in the spectra and were accounted for using the custom fitting procedure as described in Chapter 3. Due to time constraints, only the 80:20 and 60:40 silica:alumina ratios were tested.

Throughout the NAP-XPS data acquisition, the mass spectrometer was collecting data via six channels; masses 2 (H_2), 16 (CH_4), 18 (H_2O), 28 (CO), 32 (O_2) and 44 (CO_2). The partial pressures of the

products and reactants were recorded on heating and cooling of the sample, and ultimately converted into a percentage conversion of methane by:

$$\text{Conv(CO)}_T = \frac{\text{partial pressure of CO at } T}{\text{partial pressure of CH}_4 \text{ at 350 K}} \times 100\ \%$$

Manipulating the data in this way provides a direct comparison of reactivity between samples and an insight into the temperature at which each product forms. Along with the NAP-XPS data, a picture is formed as to how the catalyst behaves at different points in the reaction with regards to temperature and gas composition. No correction factors were applied to the mass spectrometry data.

6.3 Results

Two 5 wt% Pd/SiO_2-Al_2O_3 catalysts containing either 80% or 60% SiO_2 were studied under conditions representative of the partial oxidation of methane reaction. Each catalyst, spray coated on a Si wafer substrate, was monitored during a temperature ramp from 500 – 800 K under 0.33 mbar total pressure reaction feed comprising of O_2 and CH_4 (1:2 ratio) with near-ambient pressure (NAP) XPS and mass spectrometry.

6.3.1 NAP-XPS

Near-ambient pressure x-ray photoelectron spectroscopy (NAP-XPS) at beam line 9.3.2 of the Advanced Light Source in Berkeley, USA was the primary characterisation method for monitoring the in-situ behaviour of these catalysts. Sample charging was minimised by heating the sample to 500 K and starting measurements at that temperature, although some artefacts of sample charging remain visible in the spectra including low intensity, peak splitting and peak broadening. The spectra taken in the Pd 3d region as shown in Figure 6.3 were shifted along the energy axis according to the shifts of the corresponding Al 2p spectrum taken with the same photon energy and at the same temperature. The spectra were normalised with respect to the inelastic background on the low binding energy side and a linear background was subtracted. Pd $3d_{5/2}$ and Pd $3d_{3/2}$ peaks were fitted using the custom method as described in Chapter 3.

The Pd 3d spectra (Figure 6.3) can be fitted with two features in each spin-orbit peak; a reduced Pd species at lower binding energy (335 – 336 eV), and an oxidised Pd species at higher binding energy (PdO_x, 336 – 337 eV). The spectra taken at 500 K and 600 K for the 80:20 sample (Figure 6.3a) both exhibit a feature at 338.0 – 338.8 eV, which can be assigned to higher oxidation states of Pd as a PdO_y species where $1 < y \leq 2$. This species appears to be unstable, and diminishes with increasing temperature. Both PdO_x and Pd metal are evident in both catalysts at each temperature, although the overall Pd $3d_{5/2}$ peak position shifts as a function of temperature. Figure 6.4 shows how the binding energy of the overall Pd $3d_{5/2}$ peak shifts to lower binding energy values with increased temperature, suggesting the catalysts reduce at high temperatures ($>$ 650 K). Both SiO_2:Al_2O_3 ratios exhibit a similar reduction in the oxidation state of Pd from 600 – 650 K. At 600 K, the operating temperature of complete methane oxidation, both catalysts are in an oxidised phase as expressed by the Pd $3d_{5/2}$ peak appearing at 337.0 eV

for the 60:40 catalyst and 336.7 eV for the 80:20 catalyst. At 650 K, a shift towards lower binding energy is observed for both catalysts, characteristic of a reduced Pd species. From 650 K to 800 K, the oxidation state of the Pd appears to be stable and remains predominately in a reduced state for the remainder of the temperature ramp.

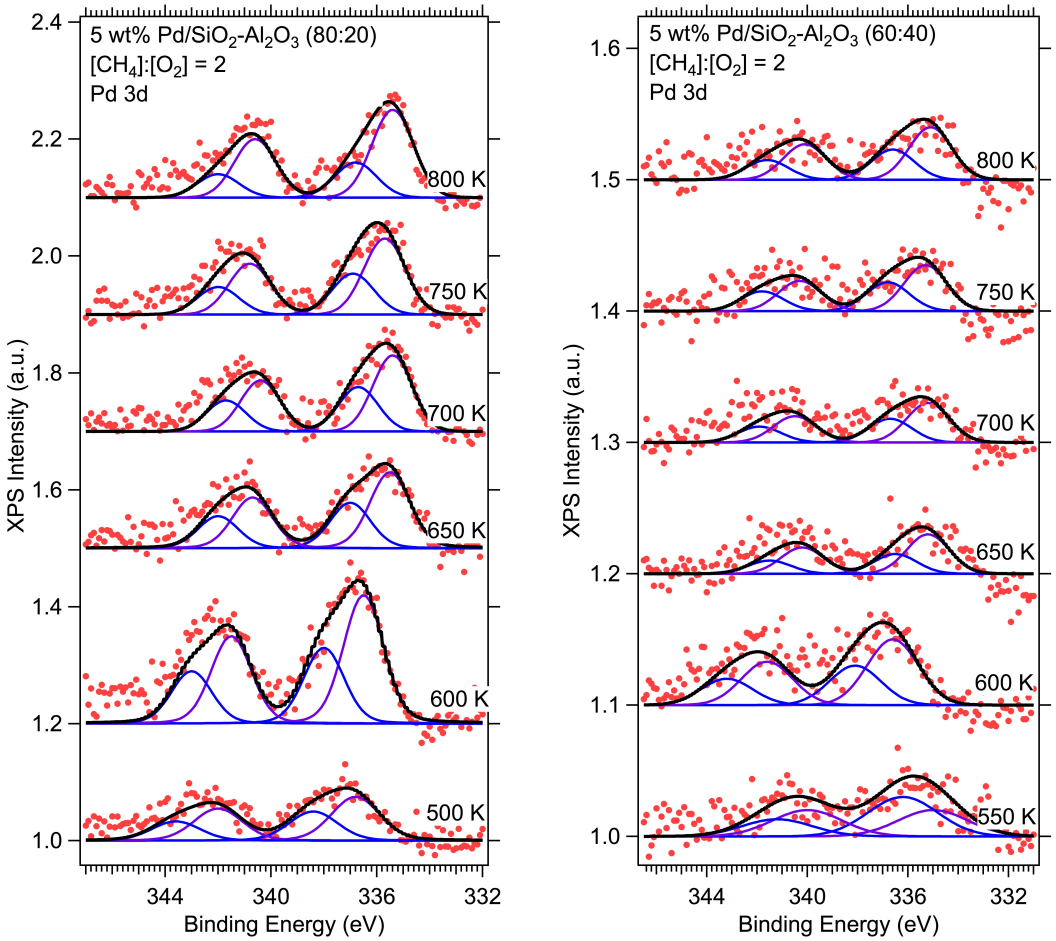

Figure 6.3: NAP-XPS data of 5 wt% Pd/SiO_2-Al_2O_3 catalysts containing either (a) 80% silica or (b) 60% silica taken at 50 K temperature intervals from 500 – 800 K under $[CH_4]$:$[O_2]$ = 2 (total pressure = 0.33 mbar), in the Pd 3d region. $h\nu$ = 650 eV, pass energy = 100 eV. Raw data are shown as red dotted lines, black lines are the overall fits. Oxidised Pd species and reduced Pd species fitted peaks are expressed as blue and purple lines respectively.

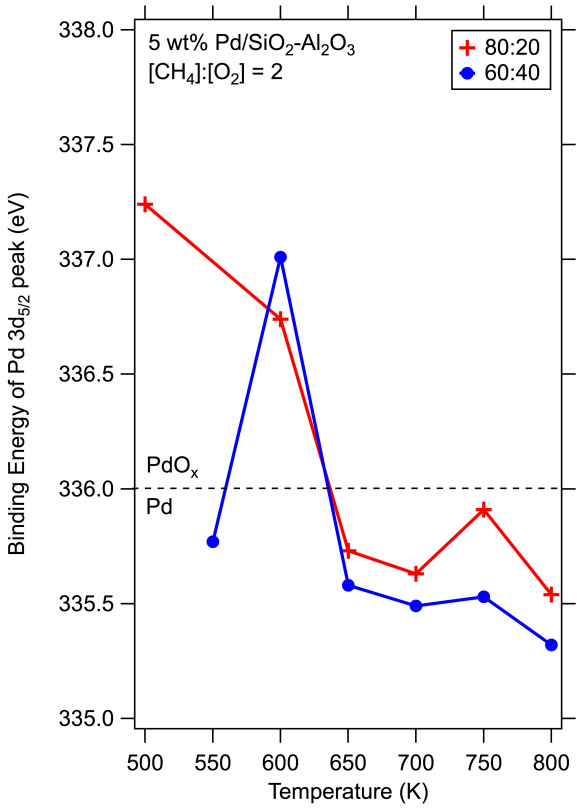

Figure 6.4: Plot of the binding energy value of the overall Pd $3d_{5/2}$ peak in the Pd 3d NAP-XP spectra from Figure 6.3 as a function of sample temperature.

Unlike the similarity in the Pd 3d spectra, the NAP-XP spectra in the Si 2p and Al 2p regions appear quite different (Figure 6.5a). The Si 2p signal at 99 – 105 eV is strong for the 80:20 catalyst and remains stable for the duration of the experiment. However, it appears that with an increased Al_2O_3 content the Si 2p signal is broadened and reduced. The 60:40 spectra in Figure 6.5a show only intensity in the Al 2p and Al 2s regions, 74.5 eV and 120 eV respectively. The lab source XPS data in Figure 6.1b also shows weak intensity in the Si 2p region under UHV conditions, and it would appear that ambient pressures and elevated temperatures do not improve Si 2p signal. The O 1s NAP-XPS shown in Figure 6.5b also differ with silica content. The 60:40 catalyst, whose Si 2p signal is weak, exhibits a broad O 1s peak that could arise from multiple surface hydroxy terminations, often seen in Al_2O_3 surfaces [258]. The O 1s signal for the 80:20 catalyst, in which SiO_2 is present at the surface, is reasonably Gaussian and symmetric in shape suggesting a more uniform and stable surface termination.

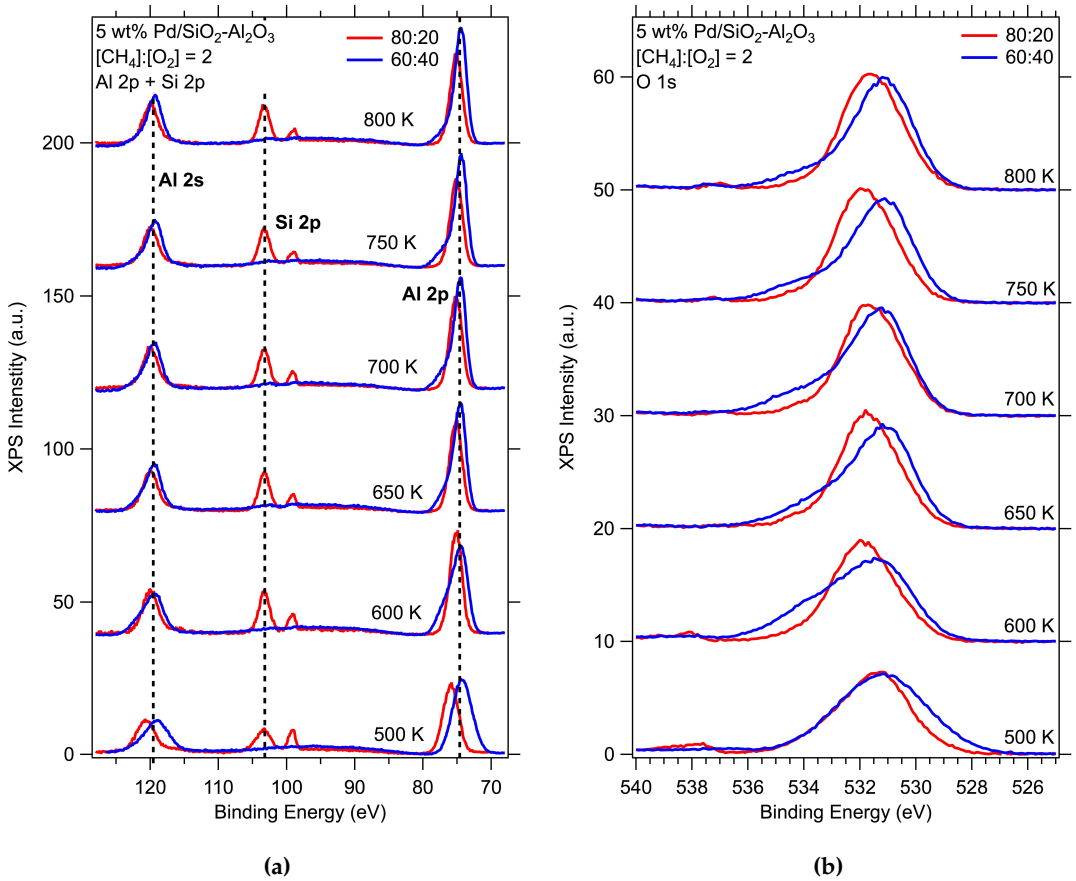

Figure 6.5: NAP-XPS data in the Al 2p, Si 2p and Al 2s (a) and O1s (b) regions of 5 wt% Pd/SiO_2-Al_2O_3 catalysts from 500 – 800 K, under $[CH_4]$:$[O_2]$ = 2 (total pressure = 0.33 mbar). SiO_2:Al_2O_3 ratio = 80:20 (red line) and 60:40 (blue line). Pass energy = 100 eV, $h\nu$ = 650 eV.

As well as monitoring the surface chemistry in-situ, the gas phase surrounding the catalyst can also be studied with NAP-XPS by retracting the sample away a few millimetres from the analyser cone. In this instance, the photoemission lines recorded are mostly those coming from the gas phase, rather than the surface of the sample whose photoelectrons are mostly scattered before reaching the analyser. Figure 6.6 shows NAP-XPS data in the C 1s and O 1s regions with the 60:40 sample retracted. In the C 1s spectrum, there are three main features that appear throughout the temperature ramp. The peak at 285 eV, characteristic of CH_4 or other hydrocarbon fragments of CH_4, is present at all temperatures but decreases in intensity with increased temperature. The formation of CO and CO_2 is also observed. At 600 K, 650 K and 700 K, a CO_2 peak appears at 291.5 eV and disappears by 750 K. Between 650 K and 800 K, a peak representative of CO at 290 eV appears to be growing in intensity with increased temperature, suggesting CO formation at these temperatures.

Figure 6.6b shows NAP-XP gas phase spectra in the O 1s region. CO_2 and CO peaks are also observed in these spectra at 536.2 eV and 537.2 eV respectively, and appear and disappear at the same temperatures at in the C 1s spectrum. Additional peaks seen in the O 1s region are those of surface O_2 and gas phase O_2 at 531.5 eV and 538.5 eV respectively. Note the gas phase O_2 peak height decreases with temperature, suggesting the oxygen in the reaction feed is used up. The peak at 534.5 eV that appears at 600 K, continues to grow at 650 K and 700 K, and decreases at 750 K and 800 K is characteristic of H_2O and, although not disappearing completely, it follows a similar pattern to that of the CO_2 peak in the O 1s and C 1s regions.

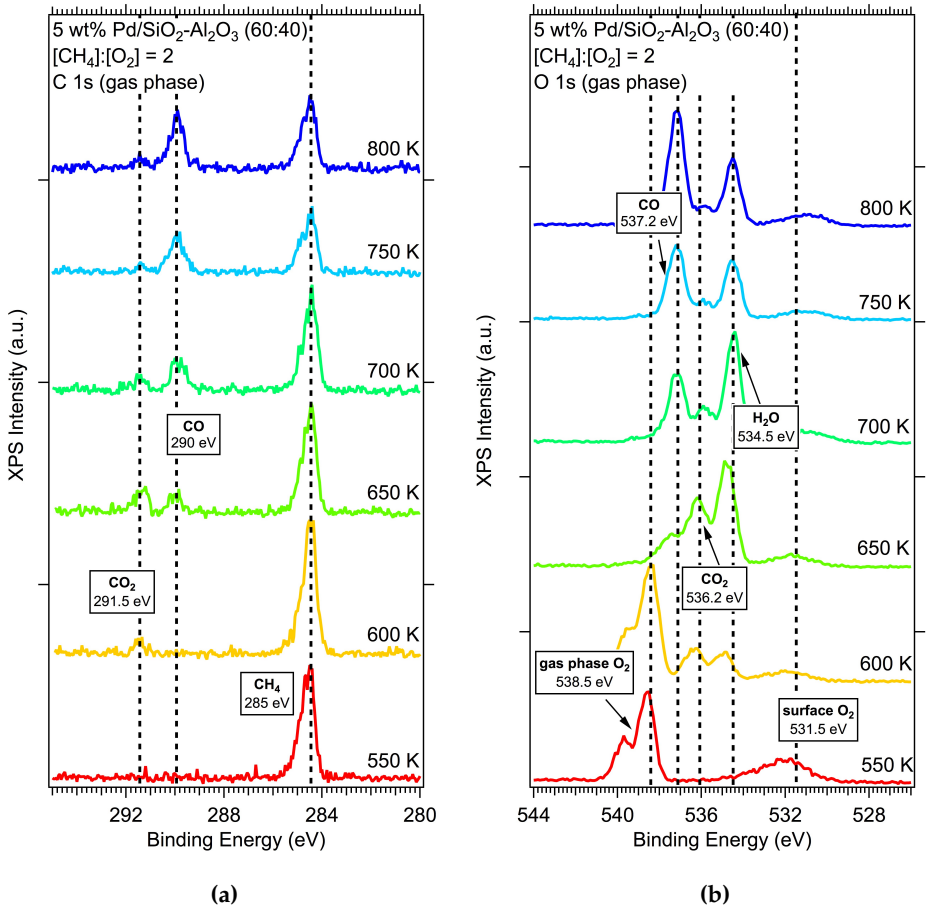

Figure 6.6: NAP-XPS data of 5 wt% Pd/SiO_2-Al_2O_3 catalyst (60:40) in the (a) C 1s region ($h\nu$ = 400 eV) and (b) O1 s region ($h\nu$ = 650 eV), taken at 50 K temperature intervals from 550 – 800 K taken in the gas phase. Pass energy = 100 eV.

6.3.2 Mass Spectrometry

For the duration of the NAP-XPS experiments, a mass spectrometer placed in the differential pumping stage of the NAP-XPS set-up was recording partial pressures of reactants and products. Masses 2 (H_2), 16 (CH_4), 18 (H_2O), 28 (CO), 32 (O_2) and 44 (CO_2) were collected to account for reactants and both complete oxidation and partial oxidation products. The mass spectrometry data helps to determine the relative reactivities of different catalysts and also to correlate the surface chemistry, as determined by NAP-XPS, with different reactive points in the reaction. Figure 6.7 shows the percentage conversion of methane to complete oxidation products (H_2O and CO_2) and to partial oxidation products (H_2 and CO) as a function of temperature as each catalyst is heated up. Each data point corresponds to the temperature at which the NAP-XP spectra were taken in Figure 6.3. From Figure 6.7, it is evident that the 60:40 catalyst produces H_2O and CO_2 at 550 K. Whilst for the 80:20 catalyst, H_2O and CO_2 are not formed until 600 K and with a visibly slower conversion rate. Syngas is produced between 600 – 650 K for both catalysts and although the onset for the 80:20 catalyst appears earlier, the final conversion percentage is greater for the 60:40 catalyst. Both SiO_2:Al_2O_3 ratios behave similarly in terms of onset temperature and overall methane conversion, however the lower SiO_2 content has a marginally higher conversion from methane to both complete oxidation products (CO_2 and H_2O) and partial oxidation products (H_2 and CO) at 800 K.

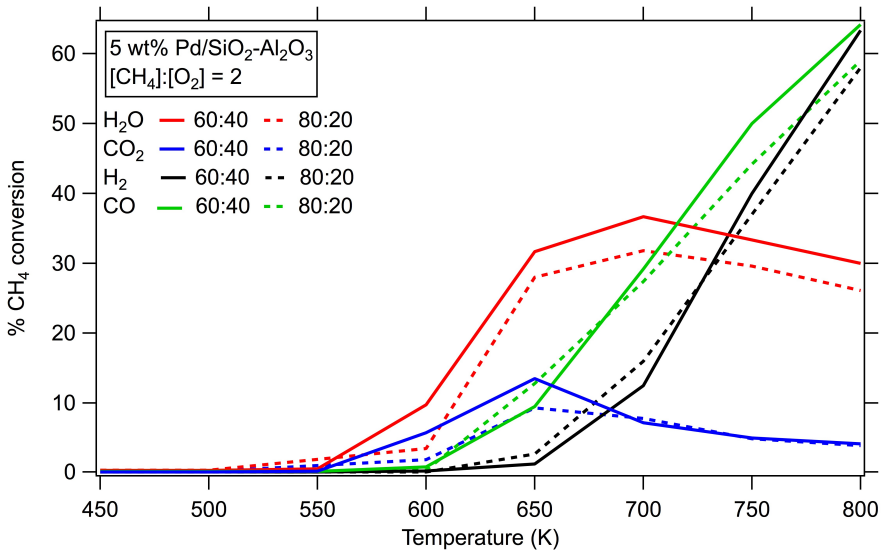

Figure 6.7: % CH_4 conversion of H_2O, CO_2, H_2 and CO as a function of temperature during heating of the catalyst. Solid lines represent SiO_2:Al_2O_3 ratio 60:40, dashed lines represent SiO_2:Al_2O_3 ratio 80:20.

On comparing the product formation from the mass spectrometry data with the Pd oxidation states from the NAP-XPS data (Figures 6.3 and 6.4), it appears that complete oxidation products, CO_2 and H_2O, are formed at T $>$ 650 K where the Pd is in an oxidised form PdO_x. The Pd reduces to metallic Pd at 650 K for both catalysts, and this temperature correlates to the onset of syngas production according to the mass spectrometry data in Figure 6.7. This result is consistent with pure Al_2O_3- and SiO_2-supported catalysts as discussed in Chapters 4 and 5 respectively. In addition, the NAP-XPS data of the gas phase can also be correlated directly with the product formation observed in the mass spectrometry data. The C 1s gas phase spectra shown in Figure 6.6a shows a peak characteristic of CO_2 appear at 600 K and diminish by 700 K; the same trend shown in Figure 6.7. The CO peak in Figure 6.6a appears at 650 K, which is also consistent with the mass spectrometry data in Figure 6.7.

Mass spectrometry data were also recorded during a steady cooling of the catalyst after reaching 800K. Figure 6.8 shows the % conversion of reactants and products during both the heating and cooling steps. The reaction is reversible: all products return to near 0% conversion by 450 K after cooling down and both reactants are regenerated to their original concentrations.

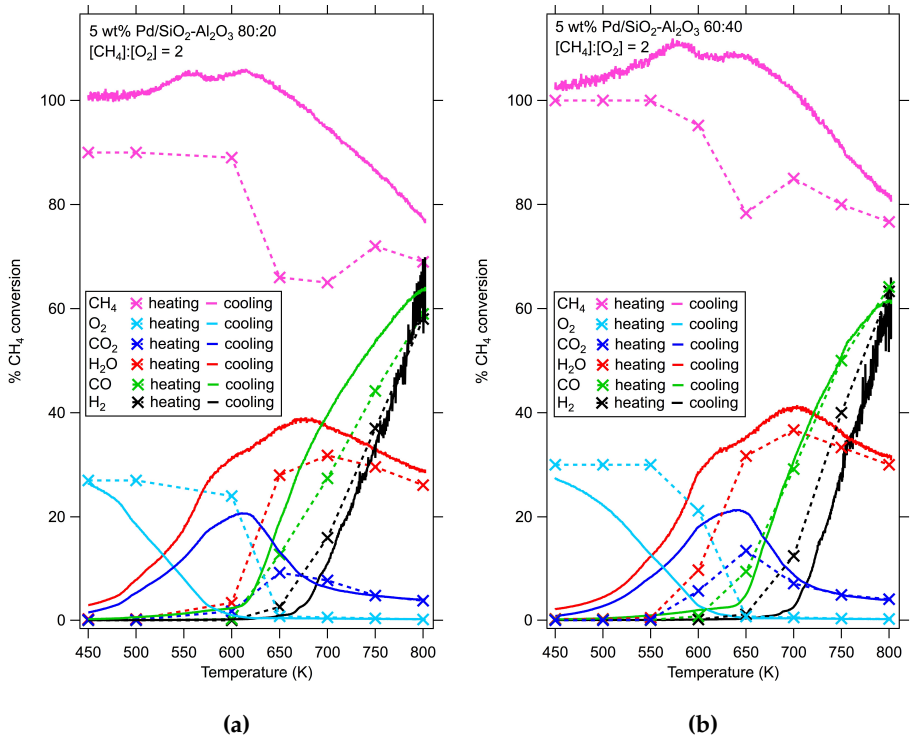

Figure 6.8: % CH_4 conversion on both heating during NAP-XPS data acquisition (dashed lines) and continuous cooling from 800 K after NAP-XPS data acquisition (solid lines) for (a) 80:20 Pd/SiO_2-Al_2O_3 catalyst and (b) 60:40 Pd/SiO_2-Al_2O_3 catalyst.

However, a hysteresis is observed, whereby a temperature shift occurs between the onset temperature on heating and the temperature at which the concentration diminishes on cooling. It generally seems that the temperature at which the concentrations of the high temperature products (H_2 and CO) fall is higher than the onset on heating, and the reverse is true for the low temperature products (CO_2 and H_2O). The decrease in reactants CH_4 and O_2 with increased temperature is reflected in the gas phase NAP-XP spectra in Figure 6.6, in which CH_4 (285 eV) and gas phase O_2 (531.5 eV) peaks in the C 1s region and O 1s region respectively diminish at higher temperatures. The temperature of the catalyst was manually controlled by applying a current, which counteracted any spontaneous temperature increase of the catalyst and provided a reliable temperature reading.

Using the continuous curves recorded whilst cooling down the catalysts, Arrhenius plots can be drawn to determine the activation energy needed for the onset of each product. The activation energy (E_a) is calculated from the gradient of the straight line by the Arrhenius equation:

$$\ln(P) = \text{const.} - \frac{E_a}{R}\left(\frac{1}{T}\right) \tag{6.1}$$

where P is the partial pressure of the gas recorded by the mass spectrometer as a function of temperature, T. The Arrhenius plots for each Pd/SiO_2-Al_2O_3 catalyst are shown in Figure 6.9, and the calculated activation energy values in Table 6.3. There is no significant difference between the two SiO_2:Al_2O_3 ratios in activation energy for most products. Only for H_2 formation the 60:40 sample has a much higher activation energy, which may be due to the higher Al_2O_3 content resulting in a higher H_2 affinity. The activation energy values for each reaction product are also in good agreement with those calculated for the complete and partial methane oxidation reactions with Pd/Al_2O_3 and Pd/SiO_2 samples as discussed in Chapters 4 and 5 respectively.

Catalyst	H_2	CO	H_2O	CO_2
SiO_2:Al_2O_3	E_a (kJ mol^{-1})	E_a (kJ mol^{-1})	E_a (kJ mol^{-1})	E_a (kJ mol^{-1})
80:20	167.3	167.7	38.2	42.1
60:40	201.4	168.8	44.2	46.1

Table 6.3: Calculated activation energies (E_a) for the onset of each product formation for Pd/SiO_2-Al_2O_3 catalysts under partial methane oxidation conditions ([CH_4]:[O_2] = 2 (0.33 mbar total pressure)).

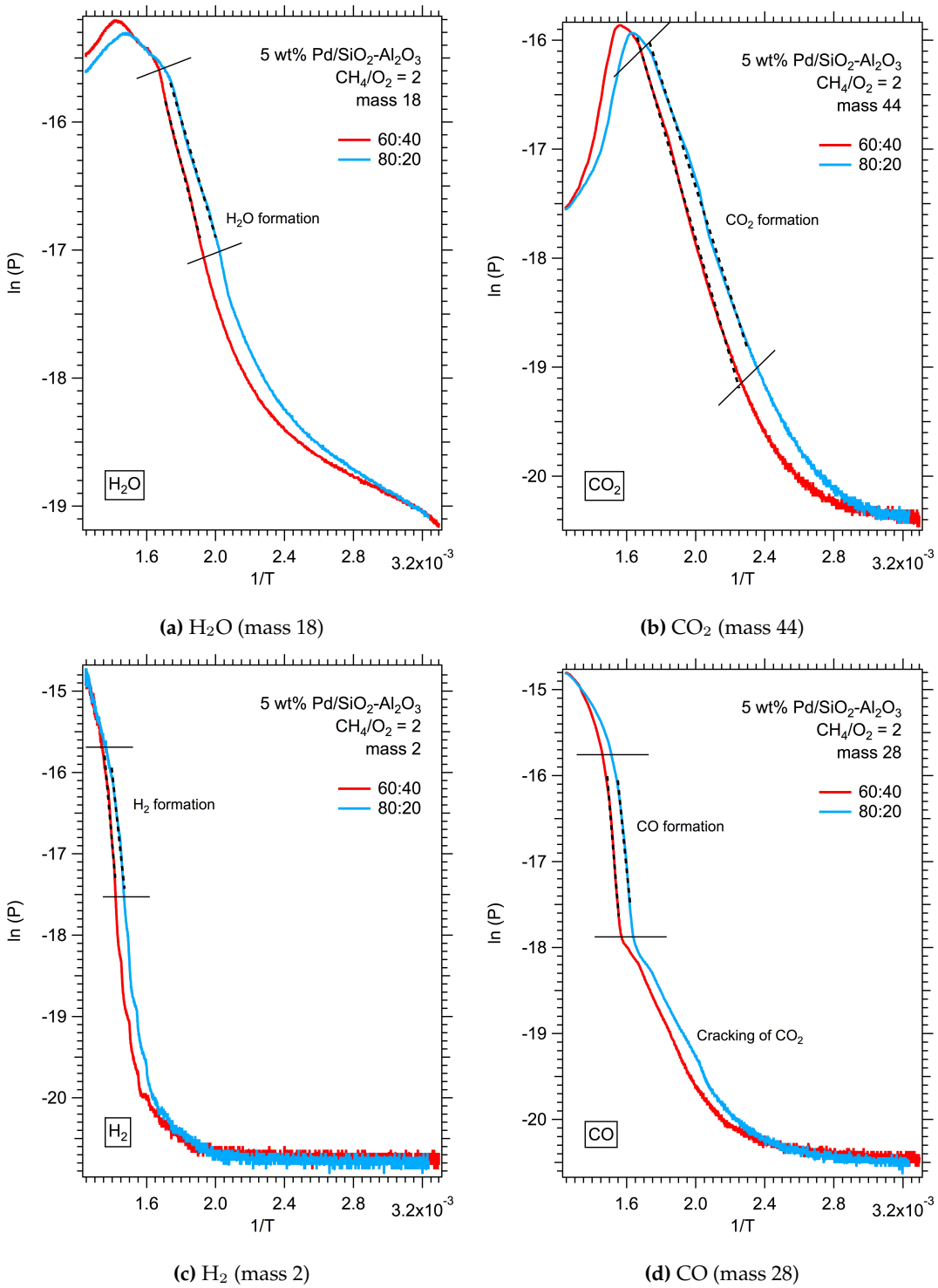

(a) H_2O (mass 18)

(b) CO_2 (mass 44)

(c) H_2 (mass 2)

(d) CO (mass 28)

Figure 6.9: Arrhenius plots of Pd/SiO_2-Al_2O_3 catalyst for each reaction product under $[CH_4]$:$[O_2]$ = 2 (total pressure 0.33 mbar). The activation energy for each product is calculated from the slope of the line at the onset temperature (Table 6.3).

6.4 Discussion

6.4.1 Support Effects

The formation of CO_2 and H_2O at lower temperatures than syngas formation is consistent with the reaction temperatures of complete and partial methane oxidation. Previous studies on complete methane oxidation have shown that the complete oxidation of methane to carbon dioxide and water occurs at around 550 K [65, 212, 245, 259]. This is also true for the 60:40 sample investigated in this study as determined by mass spectrometry, although CO_2 and H_2O formation start 50 K higher for the 80:20 sample. Generally Pd/Al_2O_3 catalysts are highly reactive towards complete methane combustion and so the increased Al_2O_3 content in the 60:40 catalyst may be providing extra reactivity. The partial oxidation of methane to syngas typically occurs at higher temperatures, with the onset of H_2 and CO starting between 650 – 700 K for Pd/Al_2O_3 [65] and Pd/SiO_2 catalysts. This can be attributed to the high activation energy needed to break C-H bonds for the formation of H_2 and is also seen in this study, whereby CO and H_2 formation starts at 600 – 650 K for both catalysts. An overall higher percentage conversion of CH_4 is observed for the 60:40 catalyst at 800 K, again perhaps due to the increased Al_2O_3 content in the support material, although the difference is non-significant at only $\sim$8%. The surface areas of the pure support materials differed by 132 m^2g^{-1} from 60% silica to 80% silica (Table 6.1), and the pore volume was 70% higher in the 60:40 support. This appears to have none or little effect in the reactivity of the catalysts, and similar effects have been reported by La Parola et al. [260]

The particle size of the Pd in these catalysts was not tested, although Muto and co-workers found that the degree of metal sintering was greater on mixed SiO_2-Al_2O_3 support than on pure SiO_2 or Al_2O_3. This stability effect played a role in the reactivity of the catalyst towards methane oxidation, in that a greater extent of sintering gave lower catalytic activity [195]. However, Niwa et al. reported that the methane oxidation turn-over frequency of a Pt/SiO_2-Al_2O_3 catalyst was higher than platinum on pure supports [261], indicating that Pd and Pt may have differing metal-support interactions and sintering effects with respective support materials.

6.4.2 Surface Acidity

The NAP-XPS data in the Pd 3d region appear quite similar, as opposed to the support material whereby the surface elemental composition appears quite different (Figure 6.5). The absence of surface silica in the 60:40 catalyst appears to affect the surface terminations from, in the presence of surface silica, a single silanol or terminal hydroxyl to a mixture of terminal and bridged hydroxyls as indicated by the O 1s NAP-XP spectra (Figure 6.5b). The surface hydroxyl terminations can play a role in the reactivity of the catalyst due to the variations in Lewis and Brønsted acidities of different oxides. The ability for a hydroxyl group to release H^+ ions, or Brønsted acidity, has proven to play a role in catalytic activity in silica-aluminas and zeolite support materials by altering the energetics of the formation of catalytic active sites [262, 263].

A pure Al_2O_3 FT-IR spectrum contains three OH bands assigned to three different OH configurations: Al-OH, Al_2-OH and Al_3-OH [258]. The 60% silica samples in this study also exhibit a surface similar to that of Al_2O_3, as the silica appears to be encapsulated by the alumina (Figure 6.5a). At 500 K, the O 1s spectra in Figure 6.5b are similar for both supports but as the temperature increases, the spectra become much broader for the lower silica content samples, suggesting multiple hydroxyl features are also present on the surface and as a result, increased Brønsted acidity. The surface terminations do not change much from UHV to ambient pressures, except that the slight shift towards lower binding energy could indicate a greater contribution from bulk oxygen under ambient pressures. The narrowing peaks under ambient pressures compared to UHV is likely due to less surface charging with the presence of the gas (Figure 6.10).

Daniell et al. [257] have reported that the Brønsted acidity of silica-aluminas with high silica percentages (70% and above) is similar, and exhibit silica-like surface properties by a single OH band in an FT-IR spectrum. Despite the spectral similarities, it is unclear if this OH band is denoting a terminal hydroxyl (silanol) as most common in pure silica, or a bridged OH between Al and Si atoms as common to zeolites [264, 265]. The latter would give greater Brønsted acidity, and so due to conflicting acidity studies of the surface of silica-aluminas, it is assumed that the hydroxyl groups of non-zeolitic mixed oxides are terminal on the Si atom [264]. However, these silanols in mixed oxides still show some Brønsted acidity, which is primarily explained by the ability for the O^- to bridge to a free Al^{3+} cation after deprotonation [264]. Therefore, despite the differences in surface termination, the similarities in reactivity of

the Pd/SiO$_2$-Al$_2$O$_3$ samples studied in this experiment may be a result of the similar Brønsted acidity between 60% silica content and 80% silica content, as reported by Daniell [257].

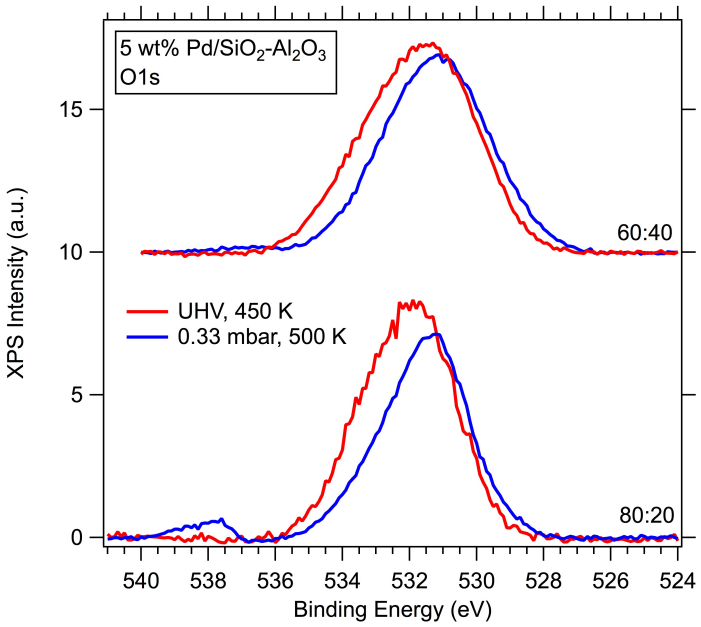

Figure 6.10: XPS spectra of 5 wt% Pd/SiO$_2$-Al$_2$O$_3$ catalysts (80:20 and 60:40) under UHV and 0.33 mbar CH_4 and O_2 (2:1 ratio). $h\nu$ = 650 eV.

In general, Lewis acid sites are absent on pure silica, which causes weak metal-support interaction through the Brønsted sites, low metal dispersion and higher risk of sintering. The reverse effect occurs on pure alumina supports, in which the metal is bonded via Lewis acid sites causing strong metal-support interactions. Mixed-supports combine both Lewis and Brønsted acidity with bridged Al-O-Si termini, which in some cases can provide an overall increase in reactivity [260]. In the case of these catalysts, silicon species are displaced by Al with Al_2O_3 concentrations at 40%, and so the bridged Si-O-Al surface structure with silanol groups is only observed for the 80:20 catalyst. It appears that concentrations of SiO_2 above 80% are required for bridged surface termini and contributions from both Al and Si. However, the alumina-like surface in the 60:40 catalyst and the strong Brønsted acidity from weakly bound H^+ ions could be responsible for the extra reactivity of this catalyst.

6.5 Conclusions

NAP-XPS and mass spectrometry have been employed to determine the surface composition and catalytic reactivity towards methane oxidation of mixed SiO_2-Al_2O_3 supported Pd catalysts. NAP-XP spectra showed that, under 0.33 mbar (total pressure) of methane and oxygen (2:1) and increased temperature, the surface Pd reduces from PdO_x to Pd metal at 650 K irrespective of SiO_2:Al_2O_3 ratio. Mass spectrometry shows that at 650 K partial methane oxidation products (H_2 and CO) are forming, suggesting a reduced Pd species is the active phase for partial oxidation of methane to syngas. This is in agreement with previous work done on partial methane oxidation with Pd catalysts [65].

The Si 2p signal in the NAP-XP spectra is very low for the 60:40 catalyst, which would suggest with increased alumina content above 20% the surface is predominately alumina-like. This is further verified in the O 1s spectra that show a number of different oxygen species in the 60:40 catalyst indicative of the varying hydroxy termini usually present on alumina surfaces. The 60:40 catalyst also displays a slightly higher overall conversion of methane to syngas at 800 K, likely due to the increased alumina content that has been shown to be a more reactive support than silica. The 80:20 catalyst also shows a good degree of methane conversion to syngas ($>$ 50% conversion at 800 K). Despite similar activity, NAP-XPS shows a very different surface composition in terms of the support material to the 60:40 catalyst suggesting other factors are at play. Enhanced surface acidity by bridging hydroxyls in the Si-O-Al configuration may explain why this catalyst is also effective.

7 Comparisons of Pd Catalyst Supports

NAP-XPS and in-situ mass spectrometry have been used to identify the behaviour of Pd catalysts with different support materials under model methane oxidation reaction conditions. As well as comparing the different particle sizes of the same catalyst, the effect of the catalyst support on the surface reactivity and composition can also be discussed and compared.

7.1 Particle Size Effects

For Pd/Al_2O_3 catalysts, a particle size effect is seen where the onset of syngas formation decreases with increasing particle size from 5 – 10 nm. A similar effect is seen for Pd/SiO_2 catalysts, with Pd particle sizes of 2 – 6 nm. Particle sizes above 6 nm were not tested for Pd/SiO_2 catalysts, but studies on polycrystalline Pd foil have shown that large grain sizes of Pd (> 1 μm) are not as reactive as Pd nanoparticles. Therefore, it is expected there would be an optimum size before reactivity is hindered. From the data presented in this thesis, it is not clear if the optimum particle size for Pd/Al_2O_3 and Pd/SiO_2 catalysts is the same. For both Al_2O_3 and SiO_2 catalysts, PdO reduces to metallic Pd at lower temperatures with larger Pd particles, shown by a high to low binding energy shift in the Pd 3d NAP-XPS spectra. The temperature at which the PdO reduces coincides with syngas formation, as seen by an increase in the partial pressures of masses 2 and 28 (H_2 and CO) in the mass spectrometry data. The smaller the nanoparticle, the stronger the Pd-O bond, and therefore the reducibility of PdO for smaller particles is weaker. As a result, fewer oxygen vacancies are available for CH_4 to bind with for the rate-determining step. Using the Arrhenius plots to determine the activation energy for different product formation, no significant particle size effects were observed in terms of activation energy, despite the onset temperatures being different. This suggests an pre-exponential factor concerning the number of active sites, or the reducibility of the particle, should be accounted for in the calculation.

7.2 Sample Charging

Sample charging is observed for Pd catalysts with Al_2O_3, SiO_2 and SiO_2-Al_2O_3 supports. Peak shifting and broadening are both seen in all NAP-XPS spectra, particularly at temperatures below 600 K. Under ambient pressures of CH_4 (0.22 mbar) and O_2 (0.11 mbar), the greatest extent of sample charging, in terms of binding energy shift, is seen for Pd/Al_2O_3 catalysts. Figure 7.1 shows the binding energy shift of the Al 2p peaks for Pd/Al_2O_3 and Pd/SiO_2-Al_2O_3 catalysts and the Si 2p peaks for the Pd/SiO_2 catalysts from their respective literature values (74.5 eV and 103.3 eV) as a function of sample temperature.

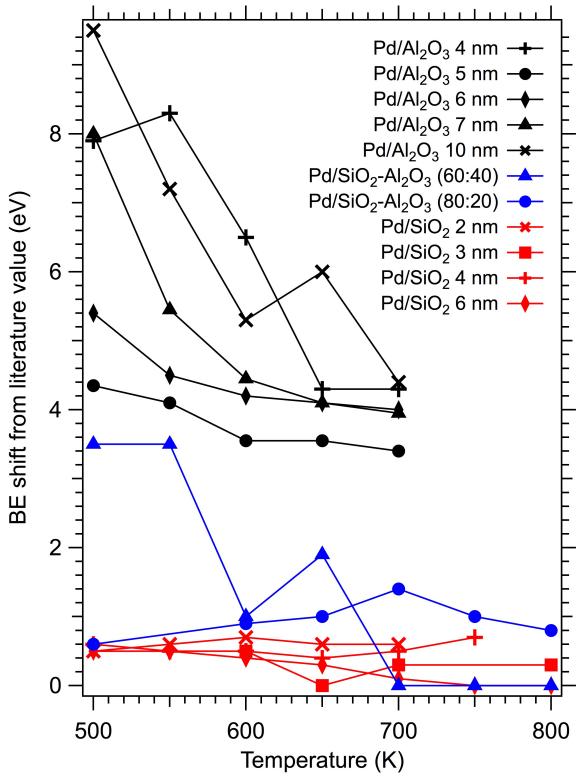

Figure 7.1: The binding energy shift of the peak with respect to the literature value, used to correct the energy scale for the corresponding Pd 3d spectra for all samples, as a function of sample temperature: Al 2p peak at 74.5 eV for Pd/Al_2O_3 and Pd/SiO_2-Al_2O_3 samples and Si 2p peak at 103.3 eV for Pd/SiO_2 samples. Pressure = 0.33 mbar ($[CH_4]/[O_2] = 2$.)

From Figure 7.1, the binding energy shift of the Pd/Al_2O_3 catalysts is greater than for the other supports. In addition, Pd/SiO_2-Al_2O_3 catalyst with the higher Al_2O_3 content (60:40) charges more than the mixed support sample with the lower Al_2O_3 content (80:20). Under ambient pressures, Pd/SiO_2 catalysts charge less than Al_2O_3-supported Pd, which is expected due to the high resistance of Al_2O_3 (10^{13} Ω at 500 K [266]).

7.3 Activity

All catalysts produced the four main products of methane oxidation, CO_2, H_2O, CO and H_2, under 0.33 mbar ($[CH_4]/[O_2] = 2$) with conversion rates to syngas greater than 20% at 700 K for most catalysts. At 700 K, a 25% conversion of methane to both CO and H_2 was observed for the most reactive Pd/Al_2O_3 catalyst (10 nm). The most reactive Pd/SiO_2 catalyst (6 nm) only showed 5% and 18% conversion of methane to H_2 and CO respectively at 700 K although after heating to 800 K, 40% conversion to both H_2 and CO was reached. Similar behaviour was observed for the mixed SiO_2-Al_2O_3 supports at 700 K, although by 800 K the conversion of CH_4 to syngas had reached 60%, which suggests that Pd/SiO_2-Al_2O_3 catalysts are more active towards syngas production than Pd/SiO_2 catalysts under these conditions. Pd/Al_2O_3 catalysts were not studied at temperatures above 720 K, due to heating constraints, although the Pd/Al_2O_3 catalysts appear to be more active than the Pd/SiO_2 catalysts in terms of the onset temperature of syngas. Catalysts with particle sizes 4 – 6 nm are comparable samples and with an Al_2O_3 support, syngas formation occurs at lower temperatures than with a SiO_2 support (Figure 7.2).

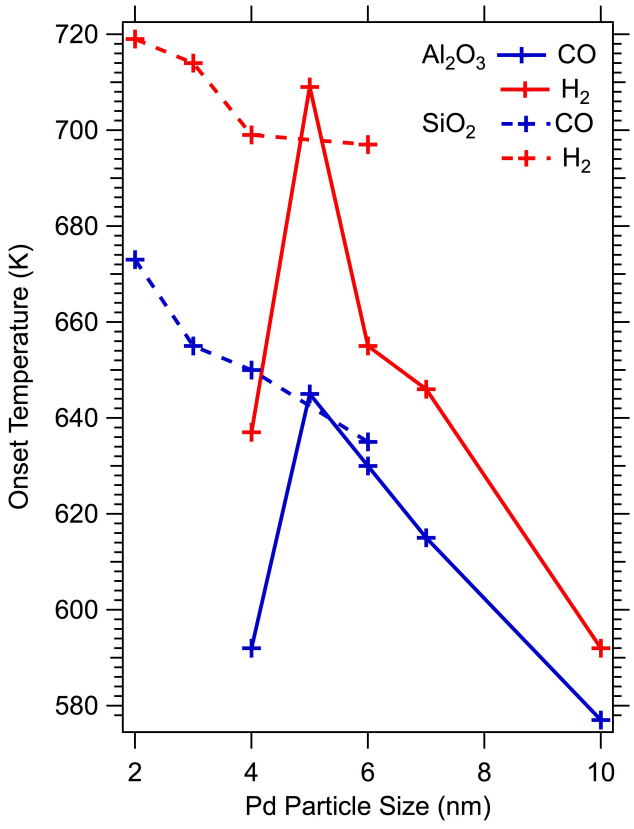

Figure 7.2: Comparison of the activity of Pd/Al_2O_3 and Pd/SiO_2 catalysts under 0.33 mbar ($[CH_4]/[O_2] = 2$)

The activation energies for each product formation for each catalyst are stated in Table 7.1. The activation energies for the partial oxidation products (H_2 and CO) are much higher for all catalysts than for the complete oxidation products (H_2O and CO_2). In general, the Pd/Al_2O_3 catalysts have lower activation energies for H_2O, CO_2 and CO formation than the other supports. Pd/Al_2O_3 catalysts have a slightly higher average activation energy for H_2 (183.1 kJ mol^{-1}) than Pd/SiO_2 catalysts (181.1 kJ mol^{-1}), and the Pd/SiO_2-Al_2O_3 catalyst with the higher Al_2O_3 content (60:40) has a higher activation energy for H_2 than the mixed support catalyst with the lower Al_2O_3 content (80:20). This suggests that Al_2O_3 has a slightly higher affinity for H_2 than SiO_2.

Catalyst	**H_2**	**CO**	**H_2O**	**CO_2**
Pd/Al_2O_3	E_a (kJ mol^{-1})	E_a (kJ mol^{-1})	E_a (kJ mol^{-1})	E_a (kJ mol^{-1})
4 nm	186.8	146.7	25.1	25.1
5 nm	154.7	109.7	20.6	17.9
6 nm	178.8	128.5	24.9	23.5
7 nm	176.6	132.8	21.9	18.6
10 nm	218.8	159.1	36.5	36.4
Pd/SiO_2:Al_2O_3	E_a (kJ mol^{-1})	E_a (kJ mol^{-1})	E_a (kJ mol^{-1})	E_a (kJ mol^{-1})
80:20	167.3	167.7	38.2	42.1
60:40	201.4	168.8	44.2	46.1
Pd/SiO_2	E_a (kJ mol^{-1})	E_a (kJ mol^{-1})	E_a (kJ mol^{-1})	E_a (kJ mol^{-1})
2 nm	187.9	162.3	46.4	48.8
3 nm	175.4	158.1	40.8	43.5
4 nm	180.2	160.0	40.9	42.2
6 nm	181.0	170.9	40.1	40.6

Table 7.1: Calculated activation energies (E_a) for the onset of each product formation for all catalysts under partial methane oxidation conditions ($[CH_4]$:$[O_2]$ = 2 (0.33 mbar total pressure)).

The onset temperatures of CO and H_2 for the Pd/SiO_2-Al_2O_3 samples are 600 K and 650 K respectively (see Figure 6.7). Compared to the most reactive particle sizes of Pd/Al_2O_3 (10 nm) and Pd/SiO_2 (6 nm) in these studies, the order of reactivity of the supports would be $SiO_2 < SiO_2$:$Al_2O_3 < Al_2O_3$.

7.4 Conclusion

It is well known that the interaction between the metal and the support affects the redox properties of the metal [174, 267, 268], which in turn affects the reactivity of the catalyst. A strong metal-support interaction can inhibit the adsorption of reactant molecules onto the metal, thus decreasing the rate of reaction [269]. Although there is no conclusive evidence that the particle size of the metal influences the strength of the metal-support interaction, it has been known that smaller particles have stronger metal-support interactions [270]. This may explain why smaller particle sizes were less reactive towards partial methane oxidation in these studies. In addition, the decrease in activity for Pd/SiO_2 catalysts is likely due a metal-support interaction effect. It has been previously reported that Si atoms can migrate to the surface from the bulk support material to the surface and block active sites, particularly in the presence of water that helps to facilitate movement [199, 239, 244]. Silicon may block the active sites by either encapsulation of the Pd and form a layer of silicon on the surface, or by forming Pd silicides. There is some spectroscopic evidence for this in our data whereby the peak area of the Si 2p silicon oxides peak in the NAP-XP spectra is increased under ambient pressures and decreased under UHV. Due to attenuation of XPS signal under higher pressures, this signifies that an increased amount of silicon is moving to the surface under reaction conditions. This phenomenon is not seen with Pd/Al_2O_3 and so appears to be an effect of the SiO_2 support.

8 Summary and Conclusions

A range of supported-Pd catalysts were studied in this project, with varying metal particle size and support material. The catalysts were synthesised using the co-precipitation method with γ-Al_2O_3, SiO_2 and SiO_2-Al_2O_3 supports, and calcined to different temperatures in order to control the particle size. The catalysts were characterised with in-house analytical methods including XPS, TEM, XRD and ICP-MS in order to define the surface composition, bulk structure and mean particle sizes.

The surface chemistry and reaction products of a selection of well-defined samples were characterised during the partial oxidation of methane. Using a gas composition of $[CH_4]$:$[O_2]$ = 2 (0.33 mbar total pressure), the expected products were CO and H_2 although complete oxidation products (CO_2 and H_2O) were also formed at lower temperatures due to the lower activation energy barrier of the latter reaction. With NAP-XPS, it was possible to identify the active phase of the Pd with each product formation, due to the monitoring of the oxidation state change of Pd in the Pd 3d region. At lower temperatures (500 – 650 K) where CO_2 and H_2O are produced, the Pd is in the form of PdO. As the temperature increases (700 – 800 K) and the thermodynamic equilibrium shifts to favour partial oxidation (H_2 and CO), the Pd reduces to metallic Pd. From this data, it can be concluded that the active phase of Pd for the complete oxidation of methane is PdO, and for the partial oxidation of methane to syngas the active phase of Pd is metallic Pd. This is observed for all Pd catalysts studied, irrespective of particle size or support. It is likely, however, that both reactions require both oxidation states of Pd to proceed as, due to the high resolution of the synchrotron data, it is possible to resolve two oxidation states for each Pd 3d spectra at each temperature. When PdO is the dominant phase, metallic Pd is also present and vice versa, suggesting a combination of both phases is needed. This would support a mechanism similar to which Fujimoto et al. reported, in which a methane molecule binds to a vacant Pd^0 site, and the oxygen from a neighbouring PdO takes a hydrogen atom from the CH_4 molecule [24]. In this case, the breaking of the C-H bond is the rate-determining step and the reaction rate is dependent on the number of PdO sites

and vacant Pd^0 sites.

Using in-situ mass spectrometry, the partial pressures of the reactants and products can be recorded as a function of temperature, alongside the NAP-XPS spectra. A particle size effect was observed for both Pd/Al_2O_3 and Pd/SiO_2, whereby the onset temperature of H_2 and CO occurred at a lower temperature for larger particles (10 nm and 6 nm respectively), which can be correlated to the reduction of Pd in the NAP-XPS spectra. Using the partial pressures obtained by the mass spectrometry data and the Arrhenius equation, the activation energy for the formation of each methane oxidation product can be determined. Four reactions were found to be occurring in total:

1. At 500 – 625 K, the complete oxidation of methane to CO_2 and H_2O is favoured using an excess of oxygen (E_a = 18 – 50 kJ mol^{-1}):

$$CH_4 + 2\,O_2 \longrightarrow CO_2 + 2\,H_2O$$

2. At the same temperature (500 – 625 K), a slight excess of O_2 is used to partially oxidise CH_4 to CO and H_2O (E_a = 30 – 35 kJ mol^{-1}):

$$CH_4 + \tfrac{3}{2}\,O_2 \longrightarrow CO + 2\,H_2O$$

3. At 625 – 750 K, most of the oxygen is used up in the previous two reactions at lower temperatures, and the favoured reaction at higher temperatures and low concentrations of oxygen is the partial oxidation of methane to syngas (E_a = 110 – 220 kJ mol^{-1}):

$$CH_4 + \tfrac{1}{2}\,O_2 \longrightarrow CO + 2\,H_2$$

4. In a side reaction at 625 – 715 K, H_2 produced in the partial oxidation of methane reacts with CO_2 produced from complete oxidation, in the water-gas shift reaction to form more CO and H_2O (E_a = 11 – 14 kJ mol^{-1}):

$$CO_2 + H_2 \longrightarrow CO + H_2O$$

Unlike the onset temperatures, no particle size effect is observed for the activation energies. A pre-exponential factor to represent the reducibility of the catalyst or the number of active sites should be included in the Arrhenius calculation to account for the different particle sizes.

When Al_2O_3 and SiO_2 are mixed, different ratios of Al_2O_3 and SiO_2 can have an effect on the surface chemistry. Two SiO_2:Al_2O_3 ratios (80:20 and 60:40) were used as supports for Pd and studied with NAP-XPS and in-situ MS. It was found that both catalysts show similar activity, but the addition of Al_2O_3 has an effect on the surface composition. With 20% Al_2O_3, both Al_2O_3 and SiO_2 are present on the surface and show good activity towards syngas production. A mixed oxide surface usually consists of bridging Si-O-Al sites which exhibit both Lewis and Brønsted acidity (depending on if the oxygen atom is protonated) and has been shown to have a positive effect on reactivity [260]. With 40% Al_2O_3, the SiO_2 XPS signal is hardly visible on the spectra and the O 1s signal exhibits -OH characteristics suggesting the surface is alumina-like with strong Brønsted acid -OH termini. The Pd/Al_2O_3 catalyst showed better activity towards syngas formation than the Pd/SiO_2 so it would be expected that the mixed support with the highest Al_2O_3 content would be most reactive, particularly with an alumina-like surface. In comparing the onset temperatures of syngas formation for different support materials, the activity follows the order $Pd/SiO_2 < Pd/SiO_2$-$Al_2O_3 < Pd/Al_2O_3$.

Due to the nature of the support material, charging of the sample was observed during NAP-XPS measurements under both UHV and ambient pressures. This affected the spectra by shifting the binding energy position and broadening and splitting the peaks. Charging was found to be temperature dependent, and at higher temperatures (> 500 K) the samples became increasingly conducting with increasing temperature. This is likely to be an effect of ion conductivity, whereby ions can "hop" between interstitial surface sites and carry charge. The availability of these charge carriers appears to be an activated process, with calculated activation energies of <0.5 eV for Pd/Al_2O_3 and Pd/SiO_2 catalysts.

In summary, this project has provided NAP-XPS data of "real" catalyst samples under close-to-real conditions and a novel insight into the surface chemistry of methane oxidation catalysts in-situ. Problems with sample charging from the insulating supports were circumvented by the use of a conducting Si wafer substrate and the sample conductivity was found to be temperature dependent. Artefacts of sample charging are still present in the spectra, however, and are accounted for by employing a custom peak fitting technique. Pd catalysts were shown to behave in similar ways, with the particle size affecting the reducibility, and hence reactivity, of the catalyst.

9 Future Work and Project Scope

The main outcomes of this project was proving that insulating samples can be successfully characterised using NAP-XPS and that NAP-XPS is an effective tool to characterise the surface chemistry of catalysts in-situ. There are many more catalysts that should be tested in this way, such as Pd/Al_2O_3 and Pd/SiO_2 catalysts with higher particle sizes than studied here, in order to determine the optimum particle size for syngas activity. Catalysts with alternative supports such as ZrO_2 and CeO_2 could be prepared and studied to give more information with regards to the metal-support interaction of different PGM and support material, a topic that is still greatly debated. Bimetallic catalysts are also of interest, particularly the Pt-Pd system, with applications in engine exhausts it is desirable to understand the extent of the interaction of one metal with another.

Continuing on from the work on mixed SiO_2-Al_2O_3 supports, acidity/basicity tests should be performed to determine the Brønsted and Lewis acid sites and whether the hypothesis discussed in Chapter 6 is correct. In future, the Brønsted acidity should be characterised for all catalysts, as this may prove to be an important variable in catalytic activity. It would also be interesting to manually mix together Al_2O_3 and SiO_2 to create a mixed support and see whether this behaves any differently to the manufactured mixed SiO_2-Al_2O_3. The difficulty in the analysis of nanoparticles that are not of uniform shape and size is that there are few data they can be compared to. It would be useful to have more standard measurements that can be used to help characterise catalytic nanoparticles, such as repeating the experiment with a pure Al_2O_3 sample, for example. In addition, the reaction should also be run with CH_4 only in the gas phase to confirm that the products are as a result of oxidation rather than high temperatures.

The near-ambient pressures used in this project are orders of magnitude higher than ultra-high vacuum pressures and are extremely useful for modelling the reaction mixtures, although 0.33 mbar is still a very low pressure compared to the actual reactions that typically operate at $\sim$1-100 bar. NAP-XPS endstations

at synchrotrons are constantly being developed in order to achieve higher pressures in conjunction with XPS high signals. The VERSOX beamline at Diamond Light Source is able to operate at pressures up to 5 mbar and with the introduction of an enclosed sample cell, the HIPPIE NAP-XPS endstation at MAX IV can accommodate pressures of up to 25 mbar and a 100% relative humidity environment [271]. The continual development of NAP-XPS endstations to achieve higher working pressures at no compromise to the spectra is highly promising for this field of research and will be an important part of catalyst design and the elucidation of a catalyst's behaviour in-situ.

References

[1] I. Chorkendorff and J. W. Niemantsverdriet. *Concepts of Modern Catalysis and Kinetcs*. Wiley-VCH Verlag, Weinheim, 2nd edition, 2007.

[2] J. R. H. Ross. *Heterogeneous Catalysis: Fundamentals and Applications*. Elsevier, 2012.

[3] R. A. Sheldon and H. van Bekkum, editors. *Fine Chemicals through Heterogeneous Catalysis*. John Wiley & Sons, 2008.

[4] J. Daintith, editor. *A Dictionary of Chemistry*. Oxford University Press, 6th edition, 2008.

[5] B. A. Averill, J. A. Moulijn, R. A. van Santen, and P. W. N. M. van Leeuwen, editors. *Catalysis: An Integrated Approach*. Elsevier, 2nd edition, 1999.

[6] J. R. Jennings, editor. *Catalytic Ammonia Synthesis: Fundamentals and Practice*. Springer Science and Business Media, 2013.

[7] M. Bowker. *The Basis and Applications of Heterogeneous Catalysis*. Number 53 in Oxford chemistry primers. Oxford University Press, 1998.

[8] M. Misono. *Heterogeneous Catalysis of Mixed Oxides: Perovskite and Heteropoly Catalysts*, volume 176 of *Studies in surface science and catalysis*. Newnes, 2013.

[9] R. W. Joyner and R. A. van Santen. *Elementary Reaction Steps in Heterogeneous Catalysis*. Springer Science and Business Media, 1993.

[10] R. J. Baxter and P. Hu. Insight into why the Langmuir-Hinshelwood mechanism is generally preferred. *J. Phys. Chem.*, 116:4379, 2002.

[11] A. D. Allian, K. Takanabe, K. L. Fujdala, X. Hao, T. J. Truex, J. Cai, C. Buda, M. Neurock, and E. Iglesia. Chemisorption of CO and mechanism of CO oxidation on supported platinum nanoclusters. *J. Am. Chem. Soc.*, 133:4498–4517, 2011.

[12] R. B. Jordan. *Reaction Mechanisms of Inorganic and Organometallic Systems*. Oxford University Press, 3rd edition, 1997.

[13] D. H. F. Liu and B. G. Liptak. *Environmental Engineers' Handbook*. CRC Press, 1999.

[14] A. J. Farebrother, A. J. H. M. Meijer, D. C. Clary, and A. J. Fisher. Formation of molecular hydrogen on a graphite surface via an Eley-Rideal mechanism. *Chem. Phys. Lett.*, 319:303–308, 2000.

[15] M. Rutigliano, M. Cacciatore, and G. D. Billing. Hydrogen atom recombination on graphite at 10 K via the Eley-Rideal mechanism. *Chem. Phys. Lett.*, 340:13–20, 2001.

[16] M. Xi and B. E. Bent. Evidence for an Eley-Rideal mechanism in the addition of hydrogen atoms to unsaturated hydrocarbons on Cu{111}. *J. Vac. Sci. Technol.*, 10:2440, 1992.

[17] P. Mars and D. W. van Krevelen. Oxidations carried out by means of vanadium oxide catalysts. *Chem. Eng. Sci.*, 3:41–59, 1954.

[18] C. T. Herbschleb. *ReactorSTM-Imaging Catalysts under Realistic Conditions*. PhD thesis, Leiden University, 2011.

[19] A. R. Almeida, J. A. Moulijn, and G. Mul. Photocatalytic oxidation of cyclohexane over TiO_2: Evidence for a Mars-van Krevelen mechanism. *J. Phys. Chem. C*, 115:1330–1338, 2011.

[20] M. Bowker, A. F. Carley, and M. House. Contrasting the behaviour of MoO_3 and MoO_2 for the oxidation of methanol. *Catal. Lett.*, 120:34–39, 2008.

[21] J. J. Spivey, editor. *Catalysis*, volume 14 of *Specialist Periodical Reports*. Royal Society of Chemistry, 1999.

[22] E. P. J. Mallens, J. H. B. J. Hoebink, and G. B. Marin. The reaction mechanism of the partial oxidation of methane to synthesis gas: A transient kinetic study over rhodium and a comparison with platinum. *J. Catal.*, 167:43–56, 1997.

[23] J. Zhu, J. G. van Ommen, H. J. M. Bouwmeester, and L. Lefferts. Activation of O_2 and CH_4 on yttrium-stabilized zirconia for the partial oxidation of methane to synthesis gas. *J. Catal.*, 233:434–441, 2005.

[24] K. Fujimoto, F. Riberio, M. Avalos-Borja, and E. Iglesia. Structure and reactivity of PdO_x/ZrO_2 catalysts for methane oxidation at low temperatures. *J. Catal.*, 179:431–442, 1998.

[25] F. R. Hartley, editor. *Chemistry of the Platinum Group Metals: Recent Developments*, volume 11 of *Studies in Inorganic Chemistry*. Elsevier, 2013.

[26] V. N. Pitchkov. The discovery of ruthenium. *Platinum Met. Rev.*, 40:181–188, 1996.

[27] Johnson Matthey. Properties of PGM - Precious Metals Management. Webpage, September 2016.

[28] F. K. Crundwell, M. Moats, and V. Ramachandran. *Extractive Metallurgy of Nickel, Cobalt and Platinum Group Metals*. Elsevier, 2011.

[29] H. Windawi. Controlling the exhaust emissions from alternative fuel vehicles. *Platinum Met. Rev.*, 36:185–195, 1992.

[30] J. Lee and D. Trimm. Catalytic combustion of methane. *Fuel Process. Technol.*, 42:339–359, 1995.

[31] M. Maedge. Methane as a Vehicle Fuel in Europe. Institution of Mechanical Engineers, London, September 2014.

[32] J. Chen, H. Arandiyan, X. Gao, and J. Li. Recent advances in catalysts for methane combustion. *Catal. Surv. from Asia*, 19:140–171, 2015.

[33] A. Raj. Methane emission control: A review of mobile and stationary source emissions abatement technologies for natural gas engines. *Johns. Matthey Technol. Rev.*, 60:228–235, 2016.

[34] B.C. Enger, R. Lodeng, and A. Holmen. A review of catalytic partial oxidation of methane to synthesis gas with emphasis on reaction mechanisms over transition metal catalysts. *Appl. Catal. A: Gen.*, 346:1–27, 2008.

[35] T. Baldwin and R. Burch. Remarkable activity enhancement in the catalytic combustion of methane on supported palladium catalysts. *Catal. Lett.*, 6:131–138, 1990.

[36] I. Czekaj, K. A. Kacprzak, and J. Mantzaras. CH_4 combustion cycles at Pd/Al_2O_3 - important role of support and oxygen access. *Phys. Chem. Chem. Phys.*, 15:11368, 2013.

[37] L. J. Hoyos, H. Praliaud, and M. Primet. Catalytic combustion of methane over palladium supported on alumina and silica in presence of hydrogen sulfide. *Appl. Catal. A: Gen.*, 98:125–138, 1993.

[38] P. Araya, S. Guerrero, J. Robertson, and F. Gracia. Methane combustion over Pd/SiO_2 catalysts with different degrees of hydrophobicity. *Appl. Catal. A: Gen.*, 283:225–233, 2005.

[39] S. Yang, A. Maroto-Valiente, M. Benito-Gonzalez, I. Rodriguez-Ramos, and A. Guerrero-Ruiz. Methane combustion over supported palladium catalysts I. Reactivity and active phase. *Appl. Catal. B: Environ.*, 28:223–233, 2000.

[40] C. A. Müller, M. Maciejewski, R. A. Koeppel, and A. Baiker. Combustion of methane over palladium/zirconia: effect of Pd-particle size and role of lattice oxygen. *Catal. Today*, 47:245–252, 1999.

[41] A. Hellman, A. Resta, N. M. Martin, J. Gustafson, A. Trinchero, P.-A. Carlsson, O. Balmes, R. Felici, R. van Rijn, J. W. M. Frenken, J. N. Andersen, E. Lundgren, and H. Grönbeck. The active phase of palladium during methane oxidation. *J. Phys. Chem. Lett.*, 3:678–682, 2012.

[42] A. K. Datye, J. Bravo, T. R. Nelson, P. Atanasova, M. Lyubovsky, and L. Pfefferle. Catalyst microstructure and methane oxidation reactivity during the Pd-PdO transformation on alumina supports. *Appl. Catal. A: Gen.*, 198:179–196, 2000.

[43] P. Gelin, L. Urfels, M. Primet, and E. Tena. Complete oxidation of methane at low temperature over Pt and Pd catalysts for the abatement of lean-burn natural gas fuelled vehicles emissions: influence of water and sulphur containing compounds. *Catal. Today*, 83:45–57, 2003.

[44] R. Gholami, M. Alyani, and K. J. Smith. Deactivation of Pd catalysts by water during low temperature methane oxidation relevant to natural gas vehicle converters. *Catal.*, 5:561–594, 2015.

[45] R. Burch, F. Urbano, and P. Loader. Methane combustion over palladium catalysts: The effect of carbon dioxide and water on activity. *Appl. Catal. A: Gen.*, 123:173–184, 1995.

[46] J. C. van Giezen, F. R. van den Berg, J. L. Kleinen, A. J. van Dillen, and J. W. Geus. The effect of water on the activity of supported palladium catalysts in the catalytic combusion of methane. *Catal. Today*, 47:287–293, 1999.

[47] W.-H. Cheng, editor. *Methanol Production and Use*. CRC Press, 1994.

[48] F. Gallucci, A. Comite, G. Capannelli, and A. Basile. Steam reforming of methane in a membrane reaction: An industrial case study. *Ind. Eng. Chem. Res.*, 45:2994–3000, 2006.

[49] Q. Zhu, X. Zhao, and Y. Deng. Advances in the partial oxidation of methane to synthesis gas. *J. Nat. Gas Chem.*, 12:191–203, 2004.

[50] C. N. Satterfield. *Heterogeneous Catalysis in Industrial Practice*. McGraw-Hill, New York, 1991.

[51] A. Holmen. Direct conversion of methane to fuels and chemicals. *Catal. Today*, 142:2–8, 2009.

[52] S. S. Bharadwaj and L. D. Schmidt. Catalytic partial oxidation of natural gas to syngas. *Fuel Process. Technol.*, 42:109–127, 1995.

[53] S. C. Tsang, J. B. Claridge, and M. L. H. Green. Recent advances in the conversion of methane to synthesis gas. *Catal. Today*, 23:3–15, 1995.

[54] T. Zhu and M. Flytzani-Stephanopoulos. Catalytic partial oxidation of methane to synthesis gas over Ni-CeO_2. *Appl. Catal. A: Gen.*, 208:403–317, 2001.

[55] V. A. Kirillov, Z. A. Fedorova, M. M. Danilova, V. I. Zaikovskii, N. A. Kuzin, V. A. Kuzmin, T. A. Krieger, and V. D. Mescheryakov. Porous nickel based catalysts for partial oxidation of methane to synthesis gas. *Appl. Catal. A: Gen.*, 401:170–175, 2011.

[56] B. Li, H. Li, W. Weng, Q. Zhang, C. Huang, and H. Wan. Synthesis gas production from partial oxidation of methane over highly dispersed Pd/SiO_2 catalyst. *Fuel*, 103:1032–1038, 2013.

[57] H. Y. Wang and E. Ruckenstein. Partial oxidation of methane to synthesis gas over MgO- and SiO_2-supported rhodium catalysts. *J. Catal.*, 186:181–187, 1999.

[58] G. A. Somorjai and J. Carrazza. Structure sensitivity of catalytic reactions. *Ind. Eng. Chem. Fundamentals*, 25:63–69, 1986.

[59] M. Che and C. O. Bennett. The influence of particle size on the catalytic properties of supported metals. *Adv. Catal.*, 36:55–172, 1989.

[60] R. M. Lambert and G. Pacchioni, editors. *Chemisorption and Reactivity on Supported Clusters and Thin Films*, pages 117–152. Springer Science and Business Media, 1997.

[61] R. A. van Santen. Complementary structure sensitive and insensitive catalytic relationships. *Accounts Chem. Res.*, 42:57–66, 2008.

[62] K. Klier, J. S Hess, and R. G. Herman. Structure sensitivity of methane dissociation on palladium single crystal surfaces. *J. Chem. Phys.*, 107:4033, 1997.

[63] J. Wei and E. Iglesia. Structural requirements and reaction pathways in methane activation and chemical conversion catalyzed by rhodium. *J. Catal.*, 225:116–127, 2004.

[64] A. Yu. Stakheev, A. M. Batkin, N. S. Teleguina, G. O. Bragina, V. I. Zaikovsky, L. P. Prosvirin, A. K. Khudorozhkov, and V. I. Bukhtiyarov. Particle size effect on CH_4 oxidation over noble metals: Comparison of Pt and Pd catalysts. *Top. Catal.*, 56:306–310, 2013.

[65] R. Price, T. Eralp-Erden, E. Crumlin, S. Rani, S. Garcia, R. Smith, L. Deacon, C. Euaruksakul, and G. Held. The partial oxidation of methane over Pd/Al_2O_3 catalyst nanoparticles studied in-situ by near ambient-pressure x-ray photoelectron spectroscopy. *Top. Catal.*, 59:516–525, 2016.

[66] F. H. Ribeiro, M. Chow, and R. A. Dalla Betta. Kinetics of the complete oxidation of methane over supported palladium catalysts. *J. Catal.*, 146:537–544, 1994.

[67] D. Starr, H. Bluhm, Z. Liu, A. Knop-Gericke, and M. Hävecker. *In-situ Characterization of Heterogeneous Catalysis*, chapter 12: Application of Ambient-Pressure X-ray Photoelectron Spectroscopy for the In-Situ Investigation of Heterogeneous Catalytic Reactions. John Wiley & Sons, 2013.

[68] H. Siegbahn and K. Siegbahn. ESCA applied to liquids. *J. Electron Spectrosc. Relat. Phenom.*, 2:319–325, 1973.

[69] H. Siegbahn, L. Asplund, P. Kelfve, K. Hamrin, L. Karlsson, and K. Siegbahn. ESCA applied to liquids II. Valence and core electron spectra of formamide. *J. Electron Spectrosc. Relat. Phenom.*, 5:1059–1079, 1974.

[70] H. Siegbahn, L. Asplund, P. Kelfve, and K. Siegbahn. ESCA applied to liquids III. ESCA phase shifts in pure and mixed organic solvents. *J. Electron Spectrosc. Relat. Phenom.*, 7:411–419, 1975.

[71] R. W. Joyner, M. W. Roberts, and K. Yates. A "high-pressure" electron spectrometer for surface studies. *Surf. Sci.*, 87:501–509, 1979.

[72] F. D. Ogletree, H. Bluhm, G. Lebedev, S. C. Fadley, Z. Hussain, and M. Salmeron. A differentially pumped electrostatic lens system for photoemission studies in the millibar range. *Rev. Sci. Instruments*, 73:3872–3877, 2002.

[73] F. D. Ogletree, H. Bluhm, B. E. Hebenstreit, and M. Salmeron. Photoelectron spectroscopy under ambient and temperature conditions. *Nucl. Instruments Methods Phys. Res. Sect. A: Accel. Spectrometers, Detect. Assoc. Equip.*, 601:151–160, 2009.

[74] H. Bluhm. Photoelectron spectroscopy of surfaces under humid conditions. *J. Electron Spectrosc. Relat. Phenom.*, 177:71–84, 2010.

[75] M. Salmeron and R. Schlögl. Ambient pressure photoelectron spectroscopy: a new tool for surface science and nanotechnology. *Surf. Sci. Reports*, 63:169–199, 2008.

[76] A. Jürgensen, N. Heutz, H. Raschke, K. Merz, and R. Hergenröder. Behavior of supported palladium oxide nanoparticles under reaction conditions, studied with near ambient pressure xps. *Anal. Chem.*, 87:7848–7856, 2015.

[77] A. Yu Klyushin, T. C. R. Rocha, M. Hävecker, A. Knop-Gericke, and R. Schlögl. A near ambient pressure XPS study of Au oxidation. *Phys. Chem. Chem. Phys.*, 16:7881, 2014.

[78] F. Tao, M. Grass, Y. Zhang, D. R. Butcher, J. R. Renzas, Z. Liu, Jen Y. Chung, B. S. Mun, M. Salmeron, and G. A. Somorjai. Reaction-driven restructuring of Rh-Pd and Pt-Pd core shell nanoparticles. *Sci.*, 322:932–934, 2008.

[79] F. Tao, M. E. Grass, Y. Zhang, D. R. Butcher, F. Aksoy, S. Aloni, V. Altoe, S. Alayoglu, J. R. Renzas, C-K. Tsung, Z. Zhu, Z. Liu, M. Salmeron, and G. A. Somorjai. Evolution of structure and chemistry of bimetallic nanoparticle catalysts under reaction conditions. *J. Am. Chem. Soc.*, 132:8697–8703, 2010.

[80] A. Shavorskiy, F. Aksoy, M. E. Grass, Z. Liu, H. Bluhm, and G. Held. A step toward the wet surface chemistry of glycine and alanine on Cu{111}: Destabilization and decomposition in the presence of near-ambient water vapor. *J. Am. Chem. Soc.*, 133:6659–6667, 2011.

[81] A. Shavorskiy, T. Eralp, K. Schulte, H. Bluhm, and G. Held. Surface chemistry of glycine on Pt{111} in different aqueous environments. *Surf. Sci.*, 607:10–19, 2013.

[82] M. Favaro, B. Jeong, P. N. Ross, J. Yano, Z. Hussain, Z. Liu, and E. J. Crumlin. Unravelling the electrochemical double layer by direct probing of the solid/liquid interface. *Nat. Commun.*, 7:12695, 2016.

[83] Z. A. Feng, C. B. Gopal, X. Ye nd Z. Guan, B. Jeong, E. J. Crumlin, and W. C. Chueh. Origin of overpotential-dependent surface dipole at CeO_{2-x}/gas interface during electrochemical oxygen insertion reactions. *Chem. Mater.*, 2016.

[84] Y. Zhu, S. Zhang, J. Shan, L. Nguyen, S. Zhan, X. Gu, and F. Tao. In situ surface chemistries and catalytic performances of ceria doped with palladium, platinum and rhodium in methane partial oxidation for the production of syngas. *ACS Catal.*, 3:2627–2639, 2013.

[85] F. F. Tao, J. Shan, L. Nguyen, Z. Wang, S. Zhang, L. Zhang, Z. Wu, W. Huang, S. Zeng, and P. Hu. Understanding complete oxidation of methane on spinel oxides at a molecular level. *Nat. Commun.*, 6:7798, 2015.

[86] J. A. Schwarz, C. Contescu, and A. Contescu. Methods for preparation of catalytic materials. *Chem. Rev.*, 95:477–510, 1995.

[87] F. Pinna. Supported metal catalysts preparation. *Catal. Today*, 41:129–137, 1998.

[88] M. L. Toebes, J. A. van Dillen, and K. P. de Jong. Synthesis of supported palladium catalysts. *J. Mol. Catal. A: Chem.*, 173:75–98, 2001.

[89] T. V. Choudhary, S. Banerjee, and V. R. Choudhary. Catalysts for combustion of methane and lower alkanes. *Appl. Catal. A: Gen.*, 234:1–23, 2002.

[90] M. R. Feaviour and E. R. Schofield. Scientific bases for the preparation of heterogeneous catalysts. *Platinum Met. Rev.*, 51:42–44, 2007.

[91] J. Haber, J. H. Block, and B. Delmon. Manual of methods and procedures for catalyst characterization. *Pure Appl. Chem.*, 67:1257–1306, 1995.

[92] J. Regalbuto, editor. *Catalyst Preparation: Science and Engineering*. CRC Press, 2016.

[93] R. D. Gonzalez, T. Lopez, and R. Gomez. Sol-gel preparation of supported metal catalysts. *Catal. Today*, 35:293–317, 1997.

[94] G. Ertl, H. Knözinger, and J. Weitkamp. *Preparation of Solid Catalysts*. Wiley, 1999.

[95] K. de Jong. *Synthesis of solid catalysts*. Wiley, 2009.

[96] S. Hofmann. *Auger and X-Ray Photoelectron Spectroscopy in Materials Science*. Springer Science and Business Media, 2012.

[97] Paul van der Heide. *X-Ray Photoelectron Spectroscopy: An Introduction to Principles and Practices*. John Wiley & Sons, 2011.

[98] G. Held. Photoelectron spectroscopy of metal surfaces for potential heterogeneous catalysis. *Spectrosc. Prop. Inorg. Organomet. Compd.*, 42:1–33, 2012.

[99] T. L. Barr. *Modern ESCA: The Principles and Practice of X-Ray Photoelectron Spectroscopy*. CRC Press, 1994.

[100] K. W. Kolasinski. *Surface Science: Foundations of Catalysis and Nanoscience*. Wiley, 2008.

[101] S. Baldanza. *Model studies for chiral modification of heterogeneous catalysts: Amino acids and tartaric acid on Cu and Ni surfaces*. PhD thesis, University of Reading, 2014.

[102] J. Cazes. *Analytical Instrumentation Handbook*. CRC Press, 3rd edition, 2004.

[103] D. Starr, Z. Liu, M. Hävecker, A. Knop-Gericke, and H. Bluhm. Investigation of solid/vapor interfaces using ambient pressure x-ray photoelectron spectroscopy. *Chem. Soc. Rev.*, 42:5833–5857, 2013.

[104] D. Briggs and M. P. Seah, editors. *Practical Surface Analysis: Auger and X-ray Photoelectron Spectroscopy*, volume 1. Wiley, 2nd edition, 1996.

[105] I. Langmuir. The constitution and fundamental properties of solids and liquids. *J. Am. Chem. Soc.*, 38:2221–2295, 1916.

[106] M. Sardela, editor. *Practical Materials Characterizaton*. Springer, 2014.

[107] P. S. Bagus, E. S. Ilton, and C. J. Nelin. The interpretation of XPS spectra: Insights into materials properties. *Surf. Sci. Reports*, 68:273–304, 2013.

[108] U. Gelius. Binding energies and chemical shifts in ESCA. *Phys. Scripta*, 9:133–147, 1974.

[109] K. S. Kim, A. F. Gossmann, and N. Winograd. X-ray photoelectron spectroscopic studies of palladium oxides and the palladium-oxygen electrode. *Anal. Chem.*, 46:197–200, 1974.

[110] S. Lizzit. *Surface-shifted core level photoemission from clean and oxygen covered metal surfaces*. PhD thesis, Technische Universität München, 2003.

[111] R. C. Baetzold, G. Apai, E. Shustorovich, and R. Jaeger. Surface core-level shifts for Pt single-crystal surfaces. *Phys. Rev. B*, 26:4022–4027, 1982.

[112] S. P. Kowalczyk, L. Ley, R. L. Martin, F. R. McFeely, and D. A. Shirley. Relaxation and final-state structure in XPS of atom, molecules and metals. *Faraday Discuss. Chem. Soc.*, 60:7–17, 1975.

[113] J. M. Walls and R. Smith, editors. *Surface Science Techniques*. Elsevier, 2013.

[114] P. Ascarelli, M. Cini, G. Missoni, and N. Nisticò. XPS line broadening in small metal particles. *J. de Physique Colloques*, 38:125–128, 1977.

[115] S. Hüfner. *Photoelectron Spectroscopy: Principles and Applications*. Springer Science and Business Media, 2013.

[116] G. C. Smith. *Surface Analysis by Electron Spectroscopy*. Measurement and Interpretation. Springer Science and Business Media, 2013.

[117] J. C. Riviere and S. Myhra. *Handbook of Surface and Interface Analysis*. CRC Press, 2009.

[118] D. P. Woodruff and T. A. Delchar. *Modern Techniques of Surface Science*. Cambridge University Press, UK, 1994.

[119] P. Ducheyne, K. Healy, D. E. Hutmacher, D. W. Grainger, and C. J. Kirkpatrick. *Comprehensive Biomaterials*. Newnes, 2015.

[120] R. Talman. *Accelerator X-Ray Sources*. John Wiley & Sons, 2007.

[121] A. C. Thompson, editor. *X-ray Data Booklet*. Lawrence Berkeley National Laboratory, Berkeley, 3rd edition, 2009.

[122] J. Chavanne. The art of the undulator. *ESRF News*, 61:8–9, 2012.

[123] D. H. Bilderback, P. Elleaume, and E. Weckert. Review of third and next generation synchrotron light sources. *J. Phys. B: At. Mol. Opt. Phys.*, 38:773–797, 2005.

[124] D. Castelvecchi. Next-generation x-ray source fires up. *Nat.*, 3:7567, 2015.

[125] H. Winick. Fourth generation light sources. In *PAC97*, Vancouver, Canada, 1997.

[126] P. J. Viccaro and G. K. Shenoy. Photon energy tunability of the advanced photon source undulators. *Nucl. Instruments Methods Phys. Res.*, 266:112–115, 1988.

[127] T. Eralp, A. Shavorskiy, Z. V. Zheleva, G. Held, N. Kalashnyk, Y. Ning, and T. R. Linderoth. Global and local expression of chirality in serine on the Cu{110} surface. *Langmuir*, 26:18841–18851, 2010.

[128] T. Eralp, A. Ievins, A. Shavorskiy, S. J. Jenkins, and G. Held. The importance of attractive three-point interaction in enantioselective surface chemistry: Stereospecific adsorption of serine on the intrinsically chiral Cu{531} surface. *J. Am. Chem. Soc.*, 134:9615–9621, 2012.

[129] S. Baldanza, A. Cornish, R. E. J. Nicklin, Z. V. Zheleva, and G. Held. Surface chemistry of alanine on Cu{111}: Adsorption geometry and temperature dependence. *Surf. Sci.*, 629:114–122, 2014.

[130] S. Baldanza, J. Ardini, A. Giglia, and G. Held. Stereochemistry and thermal stability of tartaric acid on the intrinsically chiral Cu{531} surface. *Surf. Sci.*, 643:108–116, 2016.

[131] H. Bluhm, M. Hävecker, A. Knop-Gericke, E. Kleimenov, R. Schlögl, D. Teschner, V. I. Bukhtiyarov, D. F. Ogletree, and M. Salmeron. Methanol oxidation on a copper catalyst investigated using in situ x-ray photoelectron spectroscopy. *J. Phys. Chem. B*, 108:14340–14347, 2004.

[132] M. Grass, P. Karlsson, F. Aksoy, M. Lundqvist, B. Wannberg, B. Mun, Z. Hussain, and Z. Liu. New ambient pressure photoemission endstation at Advanced Light Source beamline 9.3.2. *Rev. Sci. Instruments*, 81, 2010.

[133] V. Pérez-Dieste, L. Aballe, S. Ferrer, J. Nicolàs, C. Escudero, A. Milán, and E. Pellegrin. Near ambient pressure XPS at ALBA. *J. Physics: Conf. Ser.*, 425:20–23, 2013.

[134] J. Schnadt, J. Knudsen, J. Andersen, H. Siegbahn, A. Pietzsch, F. Hennies, N. Johansson, N. Mårtensson, G. Öhrwall, S. Bahr, S. Mähl, and O. Schaff. The new ambient-pressure x-ray photoelectron spectroscopy instrument at MAX-lab. *J. Synchrotron Radiat.*, 19:701–704, 2012.

[135] R. E. J. Nicklin. *Emulation of Chiral Hydrogenation Catalysts by Adsorption of Small Molecules onto Ni Surfaces*. PhD thesis, University of Reading, 2014.

[136] E. de Hoffmann and V. Stroobant. *Mass Spectrometry: Prinicples and Applications*. John Wiley & Sons, 3rd edition, 2007.

[137] J. H. Gross. *Mass Spectrometry: A Textbook*. Springer Science and Business Media, 2nd edition, 2011.

[138] J. Cazaux. About the charge compensation of insulating samples in XPS. *J. Electron Spectrosc. Relat. Phenom.*, 113:15–33, 200.

[139] J. Cazaux. Secondary electron emission and fundamentals of charging mechanisms in XPS. *J. Electron Spectrosc. Relat. Phenom.*, 178-179:357–372, 2010.

[140] J. Cazaux. Mechanisms of charging in electron spectroscopy. *J. Electron Spectrosc. Relat. Phenom.*, 105:155–185, 1999.

[141] A. Vilan, T. Bendikov, and H. Cohen. Secondary electron emission control in x-ray photoelectron spectroscopy. *J. Electron Spectrosc. Relat. Phenom.*, 162:99–105, 2008.

[142] J. W. Niemantsverdriet. *Spectroscopy in Catalysis: An Introduction*. VCH, 1993.

[143] D. R. Baer, M. H. Engelhard, D. J. Gaspar, A. S. Lea, and C. F. Windisch. Use and limitations of electron flood gun control of surface potential during XPS: two non-homogeneous sample types. *Surf. Interface Analysis*, 33:781–790, 2002.

[144] R. T. Lewis and M. A. Kelly. Binding energy reference in x-ray photoelectron spectroscopy of insulators. *J. Electron Spectrosc. Relat. Phenom.*, 20:105–115, 1980.

[145] O. Brunke, K. Brockdorf, S. Drews, B. Müller, T. Donath, J. Herzen, and F. Beckmann. Comparison between x-ray tube-based and synchrotron radiation-based μCT. In *Optical Engineering and Applications*. International Society for Optics and Photonics, 2008.

[146] M. Inagaki and F. Kang, editors. *Materials Science and Engineering of Carbon: Characterization*. Butterworth-Heinemann, 2016.

[147] H. G. Wallace, J. G. Stark, and M. L. McGlashan. *Chemistry Data Book*. Hodder Education, 2nd edition, 1989.

[148] A. B. Sproul, M. A. Green, and J. Zhao. Improved value for the silicon intrinsic carrier concentration at 300 K. *Appl. Phys. Lett.*, 57:255, 1990.

[149] B. Strohmeier. Characterization of an activated alumina claus catalyst by XPS. *Surf. Sci. Spectra*, 3:141, 1994.

[150] L. E. Ramos, J. Furthmüller, and F. Bechstedt. Quasiparticle band structures and optical spectra of β-cristobalite SiO_2. *Phys. Rev. B*, 69:85–102, 2004.

[151] Z. A. Weinberg, G. W. Rubloff, and E. Bassous. Transmission, photoconductivity and the experimental band gap of thermally grown SiO_2 films. *Phys. Rev. B*, 19:3107, 1979.

[152] M. Yazdanmehr, S. J. Asadabadi, A. Nourmohammadi, M. Ghasemzadeh, and M. Rezvanian. Electronic structure and bandgap of γ-Al_2O_3 compound using mBJ exchange potential. *Nanoscale Res. Lett.*, 7:488–498, 2012.

[153] B. Ealet, M. H. Elyakhloufi, E. Gillet, and M. Ricci. Electronic and crystallographic structure of γ-alumina thin films. *Thin Solid Films*, 250:92–100, 1994.

[154] R. Xu, S. K. Selvaraj, N. Azimi, and C. G. Takoudis. Growth characteristics and properties of yttrium oxide thin films by atomic layer deposition from novel $Y(iPrCp)_3$ precursor and O_3. *ECS Transactions*, 50:107–116, 2013.

[155] C. Korte, A. Peters, J. Janek, D. Hesse, and N. Zakharov. Ionic conductivity and activation energy for oxygen ion transport in superlattices – the semicoherent multilayer system YSZ (ZrO_2 + 9.5 mol% Y_2O_3)/Y_2O_3. *Phys. Chem. Chem. Phys.*, 10:4623–4635, 2008.

[156] X. Yu and H. Hantsche. Vertical differential charging in monochromatized small spot x-ray photoelectron spectroscopy. *Surf. Interface Analysis*, 20:555–558, 1993.

[157] M. Liehr, P. A. Thiry, J. J. Pireaux, and R. Caudano. Characterisation of insulators by HREELS: Application of a surface-potential stabilisation technique. *Phys. Rev. B*, 33:5682, 1986.

[158] D. Zemlyanov, B. Aszalos-Kiss, E. Kleimenov, D. Teschner, S. Zafeiratos, M. Hävecker, A. Knop-Gericke, R. Schlögl, H. Gabasch, W. Unterberger, K. Hayek, and B. Klötzer. In situ XPS study of Pd(111) oxidation. Part 1: 2D oxide formation in 10^3 mbar O_2. *Surf. Sci.*, 600:983–994, 2006.

[159] W. Griffith and S. Robinson. *Pd Palladium: Palladium Compounds*. Springer Science, 2013.

[160] B. Singh, R. Hesse, and M. R. Linford. Good practices for XPS peak fitting. *Vac. Technol. Coat.*, pages 2–7, 2015.

[161] C. G. Pantano and T. E. Madey. Electron beam damage in Auger electron spectroscopy. *Appl. Surf. Sci.*, 7:115–141, 1981.

[162] P. Gelin and M. Primet. Complete oxidation of methane at low temperature over noble metal based catalysts: a review. *Appl. Catal. B: Environ.*, 39:1–37, 2002.

[163] R. Burch and F.J. Urbano. Investigation of the active state of supported palladium catalysts in the combustion of methane. *Appl. Catal. A: Gen.*, 124:121–138, 1995.

[164] A. Gannouni, B. Albela, M. Said Zina, and L. Bonneviot. Metal dispersion, accessibility and catalytic activity in methane oxidation of mesoporus templated aluminosilica supported palladium. *Appl. Catal. A: Gen.*, 464-465:116–127, 2013.

[165] Y. Cai, Y. Niu, and Z. Chen. Synthesis of methanol and isobutanol from syngas over ZrO_2- based catalysts. *Fuel Process. Technol.*, 50(1-2):163–170, 1997.

[166] K. Li and D. Jiang. Methanol synthesis from syngas in the homogeneous system. *J. Mol. Catal. A: Chem.*, 147(1-2):125–130, 1999.

[167] Y. Chen, Y. Wang, H. Xu, and G. Xiong. Efficient production of hydrogen from natural gas steam reforming in palladium membrane reactor. *Appl. Catal. B: Environ.*, 80:283–294, 2008.

[168] J. B. Claridge, M. Green, S. C. Tsang, A. York, A. T. Ashcroft, and P. D. Battle. A study of carbon deposition on catalysts during the partial oxidation of methane to synthesis gas. *Catal. Lett.*, 22(4):299–305, 1993.

[169] P. Vernon, M. Green, A.K. Cheetham, and A.T. Ashcroft. Partial oxidation of methane to synthesis gas. *Catal. Lett.*, 6(2):181–186, 1990.

[170] D. Teschner, A. Pestryakov, E. Kleimenov, M. Hävecker, H. Bluhm, H. Sauer, A. Knop-Gericke, and R. Schlögl. High-pressure x-ray photoelectron spectroscopy on palladium model hydrogenation catalysts. Part 1: Effect of gas ambient and temperature. *J. Catal.*, 230:186–194, 2005.

[171] R. Burch, D.J. Crittle, and M.J. Hayes. C-H bond activation in hydrocarbon oxidation on heterogeneous catalysts. *Catal. Today*, 47:229–234, 1999.

[172] E. Lundgren, G. Kresse, C. Klein, M. Borg, J.N. Andersen, M. De Santis, Y. Gauthier, C. Konvicka, M. Schmid, and P. Varga. Two-dimensional oxide on Pd(111). *Phys. Rev. Lett.*, 88:246103, 2002.

[173] S. Kaya, H. Ogasawara, L. Naslund, J-O. Forsrell, H. Casalongue, D. Miller, and A. Nilsson. Ambient-pressure photoelectron spectroscopy for heterogeneous catalysis and electrochemistry. *Catal. Today*, 205:101–105, 2013.

[174] A.S. Ivanova, E.M. Slavinskaya, R.V. Gulyaev, V.I. Zaikovskii, O.A. Stonkus, I.G. Danilova, L.M. Plyasova, I.A. Polukhina, and A.I. Boronin. Metal-support interactions in Pt/Al_2O_3 and Pd/Al_2O_3 catalysts for CO oxidation. *Appl. Catal. B: Environ.*, 97:57–71, 2010.

[175] D.A. Shirley. High-resolution x-ray photoemission spectrum of the valence bands of gold. *Phys. Rev. B*, 5:4709, 1972.

[176] R. Arrigo, M. Schuster, Z. Xie, Y. Yi, G. Wowsnick, L. Sun, K. Hermann, M. Friedrich, P. Kast, M. Hävecker, A. Knop-Gericke, and R. Schlögl. Nature of the N-Pd interaction in nitrogen-doped carbon nanotube catalysts. *ACS Catal.*, 5:2740–2753, 2015.

[177] H. Gabasch, K. Hayek, B. Klötzer, W. Unterberger, E. Kleimenov, D. Teschner, S. Zafeiratos, M. Hävecker, A. Knop-Gericke, R. Schlögl, B. Aszalos-Kiss, and D. Zemlyanov. Methane oxi-

dation on Pd(111): In situ XPS indentification of active phase. *J. Phys. Chem. C*, 111(7957-7962), 2007.

[178] D. Teschner, J. Borsodi, A. Wootsch, Z. Revay, M. Hävecker, A. Knop-Gericke, S. D. Jackson, and R. Schlögl. The roles of subsurface carbon and hydrogen in palladium-catalysed alkyne hydrogenation. *Sci.*, 320:86–89, 2008.

[179] T. Fujitani, M. Saito, Y. Kanai, T. Watanabe, J. Nakamura, and T. Uchijima. Development of an active Ga_2O_3 supported palladium catalyst for the synthesis of methanol from carbon dioxide and hydrogen. *Appl. Catal. A: Gen.*, 125:L199–L202, 1995.

[180] R. S. Monteiro, D. Zemlyanov, J. M. Storey, and F. H. Ribeiro. Turnover rate and reaction orders for the complete oxidation of methane on a palladium foil in excess dioxygen. *J. Catal.*, 199:291–301, 2001.

[181] H. Gabasch, W. Unterberger, K. Hayek, B. Klötzer, E. Kleimenov, D. Teschner, S. Zafeiratos, M. Hävecker, A. Knop-Gericke, R. Schlögl, J. Han, F. Ribeiro, B. Aszalos-Kiss, T. Curtin, and D. Zemlyanov. In situ XPS study of Pd(111) oxidation at elevated pressure, Part 2: Palladium oxidation in the 10^{-1} mbar range. *Surf. Sci.*, 600:2980–2989, 2006.

[182] J. P. Boitiaux, J. Cosyns, and S. Vasudevan. Hydrogenation of highly unsaturated hydrocarbons over highly dispersed palladium catalyst: Part I: Behaviour of small metal particles. *Appl. Catal.*, 6(1):41 – 51, 1983.

[183] B. Tardy, C. Noupa, C. Leclercq, J. C. Bertolini, A. Hoareau, M. Treilleux, J. P. Faure, and G. Nihoul. Catalytic hydrogenation of 1,3-butadiene on Pd particles evaporated on carbonaceous supports: Particle size effect. *J. Catal.*, 129(1):1 – 11, 1991.

[184] J. Silvestre-Albero, G. Rupprechter, and H-J. Freund. Atmospheric pressure studies of selective 1,3-butadiene hydrogenation on well-defined $Pd/Al_2O_3/NiAl(110)$ model catalysts: Effect of Pd particle size. *J. Catal.*, 240(1):58 – 65, 2006.

[185] A. Ota, E. Kunkes, J. Krohnert, M. Schmal, and M. Behrens. Particle size effect in methane activation over supported palladium nanoparticles. *Appl. Catal. A: Gen.*, 452:203–213, 2013.

[186] N. Semagina, A. Renken, and L. Kiwi-Minsker. Palladium nanoparticle size effect in 1-hexyne selective hydrogenation. *J. Phys. Chem. C*, 111:13933–13937, 2007.

[187] L. Ji, J. Lin, and H. C. Zeng. Metal-support interactions in Co/Al_2O_3 catalysts: A comparative study on reactivity of support. *J. Phys. Chem. B*, 104:1783–1790, 2000.

[188] M. Lyubovsky, S. Roychoudhury, and R. LaPierre. Catalytic partial oxidation of methane to syngas at elevated pressures. *Catal. Lett.*, 99:113–117, 2005.

[189] V. Bychkov, Y. Tyulenin, M. Slinko, D. Shashkin, and V. Korchak. The study of the oscillatory behavior during methane oxidation over Pd catalysts. *J. Catal.*, 267:181–187, 2009.

[190] S. Suhonen, M. Valden, M. Pessa, A. Savimäki, M. Härkönen, M. Hietikko, J. Pursiainen, and R. Laitinen. Characterization of alumina supported Pd catalysts modified by rare earth oxides using x-ray photoelectron spectroscopy and x-ray diffraction: enhanced thermal stability of PdO in Nd/Pd catalysts. *Appl. Catal. A: Gen.*, 207(1–2):113 – 120, 2001.

[191] O. Edenhofer, R. Pichs-Madruga, Y. Sokona, E. Farahani, S. Kadner, K. Seyboth, A. Adler, I. Baum, S. Brunner, P. Eickemeier, B. Kriemann, J. Savolainen, S. Schlomer, C. von Stechow, T. Zwichel, and J.C. Minx, editors. *Climate Change 2014: Mitigation of Climate Change. Contribution of Working Group III to the Fifth Assessment Report of the Intergovernmental Panel on Climate Change*. IPCC, Cambridge University Press, UK, 2014.

[192] H. Zhu, R. Kee, M. Pillai, and S. Barnett. Modelling electrochemical partial oxidation of methane for cogeneration of electricity and syngas in solid-oxide fuel cells. *J. Power Sources*, 183:143–150, 2008.

[193] F. Cayan, M. Zhi, S. Pakalapati, I. Celik, N. Wu, and R. Gemmen. Effects of coal syngas impurities on anodes of solid oxide fuel cells. *J. Power Sources*, 185:595–602, 2008.

[194] T. Kobayashi, K. Nakagawa, K. Tabata, and M. Haruta. Partial oxidation of methane over silica catalysts promoted by 3d transition metal ions. *J. Chem. Soc. Chem. Commun.*, 13:1609–1610, 1994.

[195] K. Muto, N. Katada, and M. Niwa. Complete oxidation of methane on supported palladium catalyst: Support effect. *Appl. Catal. A: Gen.*, 134:203–215, 1996.

[196] K. Muto, N. Katada, and M. Niwa. Thermally stable environmental catalyst: oxidation of methane over calcined palladium loaded on silica monolayer. *Catal. Today*, 35:145–151, 1997.

[197] R. Gholami and K. J. Smith. Activity of PdO/SiO_2 catalysts for CH_4 oxidation following thermal treatments. *Appl. Catal. B: Environ.*, 168-169:156–163, 2015.

[198] G. Zhu. *Kinetics of complete methane oxidation on palladium model catalysts*. PhD thesis, Worcester Polytechnic Institute, January 2004.

[199] G. Zhu, K. Fujimoto, D. Zemlyanov, A. Datye, and F. Riberio. Coverage of palladium by silicon oxide during reduction in H_2 and complete oxidation of methane. *J. Catal.*, 225:170–178, 2004.

[200] B. Min, A. Santra, and D. Goodman. Understanding silica-supported metal catalysts: Pd/silica as a case study. *Catal. Today*, 85:113–124, 2003.

[201] G. Veith, A. Lupini, S. Rashkeev, S. Penny, D. Mullins, V. Schwartz, C. Bridges, and N. Dudney. Thermal stability and catalytic activity of gold nanoparticles supported on silica. *J. Catal.*, 262:92–101, 2009.

[202] S. Joo, J. Park, C. Tsung, Y. Yamada, P. Yang, and G. Somorjai. Thermally stable Pt/mesoporous silica core-shell nanocatalysts for high-temperature reactions. *Nat. Mater.*, 8:126–131, 2009.

[203] C. Lai. Mesoporous silica nanomaterials applications in catalysis. *J. Thermodyn. Catal.*, 5:1–3, 2013.

[204] D. Wragg, R. Morris, and A. Burton. Pure silica zeolite-type frameworks: A structural analysis. *Chem. Mater.*, 20:1561–1570, 2008.

[205] J. Spivey and M. Gupta, editors. *Catalysis: Catalytic applications of mesoporous silica-based materials*, volume 24. RSC Publishing, 2012.

[206] L. Giraldo, B. Lopez, L. Perez, S. Urrego, L. Sierra, and M. Mesa. Mesoporous silica applications. *Macromol. Symp.*, 258:129–141, 2007.

[207] T. Keller, S. Isabettini, D. Verboekend, E. Rodrigues, and J. Perez-Ramirez. Hierachical high-silica zeolites as superior base catalysts. *Chem. Sci.*, 5:677–684, 2014.

[208] L. Zhuravlev. The surface chemistry of amorphous silica: Zhuravlev model. *Colloids Surfaces A: Physicochem. Eng. Aspects*, 173:1–38, 2000.

[209] T. Ishikawa, M. Matsuda, A. Yasukawa, K. Kandori, S. Inagaki, T. Fukushima, and S. Kondo. Surface silanol groups of mesoporous silica FSM-16. *J. Chem. Soc. Faraday Transactions*, 92:1985–1989, 1996.

[210] C. Cullis, T. Nevell, and D. Trimm. Role of the catalyst support in the oxidation of methane over palladium. *J. Chem. Soc. Faraday Transactions*, 1:1406–1412, 1972.

[211] D. Roth, P. Gelin, M. Primet, and E. Tena. Catalytic behaviour of Cl-free and Cl-containing Pd/Al_2O_3 catalysts in the total oxidation of methane at low temperature. *Appl. Catal. A: Gen.*, 203:37–45, 2000.

[212] T. Baldwin and R. Burch. Catalytic combustion of methane over supported palladium catalysts: II. support and possible morphological effects. *Appl. Catal.*, 66:359–381, 1990.

[213] R. Lamber and W. Romanowski. Dispersion changes of platinum supported on silica glass during thermal treatment in oxgygen and hydrogen atmospheres. *J. Catal.*, 105:213–226, 1987.

[214] R. Lamber, N. Jaeger, and G. Schultz-Ekloff. Metal-support interaction in the Pd/SiO_2 system: Influence of the support pretreatment. *J. Catal.*, 123:285–297, 1990.

[215] L. Sheu, Z. Karpinski, and W. M. H. Sachtler. Effects of palladium particle size and palladium silicide formation on FT-IR spectra and carbon monoxide adsorbed on palladium/silicon dioxide catalysts. *J. Phys. Chem.*, 93:4890–4894, 1989.

[216] W. Juszczyk and Z. Karpinski. Characterisation of supported palladium catalysts: II. Pd/SiO_2. *J. Catal.*, 117:519–532, 1989.

[217] A. Stoch, J. Stoch, and A. Rakowska. An XPS and SEMS study of silica sol-gel/metal substrate interaction. *Surf. Interface Analysis*, 22:242–247, 1994.

[218] J.Z. Shyu, K. Otto, W.L.H. Watkins, G.W. Graham, R.K. Belitz, and H.S. Gandhi. Characterisation of Pd/γ-alumina catalysts containing ceria. *J. Catal.*, 114:23–33, 1988.

[219] J. Finster. SiO_2 in 6:3 (stishovite) and 4:2 co-ordination – characterisation by core level spectroscopy (XPS/XAES). *Surf. Interface Analysis*, 12:309–314, 1988.

[220] R. Nyholm and N. Martensson. Core level binding energies for the elements Zr-Te (Z=40-52). *J. Phys. C: Solid State Phys.*, 13:L279, 1980.

[221] A. Bahari. Deconvoluted Si 2p photoelectron spectra of ultra thin SiO_2 film with FitXPS method. *J. Nanostructures*, 1:54–61, 2012.

[222] L-A. O'Hare, B. Parbhoo, and S. R. Ledley. Development of a methodology for XPS curve-fitting of the Si 2p core level of siloxane materials. *Surf. Interface Analysis*, 36(1427-1434), 2004.

[223] J-M. Park, K. H. Kim, C. J. An, M. L. Jin, J-H. Hahn, B-S. Kong, and H-T. Jung. Highly robust SiCOH/mesoporous SiO_2 ultralow dielectric films with heterostructures. *RSC Adv.*, 4:28409–28416, 2014.

[224] S. Blomberg, M. J. Hoffmann, J. Gustafson, N. M. Martin, V. R. Fernandes, A. Borg, Z. Liu, R. Chang, S. Matera, K. Reuter, and E. Lundgren. In situ x-ray photoelectron spectroscopy of model catalysts: At the edge of the gap. *Phys. Rev. Lett.*, 110:117601, 2013.

[225] F. J. J. G. Janssen and R. A. van Santen, editors. *Environmental Catalysis*, volume 1 of *Catalytic Science Series*. Imperial College Press, 1999.

[226] A. M. Venezia, R. Murania, G. Pantaleo, and G. Deganello. Pd and PdAu on mesporous silica for methane oxidation: Effect ofSO_2. *J. Catal.*, 251:94–102, 2007.

[227] M. Niwa, N. Katada, and K. Okumura. *Characterization and Design of Zeolite Catalysts*. Springer Science and Business Media, 2010.

[228] K. Otto. Methane oxidation over Pt on γ-alumina: Kinetics and structure sensitivity. *Langmuir*, 5:1364–1369, 1989.

[229] M. A. Raj, G. M. Madhu, and Y. J. Rao. Kinetics of palladium catalysed partial oxidation of methane. *Indian J. Chem. Technol.*, 13:107–113, 2006.

[230] J. Au-Yeung, K. Chen, A. T. Bell, and E. Iglesia. Isotopic studies of methane oxidation pathways on PdO catalysts. *J. Catal.*, 188:132–139, 1999.

[231] X. Zhang, C. Lee, D. M. Mingos, and D. Hayward. Oscillatory behaviour during the oxidation of methane over palladium metal catalysts. *Appl. Catal. A: Gen.*, 240:183–197, 2003.

[232] A. Karelovic and P. Ruiz. CO_2 hydrogenation at low temperature over Rh/γ-Al_2O_3 catalyts: Effect of the metal particle size on catalytic performance and reaction mechanism. *Appl. Catal. B: Environ.*, 113-114:237–249, 2012.

[233] G. C. Bond. Metal-support and metal-additive effects in catalysis. *Platinum Met. Rev.*, 27:16–18, 1983.

[234] S. J. Tauster, S. C. Fung, and R. L. Garten. Strong metal-support interactions. Group 8 noble metals supported on titanium dioxide. *J. Am. Chem. Soc.*, 100:170–175, 1978.

[235] S. J. Tauster. Strong metal-support interactions. *Accounts Chem. Res.*, 20:389–394, 1987.

[236] R. Lambert and G. Pacchioni, editors. *Chemisorption and Reactivity on Supported Clusters and Thin Films: Towards an Understanding of Microscopic Processes in Catalysis*. Springer Science, 1997.

[237] T. Ueckert, R. Lamber, N. I. Jaeger, and U. Schubert. Strong metal-support interactions in a Ni/SiO_2 catalyst prepared via sol-gel synthesis. *Appl. Catal. A: Gen.*, 155:75–85, 1997.

[238] R. Hicks, H. Qi, M. L. Young, and R. G. Lee. Structure sensitivity of methane oxidation over platinum and palladium. *J. Catal.*, 122:280–294, 1990.

[239] W. Juszczyk, D. Lomot, J. Pielaszek, and Z. Karpinski. Transformation of Pd/SiO_2 catalysts during high temperature reduction. *Catal. Lett.*, 78:95–98, 2002.

[240] P. Crozier, R. Sharma, and A. Datye. Oxidation and reduction of small palladium particles on silica. *Microsc. Microanal.*, 4:278–285, 1998.

[241] V. Atzrodt, T. Wirth, and H. Lange. Investigation of NiSi and Pd_3Si thin films by AES and XPS. *Phys. Status Solidi A*, 62:531–537, 1980.

[242] P. J. Grunthaner, F. J. Grunthaner, and A. Madhukar. Chemical bonding and charge redistribution: Valence band and core level correlations for the Ni/Si, Pd/Si and Pt/Si systems. *J. Vac. Sci. Technol.*, 20:680, 1982.

[243] D. Dai and I. Davoli. An experimental study of an interface reaction at the practical Pd/Si interface by XPS. *Vac.*, 46:139–142, 1995.

[244] C. Lund and J. A. Dumesic. Strong oxide-oxide interactions in silica-supported Fe_3O_4: III. Water-induced migration of silica on geometrically designed catalysts. *J. Catal.*, 72:21–30, 1981.

[245] Z. Li and G. B. Hoflund. A review on complete oxidation of methane at low temperatures. *J. Nat. Gas Chem.*, 12:153–160, 2003.

[246] G. I. Panov, A. K. Uriarte, M. A. Rodkin, and V. I. Sobolev. Generation of active oxygen species on solid surfaces. Opportunity for novel oxidation technologies over zeolites. *Catal. Today*, 41:365–385, 1998.

[247] V. I. Sobolev, K. A. Dubkov, O. V. Panna, and G. I. Panov. Selective oxidation of methane to methanol on a FeZSM-5 surface. *Catal. Today*, 24:251–252, 1995.

[248] M. H. Groothaert, P. J. Smeets, B. F. Sels, P. A. Jacobs, and R. A. Schoonheydt. Selective oxidation of methane by the bis(μ-oxo)dicopper core stabized on ZSM-5 and mordenite zeolites. *J. Am. Chem. Soc.*, 127:1394–1395, 2005.

[249] J. Scherzer and A. J. Gruia. *Hydrocracking Science and Technology*. CRC Press, 1996.

[250] G. Albert, M. Kamps, K. Noweck, A. Reichenauer, R. Scherf, and U. Ziegler. Process and apparatus for producing aluminium alkoxides. Patent US-4590289, 1986.

[251] N. C. Dispenziere, L. L. Murrell, and D. E. W. Vaughan. Cracking process using catalysts with carries comprising silica supported on alumina. Patent EP-0238760, 1987.

[252] A. Meyer, K. Noweck, A. Reichenauer, and J. Schimanski. Process for the preparation of a catalyst carrier based on aluminosilicates. Patent US-5045519, 1991.

[253] R. de Haan, G. Joorst, E. Mokoena, and C. P. Nicolaides. Non-sulfided nickel supported on silicated alumina as catalyst for the hydrocracking of n-hexadecane and of iron-based Fischer-Tropsch wax. *Appl. Catal. A: Gen.*, 327:247–254, 2007.

[254] S. Xu, J. Li, D. Yang, and J. Hao. Effects of support acidity on the reaction mechanisms of selective catalytic reduction of NO by CH_4 in excess oxygen. *Front. Environ. Sci. Eng.*, 3:186–193, 2009.

[255] A. A. Tsyganenko, E. N. Storozheva, O. V. Manoilova, T. Lesage, M. Daturi, and J.-C. Lavalley. Brønsted acidity of silica silanol groups induced by adsorption of acids. *Catal. Lett.*, 70:159–163, 2000.

[256] P. Euzen, J-H. Le Gal, B. Rebours, and G. Martin. Deactivation of palladium catalyst in catalytic combustion of methane. *Catal. Today*, 47:19–27, 1999.

[257] W. Daniell, U. Schubert, R. Glöckler, A. Meyer, K. Noweck, and H. Knözinger. Enhanced surface acidity in mixed alumina-silicas: a low-temperature FTIR study. *Appl. Catal. A: Gen.*, 196:247–260, 2000.

[258] R. A. van Santen. *Catalysis: An Integrated Approach*, volume 123 of *Studies in surface science and catalysis*. Elsevier, 2000.

[259] T. Baldwin and R. Burch. Catalytic combustion of methane over supported palladium catalysts: I. Alumina supported catalysts. *Appl. Catal.*, 66:337–358, 1990.

[260] V. La Parola, G. Deganello, and A. M. Venezia. CoMo catalysts supported on aluminosilicates: synergy between support and sodium effects. *Appl. Catal. A: Gen.*, 260:237–247, 2004.

[261] M. Niwa, K. Awano, and Y. Murakami. Activity of supported platinum catalysts for methane oxidation. *Appl. Catal.*, 7:317–325, 1983.

[262] K. Narsimhan, K. Iyoki, K. Dinh, and Y. Roman-Leshkov. Catalytic oxidation of methane into methanol over copper-exchanged zeolites with oxygen at low temperature. *ACS Cent. Sci.*, 2:424–429, 2016.

[263] K. P. Sajith, Y. Shiota, and K. Yoshizawa. Role of acidic proton in the decomposition of NO over dimeric Cu(I) active sites in Cu-ZSM-5 catalyst. *ACS Catal.*, 4:2075–2085, 2014.

[264] M. Trombetta, G. Busca, S. Rossini, V. Piccoli, U. Cornaro, A. Guercio, R. Catani, and R. J. Willey. FT-IR studies on light olefin skeletal isomerization catalysis: III. Surface acidity and activity of amorphous and crystalline catalysts belonging to the SiO_2-Al_2O_3 system. *J. Catal.*, 179:581–596, 1998.

[265] A. Corma. Inorganic solid acids and their use in acid-catalyzed hydrocarbon reactions. *Chem. Rev.*, 95:559–614, 1995.

[266] T. Terai, T. Kobayashi, and S. Tanaka. Anomalous electrical resistivity of Al_2O_3 single crystal degraded by electron irradiation. *Nucl. Instruments Methods Phys. Res. Sect. B: Beam Interactions with materials Atoms*, 116:294–298, 1996.

[267] D. Ciuparu and L. Pfefferle. Support and water effects on palladium based methane combustion catalysts. *Appl. Catal. A: Gen.*, 209:415–428, 2001.

[268] N. M. Rodriguez, S. G. Oh, R. A. Dalla-Betta, and R. T. K. Baker. In situ electron microscopy studies of palladium supported on Al_2O_3, SiO_2 and ZrO_2 in oxygen. *J. Catal.*, 157:676–686, 1995.

[269] S. J. Tauster, S. C. Fung, R. T. K. Baker, and J. A. Horsley. Strong interactions in supported-metal catalysts. *Sci.*, 211:1121–1125, 1981.

[270] G. C. Bond. *The Modifications of Catalytic Properties by Metal-Support Interactions*. Elsevier, 2000.

[271] Y. Cerenius, F. Hennies, and P. Fernandes Tavares. Status of the MAX IV Laboratory. *Synchrotron Radiat. News*, 29:34–38, 2016.